NUMERICAL SIMULATION OF VISCOUS REACTING HYPERSONIC FLOW PAST CONES

Thesis by

Shaun Shariff

In Partial Fulfillment of the Requirements

for the Degree of

Doctor of Philosophy

California Institute of Technology

Pasadena, California

1999

(Submitted October 1, 1998)

To my parents, Asghar and Kay

Acknowledgements

I would like to thank my advisor, Professor Dale Pullin, for the guidance, ideas, and encouragement he has contributed to this project. His time, insight, and friendship have always been most available and helpful.

I would like to acknowledge Rob Mallett for his help at the beginning of this project, and for all the work that went into PGP before I got my hands on it. I would also like to thank James Quirk and Jean-Marc Moschetta for their enlightening discussions and helpful advice.

Several people have been immensely helpful with the many hardware and software problems encountered in this project. I appreciate the help of Heidi Lorenz-Wirzba of the Caltech Concurrent Supercomputing Facilities and the Center for Advanced Computing Research for her assistance with the parallel machines. Doug Shiels provided the script used to scan in the experimental data. I would also like to thank the Iris lab gurus, Ashish Misra, Mark Brady and Tobias Völkl, for generally knowing the answers to every question I asked. Mark and Tobias were especially helpful in surmounting the nearly catastrophic hardware problems suffered at the end of this project.

Last but not least, I wish to thank the many people who have made this journey worthwhile. The support I've received from all my family, especially those here in LA, has made this much easier. Much love to Loki der Quäler-Bock and Guerren Marter, friends for eighteen years, and thanks to everyone from Virginia Tech. Here at Caltech, there have been far too many to mention, but I'll try anyway. Mike Wehr and Dan Fain were indispensable for survival and sanity, as were all my friends at GALCIT, A&J, all the Daves, Liz, Matt, Michael, Nels, Rob, Scott, and Steve. Gratitude to Orbital, Hardfloor, Sven Väth, Frankie Bones, the Chemical Brothers, the Medicine Show, and Plastikman for the beats, inspiration, and motivation that kept me going.

This work was supported by ONR Grant N00014-90-J-1778 and AFOSR Grant F49620-93-1-0338.

Abstract

The stepback and partial grid techniques were used in the numerical simulation of laminar viscous reacting flows past cones at incidence. The stepback technique is a method for computing exactly flows which are truly conical, and can be an effective approximate method for nearly conical flows such as viscous flow past cones. The partial grid technique uses a stepback solution as the upstream boundary condition for a time-marching calculation, and is more accurate than the stepback method. Both frozen and chemically active equilibrium flow were considered, using the Ideal Dissociating Gas model. Computations were performed for frozen hypersonic flow past a 10° half-angle cone inclined at 24° incidence, and for hypervelocity flow past a 15° half-angle cone at 30° incidence with active dissociation and recombination chemistry. These computations were compared with experiments, and the effects of equilibrium and non-equilibrium chemistry were observed. These calculations also show that the effects of chemistry on heat transfer and separation location are small and of the same order as the errors associated with the stepback method. Therefore, for high accuracy in computing reacting flows, the partial grid method should be used.

Contents

List of Figures

List of Tables

Chapter 1

Introduction

A critical aspect of the design of reusable spacecraft is an accurate prediction of the flowfield during hypersonic atmospheric reentry. Wind tunnel testing is difficult for these flows, since the proper scaling of both viscous and chemical effects would require full-scale models at flight conditions. During reentry at a high angle of attack, dissociation and recombination reactions will significantly affect the flowfield. At such high angles of attack, complex shock-vortex systems develop on the leeward side of the reentry body, and these systems can cause intense heat transfer [7].

The non-equilibrium flow field is quite different than the frozen or equilibrium limits, and cannot be predicted by such simulations [8]. During the reentry of the maiden flight of the Space Shuttle Orbiter, the pitching moment was significantly different than the pre-flight predictions [9]. These predictions were based on cold hypersonic wind-tunnel test which could not reproduce real gas effects.

Here we study the hypervelocity flow past a cone at a high angle of attack. The cone is a simple body shape which results in a complex, fully three-dimensional flow pattern of the type expected to occur in more complex geometries. These flows are studied with two numerical techniques, the stepback method and the partial grid method. These methods are applied to frozen, equilibrium, and non-equilibrium flows, and the results are compared with experiments.

In the following sections we describe the basic features of cone flow and review some of the literature on the subject. In the later chapters we describe the numerical methods used, the chemistry model, and the special techniques used to simulate these cone flows. Then the details of the frozen zero incidence tests are given, followed by the reacting cone tests at incidence. The stepback method is shown to be a cheap and effective way to get approximate solutions for cone flows, and can be combined with a partial grid technique to get more accurate solutions.

1.1 General Features of Flow Past a Cone

Figure 1.1 shows some of the basic features of hypersonic cone flow for a cone at an angle of attack α, and defines some of the nomenclature used here. We will use coordinates (r, θ, ϕ) where r is the distance from the cone apex, and θ and ϕ are polar and azimuthal angles measured respectively from the cone surface and from the windward plane of symmetry. In the schematic of Figure 1.1, a fluid element from the freestream hits the bow shock first, and then expands around the cone. If it is sufficiently close to the plane of symmetry, the element will remain near the surface of the cone, and it will be processed by a leeward shock, which forms in order to turn the near-surface flow parallel to the leeward plane of symmetry. Behind the leeward shock, the flow separates and rolls up into one of a pair of symmetrical leeward vortices bisected by the leeward symmetry plane. If the fluid element is processed by the bow shock away from the windward plane of symmetry, it can, under certain conditions, avoid the leeward shock, and will either move into the vortex from the leeward plane of symmetry or approach a singular point which sits above the vortices on the leeward plane of symmetry [10]. General discussions of flow past cones can be found in Shapiro [11] and Anderson [12] and in papers by Marconi [13, 14, 15], Macrossan and Pullin [16], Smith [17], and Rainbird [18].

For supersonic flow past a cone, viscosity is not necessary to produce flow separation following the leeward shock system – an example of one of the few inviscid separation mechanisms. The leeward shock has a strength gradient; it is strongest at the cone surface, and becomes weaker away from the body. This results in an entropy gradient behind the leeward shock. From Crocco's theorem [12],

$$\mathbf{V} \times \boldsymbol{\omega} = \nabla h_0 - T \nabla s, \tag{1.1}$$

where T is temperature, s is entropy, h_0 is total enthalpy, $\mathbf{V}$ is the velocity vector, and $\boldsymbol{\omega}$ is the vorticity vector. There is no gradient of total enthalpy behind either the bow shock or the leeward shocks, since total enthalpy is conserved across shock waves. There is an entropy gradient behind the bow shock due to its curvature, and this generates vorticity upstream of the leeward shock. The entropy gradient of the leeward shock is similarly balanced by vorticity, and the accumulated vorticity is sufficient to cause crossflow separation behind the leeward shock. The presence of a viscous boundary layer will strongly influence the

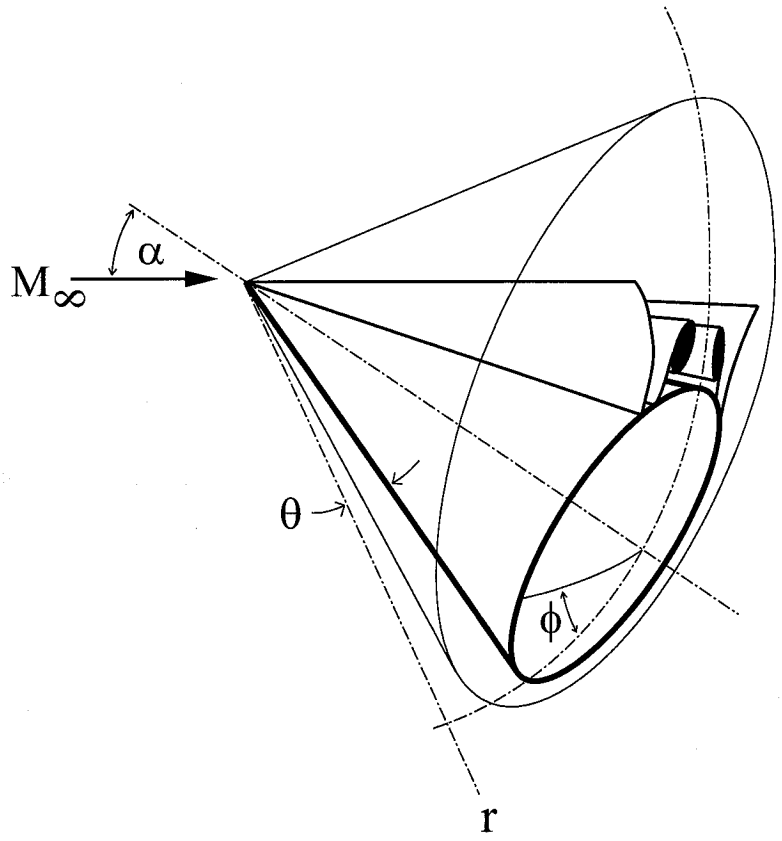

Figure 1.1 Schematic of major features of cone flow. α is the angle of incidence, r is the distance from the tip of the cone, θ is the angular distance away from the surface of the cone, and ϕ is the azimuthal angle, 0° at the windward side to 180° at the leeward side.

azimuthal position of the surface separatrix. The boundary layer will separate upstream of its inviscid separation point, and the displacement of the separated boundary layer causes the formation of a second branch of the shock wave, forming a λ-shock, so-called because of its resemblance to the shape of the letter.

1.2 Topology of the Flowfield

The topology of the flow can be examined through the use of crossflow streamlines. Crossflow streamlines are obtained by projecting the velocity field onto a surface, and integrating only these crossflow components of velocity. Crossflow streamlines can be projected onto a plane, but here the surface used is a sphere centered on the tip of the cone.

There are several critical points where the crossflow velocity is zero. Critical point theory

may be used to analyze the crossflow velocity field. An excellent discussion of critical point theory applied to flow fields may be found in Hunt et al. [19]. The Jacobian J and the divergence Δ may be used to classify the critical points. If the crossflow components of velocity are given by u_1 and u_2 and the coordinates on the surface are x_1 and x_2, then

$$J = \frac{\partial u_1}{\partial x_1}\frac{\partial u_2}{\partial x_2} - \frac{\partial u_1}{\partial x_2}\frac{\partial u_2}{\partial x_1} \tag{1.2}$$

and

$$\Delta = \frac{\partial u_1}{\partial x_1} + \frac{\partial u_2}{\partial x_2}. \tag{1.3}$$

There are two types of critical points: saddle points and node points. If $J < 0$, then the critical point is a saddle point. If $J > 0$, then it is a node point. There are two types of node points. A node is a regular node point if $J < \Delta^2/4$, and is a focus if $J > \Delta^2/4$. Furthermore, a focus is stable if $\Delta < 0$ and unstable if $\Delta > 0$.

Saddle points and regular node points may exist on the body surface. These are called half-saddle and half-node points, and physically correspond to separation points (for $\Delta < 0$) and reattachment points (for $\Delta > 0$). Foci correspond physically to vortices.

A topological rule specifies the relationship between the number of critical points in the crossflow field [19]. Let the connectivity of the domain be n, the number of saddle points and half-saddles be given by S and S', respectively, and the number of nodes and half-nodes be given by N and N', respectively. The crossflow flowfield must satisfy the relation

$$\left(\sum N + \frac{1}{2}\sum N'\right) - \left(\sum S + \frac{1}{2}\sum S'\right) = 1 - n, \tag{1.4}$$

where the critical points are summed over the entire flowfield (i.e., both sides of the body).

As mentioned above, the velocity field may be projected onto any surface. Some researchers have investigated crossflow topology for fields projected onto planes [20]. When projected onto a plane, the freestream is parallel to the line of symmetry and the connectivity $n = 2$. However, when the crossflow streamlines are projected onto a sphere, the freestream is directed radially inward everywhere, and $n = 1$. Here the projection on the

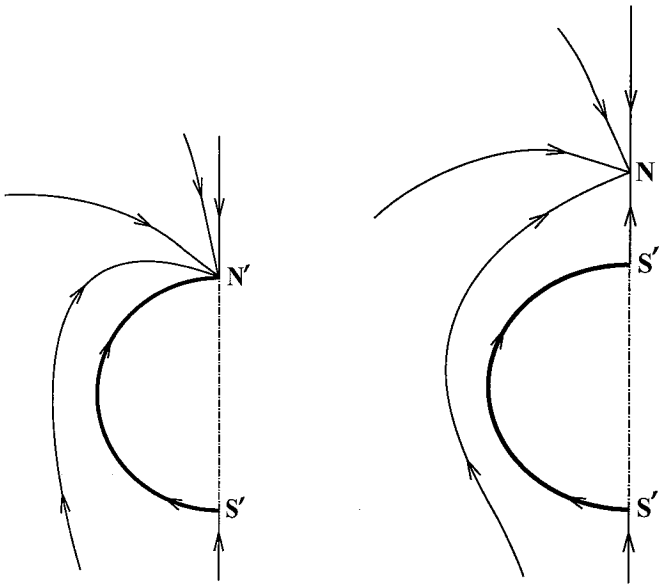

Figure 1.2 Topology of flow field for a cone with attached flow. Crossflow streamlines are plotted on a sphere centered at the tip of the cone. S and S′ denote saddle and half-saddle points, respectively. N and N′ denote node points and half-node points, respectively.

sphere is used, so

$$\left(\sum N + \frac{1}{2}\sum N'\right) - \left(\sum S + \frac{1}{2}\sum S'\right) = 0, \tag{1.5}$$

For a cone at a small angle of incidence, the flow will remain attached on the leeward side. The topology of this flowfield is shown in Figure 1.2. The stagnation point is a half-saddle and a half-node exists on the surface of the cone at the leeward plane. This half-node is the ultimate destination of all fluid passing the cone. Here, $S' = 1$, $N' = 1$, and Equation 1.5 is satisfied[1].

At a higher angle of incidence, but not high enough to cause separation, the half-node moves away from the surface of the cone and becomes a full node. This is also shown in Figure 1.2. When the node moves from the surface, it leaves a half-saddle on the cone at the leeward plane. The node is not a singularity, but is merely a crossflow critical point

[1]For the projection on a plane, this picture would be different. The flow would still expand around the cone, and feed into the node on the leeward side, but there will be a saddle point on the leeward plane of symmetry where the crossflow velocity goes to zero just inside the leeward portion of the bow shock. This saddle point divides the part of the crossflow domain which feeds into the half-node from the part which travels around the cone to eventually flow vertically far down the symmetry line. Here, $S' = 1$, $S = 1$, $N' = 1$, and $n = 2$, satisfying Equation 1.4.

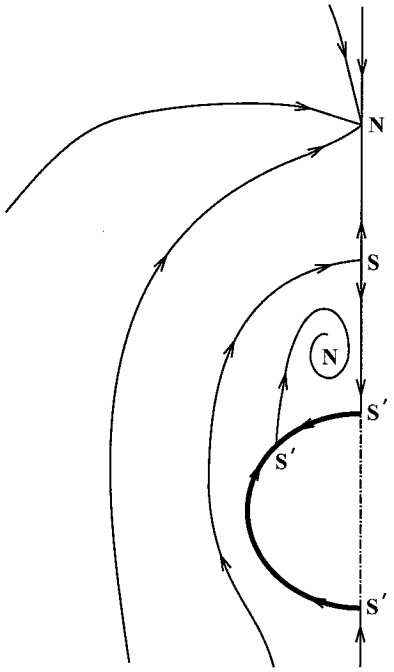

Figure 1.3 Topology of flow field for a cone with separated flow. Crossflow streamlines are plotted on a sphere centered at the tip of the cone. S and S′ denote saddle and half-saddle points, respectively. N denotes a node point.

where the velocity is purely radial. The node is still the final destination of all of the fluid. Here, $S' = 2$, $N = 1$, and Equation 1.5 is again satisfied.

At angles of incidence large enough to cause separation, the flowfield becomes more complex. This is shown in Figure 1.3. The separation point is a half-saddle point, feeding into the node corresponding to the vortex. The half-saddle which had been on the surface at lower incidence moves away from the cone, becoming a full saddle point, leaving another half-saddle on the surface at the leeward plane of symmetry. This streamline leading to the full saddle point is a dividing streamline between the fluid which enters the vortex and the fluid which does not. All of the fluid still ends up at the nodes, either at the node on the plane of symmetry or in one of the vortices. Recalling that both sides of the cone must be accounted for, $S = 1$, $S' = 4$, and $N = 3$, and the topological relation is again satisfied.

Even more complex flow patterns are possible. Secondary separation can occur on the leeward side of the cone, between the plane of symmetry and the separation point. If secondary separation occurs, it will be accompanied by the appearance of another node and a reattachment half-saddle point. Theoretically, any number of separations can occur on this region of the cone, which has been observed in numerical simulations of a hemisphere-

cylinder body at high incidence [20].

1.3 Literature Review

Various experiments have been performed on supersonic and hypersonic flow over cones, although most of the data are for small angles of incidence. Experimental measurements typically include heat transfer and surface pressure, and flow visualizations such as surface oil flow techniques.

Holt and Blackie [21] conducted one of the earliest experiments on supersonic cone flows. Two cones of half-angles 15° and 20° were tested at angles of incidence up to 25° for $M = 3.53$. Surface pressure was measured, and a pressure recovery was noted on the leeward surface when the angle of incidence exceeded the cone half-angle.

Experiments were performed by Tracy [5] on a 10° half-angle cone at incidences ranging from 0° to 24° incidence. Surface pressure and heat transfer were measured, and a pitot probe was traversed through the flowfield to determine its features. Tracy's results capture the development of the topological structure of the flow from low incidence to high incidence. Tracy found that at low angles of incidence, the pressure recovery on the leeward side grew with increasing incidence, but beyond incidences of about 8°, no further dependence on angle of incidence was observed. The separated region was found to be essentially conical and inviscid.

Rainbird [18] investigated two cones of half-angle 5° and 10°, up to incidences of 12.6° and 31.5°, respectively. Tests were performed at $M = 1.80$ and $M = 4.25$. Rainbird showed that for low incidences, an unseparated inviscid calculation is sufficient for predicting the flow. However, to calculate flow at higher incidences, an inviscid model with free vortex sheets would be necessary.

A 5° cone at $M = 5$ and at various angles of attack was studied by Feldhuhn and Winkelman [22]. Surface pressure measurements and pitot flowfield surveys were conducted. It was established that the flowfield on the leeward surface of the cone at large incidence was the results of the interaction between the viscous and inviscid regions of the flow.

Few experiments have measured real gas effects. Krek [6] performed high-enthalpy experiments on a 15° cone at 30° incidence in a $M = 5$ flow in a free piston shock tunnel. Surface pressure and heat transfer were measured, and inviscid EFM calculations were per-

formed for comparison. These experiments offered a challenging benchmark for validating simulations.

Similarly, Wen [23] conducted experiments on hypervelocity flow over spheres in a shock tunnel. Although this is not a cone flow, the analysis of the dissociating flow over blunt bodies is relevant to the shock standoff scaling. An analytical correlation was developed to correlate the reaction rate parameter with the standoff distance.

Three-dimensional viscous flows are very difficult to compute, and involve complex flow-fields with separation, shock/boundary layer interactions, and viscous regions embedded in regions of essentially inviscid flow. Early attempts at computing cone flows were restricted to low incidence, inviscid cones. The solutions involved perturbation methods based on the exact inviscid Taylor-Maccoll solution [24]. The original perturbation solutions were formulated by Stone [25, 26], but Ferri [27] showed that the analysis was incorrect near the leeward symmetry point for a cone at incidence. Cheng [28] was able to correct the problem with the Stone theory by obtaining an explicit expression for the entropy distribution in the flow field. However, none of these low incidence results are applicable to the more complex flow fields we are interested in.

Marconi [13] computed the three-dimensional supersonic inviscid flow about slender cones at large incidences. Marconi suggested that there are two possible sources of additional vorticity (beyond the vorticity due to the bow shock). The first is the strength gradient in crossflow shock waves, and the second is vorticity shed from the boundary layer at the separation point. Only the former is possible in inviscid flow. Then Marconi [14] used an inviscid shock-fitting scheme to simulate the inviscid flow past a 5° cone at 12.35° incidence. Shock fitting was used to calculate the positions of the bow shock and the leeward shock, and inviscid separation was predicted behind, not at, the crossflow shock. For cases with supersonic reverse crossflow in the separated region, a reverse crossflow shock could form, which could induce secondary separation. Calculations were made by Marconi [15] for a 10° cone at two Mach numbers, $M = 5$ and $M = 10$. The angle of incidence was varied from 10° to 25° to study the development of the shock-vortex system with increasing incidence. For angles of incidence less than the cone half-angle, no crossflow shocks were observed. At high incidences, more complex shock-vortex systems with secondary separation were observed.

Finally, Macrossan and Pullin [16] studied reacting inviscid flow past a 15° cone at 30° incidence using the Equilibrium Flux Method. Frozen, non-equilibrium, and equilibrium

flows were investigated. The effects of chemistry on the windward shock standoff distance and the vortex size and shape were examined. The equilibrium cases separated later than the frozen cases, and the surface pressure for the non-equilibrium case was not bracketed by the frozen and equilibrium solutions.

Chapter 2

Equations of Motion and Numerical Methods

This chapter describes the numerical methods used for this thesis. The two algorithms used in these simulations for calculating fluxes are the Equilibrium Flux Method (EFM), and the EFMO Method (which stands for EFM-Osher). This chapter also discusses the stepback technique, which is used for approximately conical flows.

2.1 The Inviscid Equilibrium Flux Method

EFM [1] is a finite volume technique for solving the inviscid Euler equations of compressible ideal gas flow. It is a kinetic-based flux-split method which is extremely robust, but suffers from high numerical diffusion in its first-order form. It can handle extremely strong shocks well and does not suffer from some of the failings of other methods (e.g. the carbuncle phenomenon [29]). It has no fixes or tunable parameters, and is entropy-satisfying [30] and positivity-preserving [31]. However, the price of high stability is large numerical diffusion.

2.1.1 Derivation

EFM is derived from the Boltzmann equations in the limit of infinite collision rate within cells, between successive applications of the convective phase of motion. The numerical flux functions at the interfaces between adjacent cells are evaluated using a split Maxwellian molecular velocity distribution.

Consider the Boltzmann equation [32] for a spatial and temporal distribution $f(\mathbf{c}, \mathbf{x}, t)$ of molecular velocities $\mathbf{c}$. If there are no external forces acting, there will be no convection in velocity space and the equation reduces to

$$\frac{\partial}{\partial t}(nf) + \mathbf{c} \cdot \frac{\partial}{\partial \mathbf{x}}(nf) = \left[\frac{\partial}{\partial t}(nf)\right]_{collisions}, \tag{2.1}$$

where $n(\mathbf{x}, t)$ is the molecular number density. The molecular state is given by the vector

Q consisting of the quantities $[m, m\mathbf{c}, \frac{1}{2}\mathbf{c}\cdot\mathbf{c}]$ By taking the moments of (2.1) with Q, one can obtain a set of conservation equations for a gas obeying Boltzmann's equation. First, a moment of this phase space distribution is obtained through

$$\langle Q \rangle = \int_c (nf) Q d\mathbf{c}. \tag{2.2}$$

This can be applied to a computational cell as follows. Consider one face of a computational cell in physical space with volume V and surface area S. Define a local set of coordinates $(\hat{\mathbf{n}}, \hat{\mathbf{p}}, \hat{\mathbf{q}})$ such that $\hat{\mathbf{n}}$ is normal to the cell face and points outward, and $\hat{\mathbf{p}}$ and $\hat{\mathbf{q}}$ lie in the face and form an orthogonal basis (see Figure 2.1). In general, a cell face need not be planar (it can be a curved surface), so $\hat{\mathbf{p}}$ and $\hat{\mathbf{q}}$ will lie approximately in the plane of the face; in practice, however, these surfaces are planes.

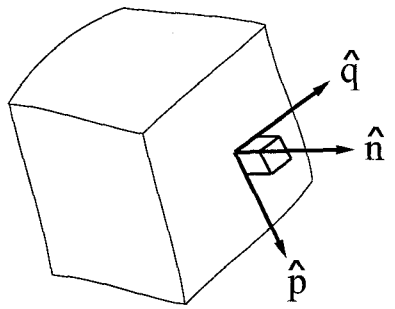

Figure 2.1 Local coordinate axis at a cell interface

We can integrate the moments of the Boltzmann equation over the cell volume and apply the divergence theorem to the convection term to obtain

$$\frac{\partial}{\partial t} \iiint_V U_Q \, dV + \iint_S F_Q \, dS = 0, \tag{2.3}$$

where U_Q is a set of conserved quantities per unit volume given by

$$U_Q = \int_c (nf) \, Q \, dc \tag{2.4}$$

and F_Q is a set of fluxed quantities given by

$$F_Q = \int_c (nf)\, Q\, \mathbf{c} \cdot \hat{\mathbf{n}}\, d\mathbf{c}. \tag{2.5}$$

The integral of the collision term from the Boltzmann equation is zero, since the molecular quantites Q are conserved in each collision.

2.1.2 Flux Splitting

The flux term F_Q contains both outward and inward fluxes. It can be decomposed into two parts, an outward or *forward* moving flux F_Q^+, and an inward or *backward* moving flux F_Q^-, so that

$$F_Q = F_Q^+ + F_Q^-. \tag{2.6}$$

Consider the one-dimensional schematic of Figure 2.2. Let c be the component of molecular

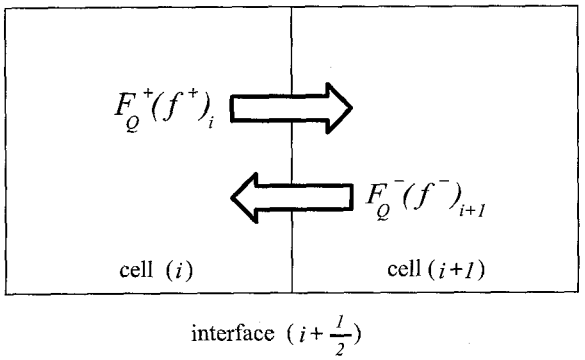

Figure 2.2 Forward and backward fluxes at cell interface $i+\frac{1}{2}$, between cell i and $i+1$

velocity normal to the interface between two cells labelled by i and $i+1$, where $x_{i+1} > x_i$. The velocity distribution contains positive and negative values, and the distribution can be split into its backward and forward moving components, expressed as

$$f^-(c) = f(c), \quad c < 0 \qquad \text{and} \qquad f^+(c) = f(c), \quad c > 0. \tag{2.7}$$

In the cell-based coordinate system, the forward and backward fluxes become

$$F_Q^+ = \int_{-\infty}^{\infty}\int_{-\infty}^{\infty}\int_{0}^{\infty} (n^+ f^+)\, Q\, c_n\, dc_n\, dc_p\, dc_q \tag{2.8}$$

and

$$F_Q^- = \int_{-\infty}^{\infty}\int_{-\infty}^{\infty}\int_{-\infty}^{0} (n^- f^-)\, Q\, c_n\, dc_n\, dc_p\, dc_q. \tag{2.9}$$

The flux through the interface between cells (i) and $(i+1)$ is equal to the sum of the forward flux from cell (i) and the backward flux from cell $(i+1)$ (see Figure 2.2).

2.1.3 Equilibrium Distribution

Once the distribution function f is known, the fluxes F_Q^+ and F_Q^- can be calculated analytically to yield the transport of mass, momentum, and energy across the cell surface. EFM follows from the assumption that the gas in every cell is in local equilibrium, so that the molecular velocity distribution is given everywhere by the Maxwellian distribution. The Maxwellian distribution is defined here in terms of $\mathbf{v}$ and β, where $\mathbf{v} = \overline{\mathbf{c}}$ is the mean molecular velocity (which is the local flow velocity) and β is the reciprocal of the most probable thermal speed, defined by

$$\beta = \frac{1}{\sqrt{2RT}}, \tag{2.10}$$

where R is the gas constant, and T is the local temperature. The Maxwellian distribution is defined as

$$f = f_0(c;\beta,v) = \left(\frac{\beta^3}{\pi^{3/2}}\right) \exp\left[-\beta^2(c-v)^2\right], \tag{2.11}$$

where the notation emphasizes that the primary dependence of f is on c, while β and v are parameters. Considering again the one-dimensional case of Figure 2.2, the total velocity

distribution at the interface is

$$f_0^-(c) = f_0(c; \beta_{i+1}, v_{i+1}), \qquad c < 0 \tag{2.12}$$

$$f_0^+(c) = f_0(c; \beta_i, v_i), \qquad c > 0. \tag{2.13}$$

The split Maxwellian distribution is illustrated in Figure 2.3.

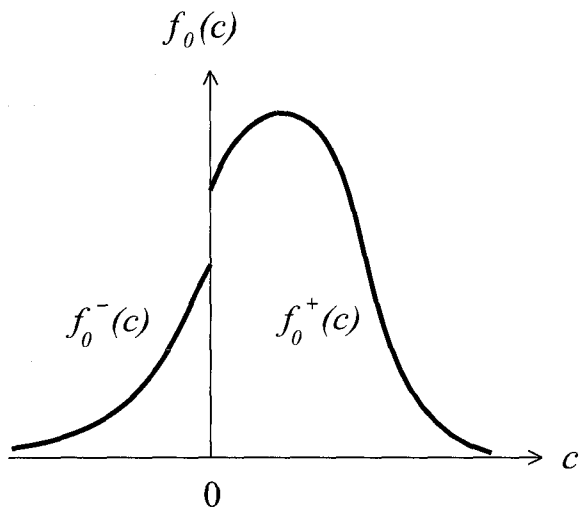

Figure 2.3 Split Maxwellian distribution. $f_0^-(c)$ is the backward moving part of the distribution from cell $i+1$, and $f_0^+(c)$ is the forward moving part of the distribution from cell $i-1$.

2.1.4 Flux Expressions

Once f is assumed to have a Maxwellian distribution, the EFM fluxes can be analytically calculated. Using the local $(\hat{\mathbf{n}}, \hat{\mathbf{p}}, \hat{\mathbf{q}})$ coordinate system, for a frozen inviscid gas, the fluxes

are given by

$$F_Q^{\pm}\begin{pmatrix} m \\ mv_n \\ mv_p \\ mv_q \\ \frac{1}{2}mV^2 \end{pmatrix} = \begin{pmatrix} \rho(\frac{D^{\pm}}{\beta} + v_n W^{\pm}) \\ \rho(\frac{D^{\pm}}{\beta} + v_n W^{\pm})v_n + pW^{\pm} \\ \rho(\frac{D^{\pm}}{\beta} + v_n W^{\pm})v_p \\ \rho(\frac{D^{\pm}}{\beta} + v_n W^{\pm})v_q \\ \rho(\frac{D^{\pm}}{\beta} + v_n W^{\pm})\left[\frac{V^2}{2} + \left(\frac{\gamma+1}{\gamma-1}\right)\frac{1}{4\beta^2}\right] + \frac{1}{2}pv_n W^{\pm} \end{pmatrix} \tag{2.14}$$

where p is the pressure and ρ is the density. Other terms in this expression are the magnitude of velocity V, given by

$$V^2 = v_n^2 + v_p^2 + v_q^2, \tag{2.15}$$

the so-called "weighting factors" W, given by

$$W^{\pm} = \frac{1}{2}[1 \pm \mathrm{erf}(s^{\pm})], \tag{2.16}$$

the "dissipation terms" D, given by

$$D^{\pm} = \frac{1}{2\sqrt{\pi}}\exp\left[-(s^{\pm})^2\right], \tag{2.17}$$

and the "speed ratio" s, given by

$$s^{\pm} = v_n^{\pm}\beta^{\pm}. \tag{2.18}$$

The error functon (erf) is defined as

$$\mathrm{erf}(s) = \frac{2}{\sqrt{\pi}}\int_0^s \exp(-t^2)dt. \tag{2.19}$$

Numerically, a rational approximation to the error function is used [33] to calculate the fluxes.

The momentum fluxes are calculated in the local coordinate system and must be trans-

formed back to the global coordinates using

$$F_Q \begin{pmatrix} mv_x \\ mv_y \\ mv_z \end{pmatrix} = \begin{pmatrix} F_Q(mv_n)n_x + F_Q(mv_p)p_x + F_Q(mv_q)q_x \\ F_Q(mv_n)n_y + F_Q(mv_p)p_y + F_Q(mv_q)q_y \\ F_Q(mv_n)n_z + F_Q(mv_p)p_z + F_Q(mv_q)q_z \end{pmatrix}. \tag{2.20}$$

The state array U_Q of mass, momentum and energy of each cell can be updated using Euler integration by simply summing the contributions from each face

$$\Delta U_Q = \sum_{faces} F_Q A \Delta t \tag{2.21}$$

where A is the area of the face and Δt is the timestep. Of course, more sophisticated time integration techniques may be used for higher accuracy in time.

2.1.5 Dissipation

It has been shown that EFM may be considered a finite volume solution method for the Euler equations with added "pseudo-dissipative" terms [34]. These dissipation terms are not an artificial viscosity which may be adjusted as desired. Rather, they arise from the simulation of the flow at the molecular level. One of the assumptions of EFM involves taking the equilibrium limit, or the limit as the collision rate goes to infinity. This would correspond to a zero mean free path. However, it can be shown that there is an effective mean free path which scales approximately with the cell size [34]. The excessive dissipation may be responsible for the robustness of EFM. For high resolution simulations, the excessive dissipation may be significantly reduced due to the smaller mean free path. No adverse effects (e.g., stability problems) due to the decreased viscosity have been observed for the high resolution simulations presented here.

However, no adverse effects of this (e.g., stability problems) have been observed for the high resolution simulations performed here.

2.1.6 Inviscid Boundary Conditions

The boundary conditions are implemented via dummy cells which border the computational domain. There are several basic boundary conditions, which include freestream

conditions, a body surface, a plane of symmetry, or zero gradient. All but the body surface are self-explanatory.

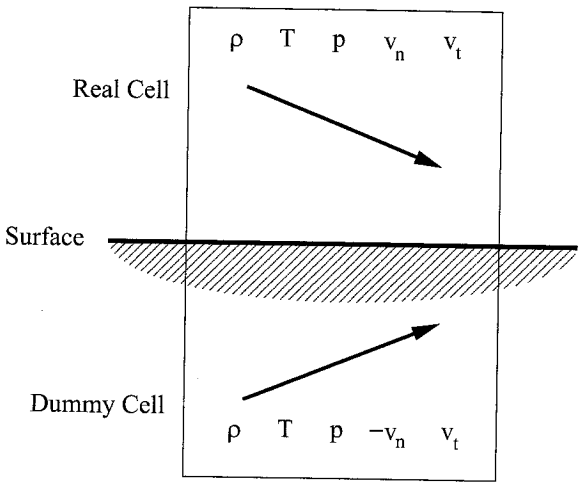

Figure 2.4 Inviscid surface boundary condition

For the Euler equations, there can be no mass or energy flux through a surface, although a slip velocity tangential to the surface may exist. In order to enforce this, the dummy cells across the body surface are assumed to have the same density and temperature as their neighboring cells, but the velocity vector of the dummy cell is reflected about the cell surface (see Figure 2.4). Fluxes are calculated for the surface interface in the same manner as any other interface, and the dummy cell's state is updated appropriately at the beginning of each timestep.

2.1.7 Estimation of Gradients and Higher-Order Methods

The basic EFM is first-order accurate in space. Higher-order methods may be obtained through the use of flux-limiters and slope-limiters. The idea of limiters is to get higher-order accuracy away from shock waves while maintaining monotonicity. With a flux-limiter, a numerical viscosity is added to the system, but its contribution is scaled by a factor which depends on the limiter. There are several well-known flux-limiters, such as van Leer's flux-limiter [35] and Roe's "superbee" limiter [36], but here the approach has been to use a slope-limiter.

The first-order method uses a piecewise constant representation of the state variables;

the cell is assumed to have a constant state equal to the state at the cell centroid, and this state is used to calculate the flux at the interface. However, a more realistic approach is to use a piecewise *linear* reconstruction by assuming that the state in the cell varies linearly from the state at the centroid to the state at the neighboring cell's centroid. Consider the variation of states in one direction, as in Figure 2.5. The state in cell i is given by U_Q^i, and the states in the neighboring cells *i-1* and *i+1* are U_Q^{i-1} and U_Q^{i+1}, respectively. We can represent the the variation over cell i by replacing U_Q^i with $\tilde{U}_Q(x)$, where $x_{j-\frac{1}{2}}$ corresponds to the left interface, and $x_{j+\frac{1}{2}}$ corresponds to the right interface. For example,

$$\tilde{U}_Q(x) = U_Q^i + \sigma^i(x - x_j); \qquad x_{j-\frac{1}{2}} < x < x_{j+\frac{1}{2}}, \tag{2.22}$$

where σ^i is the slope of $\tilde{U}_Q$ in cell i. Note that the average cell value is still U_Q^i, and for the first-order method, $\sigma^i = 0$.

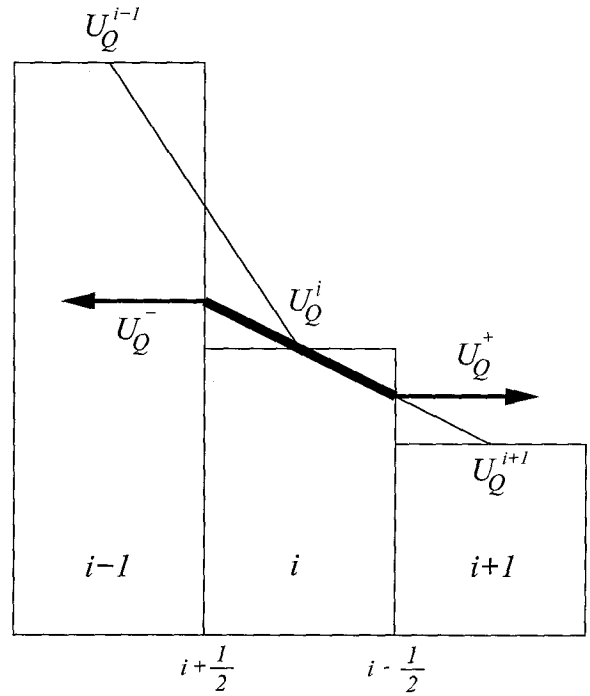

Figure 2.5 Estimation of gradients using min-mod

There are several choices one can make for σ^i. With the proper selection, the method may be made monotonic and total variation diminishing (TVD) [37]. Van Leer's minmod method [38] can be shown to be TVD, and is the limiter used here. The minmod limiter

uses the minmod function, which is based on the sign function (or sgn), where

$$\text{sgn}(x) = \begin{cases} -1, & x < 0 \\ 0, & x = 0 \\ 1, & x > 0 \end{cases} \tag{2.23}$$

and the minmod function is given by

$$\text{minmod}(a, b) = \frac{1}{2}\left[\text{sgn}(a) + \text{sgn}(b)\right] \min(|a|, |b|), \tag{2.24}$$

where the min function returns the minimum value of its two arguments. Therefore, the minmod function can also be given by

$$\text{minmod}(a, b) = \begin{cases} a, & |a| < |b|, \; ab > 0 \\ b, & |b| < |a|, \; ab > 0 \\ 0, & ab < 0 \end{cases} . \tag{2.25}$$

Consider cells $(i-1)$, (i), and $(i+1)$ as shown in Figure 2.5. The gradients at the faces of cell i are estimated linearly using the values of the neighboring cells. If the state variable is a local extremum, then the gradients will be of opposite sign, and zero gradient is assumed (the state is assumed to be the same at both interfaces as it is in the cell). In this case, the algorithm reverts to first-order. If the gradients are of the same sign, then the lesser of the two gradients is used to estimate properties at both cell interfaces (U_Q^- and U_Q^+). These properties are then used to evaluate the fluxes. If the centroids of cells $(i-1)$, (i), and $(i+1)$ are x^{i-1}, x^i, and x^{i+1}, respectively, then the minmod slope limiter can be used to find the value of σ^i with

$$\sigma^i = \text{minmod}\left[\left(\frac{U_Q^{i+1} - U_Q^i}{x^{i+1} - x^i}\right), \left(\frac{U_Q^i - U_Q^{i-1}}{x^i - x^{i-1}}\right)\right]. \tag{2.26}$$

This can be applied separately in each dimension in order to project the states onto the appropriate interfaces.

2.2 Viscous EFM

EFM was designed for the Euler equations. In order to implement EFM for the Navier-Stokes equations, dissipative terms must be introduced to model the effects of viscosity. This can be done at two levels. Microscopically, the dissipation may be introduced at the molecular level by changing the assumed velocity distribution to incorporate viscosity. Recall that one of the assumptions of EFM is that the molecular velocities in each cell conform to the Maxwellian distribution (see Section 2.1.3). One may rederive viscous flux expressions based on a different molecular velocity distribution, such as the Chapman-Enskog distribution [39].

Alternatively, viscous effects can be introduced at the macroscopic level by adding corrections to the flux expressions. This is the more typical approach and is the one used in these studies.

2.2.1 Viscous Flux Terms and Transport Properties

The viscous stress tensor σ_{ij} can be written as

$$\sigma_{ij} = \begin{bmatrix} \sigma_{xx} & \sigma_{xy} & \sigma_{xz} \\ \sigma_{yx} & \sigma_{yy} & \sigma_{yz} \\ \sigma_{zx} & \sigma_{zy} & \sigma_{zz} \end{bmatrix}. \tag{2.27}$$

The stress tensor for the Navier-Stokes equations may be split into pressure and viscous terms τ_{ij}, so that

$$\sigma_{ij} = -p\,\delta_{ij} + \tau_{ij}. \tag{2.28}$$

The viscous term is

$$\tau_{ij} = \mu\left(\frac{\partial u_i}{\partial x_j} + \frac{\partial u_j}{\partial x_i}\right) + \delta_{ij}(\nabla\cdot\mathbf{v})\left(\mu_v - \frac{2}{3}\mu\right), \tag{2.29}$$

where μ is the coefficient of shear viscosity and μ_v is the coefficient of bulk viscosity [40]. Similarly, the flux terms can be decoupled into inviscid and viscous terms, and the viscous contributions to the flux may be calculated separately. The resulting viscous corrections to

the flux are

$$F_Q \begin{bmatrix} m \\ mv_x \\ mv_y \\ mv_z \\ me \end{bmatrix} = \begin{bmatrix} F_Q(m)_{inviscid} \\ F_Q(mv_x)_{inviscid} - \tau_{xx}n_x - \tau_{xy}n_y - \tau_{xz}n_z \\ F_Q(mv_y)_{inviscid} - \tau_{yx}n_y - \tau_{yy}n_y - \tau_{yz}n_z \\ F_Q(mv_z)_{inviscid} - \tau_{zx}n_x - \tau_{zy}n_y - \tau_{zz}n_z \\ \begin{aligned} F_Q(me)_{inviscid} &- n_x\{v_x\tau_{xx} + v_y\tau_{xy} + v_z\tau_{xz} - q_x\} \\ &- n_y\{v_x\tau_{yx} + v_y\tau_{yy} + v_z\tau_{yz} - q_y\} \\ &- n_z\{v_x\tau_{zx} + v_y\tau_{zy} + v_z\tau_{zz} - q_z\} \end{aligned} \end{bmatrix}, \tag{2.30}$$

where n is the direction normal to the interface, e is the total energy and q is the heat transfer.

EFM is a shock-capturing scheme and will therefore smear shock waves over several cells. This justifies the assumption of Stokes' hypothesis that $\mu_v = 0$. Bulk viscosity will be important only very near shock waves, and since we do not resolve the fine-scale structure of shocks, it can be neglected. With this assumption, the shear stress and heat transfer terms become

$$\begin{bmatrix} \tau_{xx} \\ \tau_{yy} \\ \tau_{zz} \\ \tau_{xy} \\ \tau_{zx} \\ \tau_{zy} \end{bmatrix} = \begin{bmatrix} \frac{2}{3}\mu\left(2\frac{\partial u}{\partial x} - \frac{\partial v}{\partial y} - \frac{\partial w}{\partial z}\right) \\ \frac{2}{3}\mu\left(2\frac{\partial v}{\partial y} - \frac{\partial w}{\partial z} - \frac{\partial u}{\partial x}\right) \\ \frac{2}{3}\mu\left(2\frac{\partial w}{\partial z} - \frac{\partial u}{\partial x} - \frac{\partial v}{\partial y}\right) \\ \mu\left(\frac{\partial u}{\partial y} + \frac{\partial v}{\partial x}\right) \\ \mu\left(\frac{\partial w}{\partial x} + \frac{\partial u}{\partial z}\right) \\ \mu\left(\frac{\partial v}{\partial z} + \frac{\partial w}{\partial y}\right) \end{bmatrix} \tag{2.31}$$

and

$$\begin{bmatrix} q_x \\ q_y \\ q_z \end{bmatrix} = -k \begin{bmatrix} \frac{\partial T}{\partial x} \\ \frac{\partial T}{\partial y} \\ \frac{\partial T}{\partial z} \end{bmatrix}, \tag{2.32}$$

where k is the thermal conductivity coefficient.

For frozen flows, Sutherland's law is used to calculate viscosity [41]. Sutherland's formula

Gas	$\mu_0 \left(\frac{kg}{m \cdot s}\right)$	T_0 (K)	S (K)
Nitrogen	1.663×10^{-5}	273	106.7
Oxygen	1.919×10^{-5}	273	138.9
Air	1.716×10^{-5}	273	110.6

Table 2.1 Parameters for Sutherland's law

is a three-parameter rule, with a reference viscosity μ_0, a reference temperature T_0, and the Sutherland constant S.

$$\mu = \mu_0 \left(\frac{T}{T_0}\right)^{1.5} \left(\frac{T_0 + S}{T + S}\right) \tag{2.33}$$

The code used for these studies can accommodate three gases: nitrogen, oxygen, and air. The Sutherland parameters for these gases are shown in Table 2.1. For frozen flows, a constant Prandtl number (Pr) is assumed, where Pr is defined as

$$Pr = \frac{\mu\, C_p}{k}, \tag{2.34}$$

where $C_p = \gamma R/(\gamma - 1)$ is the specific heat at constant pressure, and the conductivity is calculated by inverting the definition of the Prandtl number,

$$k = \frac{\mu\, C_p}{Pr}. \tag{2.35}$$

Section B discusses the treatment of viscosity and conductivity for reacting flows.

2.2.2 Viscous Boundary Conditions

For viscous flows, the surface boundary condition must be treated differently than for inviscid flows. The no-slip boundary condition means that the velocity at the wall must be zero. This is satisfied by setting the velocity in the dummy cell to be the opposite of the velocity in the first cell. With a second-order reconstruction, the velocity at the surface will be zero, and the mass flux will also be zero. The pressure (and degree of dissociation for reacting flows) is set to be the same as the first cell, so that there is zero momentum flux through the surface.

There are two different viscous boundary conditions treated here: adiabatic and isothermal. For the adiabatic case, there is no heat transfer through the surface, or

$$\nabla T \cdot \hat{n} = 0, \tag{2.36}$$

where T is the temperature, and $\hat{n}$ is the unit vector normal to the surface. This is enforced by setting the temperature of the dummy cell to be equal to the temperature in the first cell. Since we have already dictated that the pressure be equal across the surface, this requires that the density in the dummy cell is equal to that of the first cell. In fact, for the adiabatic boundary condition, the state in the dummy cell is equivalent to the state in the first cell, but with opposite velocity, so there can be no energy flux across the surface.

For the isothermal case, the temperature in the dummy cell is set to the prescribed wall temperature,

$$T = T_w, \tag{2.37}$$

and the density is chosen so that the pressure is constant across the surface, as discussed above. This allows for zero mass and momentum flux, and non-zero energy flux across the surface.

2.3 EFMO

EFM is a flux-vector splitting (FVS) scheme. These schemes tend to be very robust in terms of capturing strong shocks, although they lead to excessive numerical diffusion. EFM is typical in these regards. Another type of scheme is a flux-difference scheme (FDS), which are generally not good for strong shocks, but are very accurate for viscous flow because they capture stationary contact discontinuities exactly. The EFMO method, due to Moschetta and Pullin [2] is an attempt to blend the desirable properties of both types of methods. The blending of FVS and FVD schemes is based on the simple wave approach used in Osher's scheme [42].

Osher's numerical flux can be written as

$$F(U_L, U_R) = \frac{1}{2}\left[F_L + F_R - \int_{LN} |A|dw - \int_{NL} |A|dw\right], \tag{2.38}$$

where $|A| = A^+ - A^-$ and $A^{\pm}$ is the Jacobian of the fluxes $F^{\pm}$. The first integral is taken on a linearly degenerate subpath which corresponds physically to a contact discontinuity, and the second integral is taken on nonlinear subpaths which correspond to compression or rarefaction waves. The idea of EFMO was to put the EFM flux into a form similar to Osher's flux and replace the integral corresponding to the contact discontinuity by the one from Osher's flux. This results in an antidiffusive flux which almost vanishes in the vicinity of shocks, but removes the excessive numerical dissipation near contact surfaces.

In practice, the EFMO algorithm works as follows: Given two states U_L and U_R, one must find two intermediate states U_1 and U_2. These intermediate states sit on either side of a contact discontinuity, and are connected to the real states U_L and U_R via compression or rarefaction waves. Antidiffusive EFM fluxes are calculated in the regular manner based on states U_1 and U_2, and these fluxes are used to modify the standard EFM fluxes.

While the numerical flux for EFM is defined as

$$F_{EFM}(U_L, U_R) = F^+(U_L) + F^-(U_R), \tag{2.39}$$

the EFMO flux is defined as

$$F_{EFMO}(U_L, U_R) = F_{EFM}(U_L, U_R) + \Delta F, \tag{2.40}$$

where ΔF is the antidiffusive flux correction.

The intermediate states U_1 and U_2 are determined by the following equations:

$(L) - (1)$, *nonlinear subpath*

$$\frac{p_L}{\rho_L^{\gamma}} = \frac{p_1}{\rho_1^{\gamma}}, \tag{2.41}$$

$$v_{n_L} + \frac{2\varepsilon}{\gamma - 1} a_L = v_{n_1} + \frac{2\varepsilon}{\gamma - 1} a_1, \tag{2.42}$$

$$v_{p_L} = v_{p_1}, \tag{2.43}$$

$$v_{q_L} = v_{q_1}, \tag{2.44}$$

$(1) - (2)$, *linear subpath*

$$v_{n_1} = v_{n_2} = v_n{}^*, \tag{2.45}$$

$$p_1 = p_2 = p^*, \tag{2.46}$$

$(2) - (R)$, *nonlinear subpath*

$$\frac{p_2}{\rho_2^{\gamma}} = \frac{p_R}{\rho_R^{\gamma}}, \tag{2.47}$$

$$v_{n_2} - \frac{2\varepsilon}{\gamma - 1}\, a_2 = v_{n_R} - \frac{2\varepsilon}{\gamma - 1} a_R, \tag{2.48}$$

$$v_{p_2} = v_{p_R}, \tag{2.49}$$

$$v_{q_2} = v_{q_R}, \tag{2.50}$$

where p, ρ, γ, and a are respectively the pressure, density, ratio of specific heats, and speed of sound, and v_n, v_p, and v_q are the velocity components in a local axis where v_n is the velocity component normal to the interface, and v_p and v_q are the components of velocity tangential to the interface. $v_n{}^*$ and p^* are the normal velocity and pressure at the contact discontinuity.

The number ε governs the order of the states. For $\varepsilon = 1$, the left and right states are connected via a compression wave, the contact discontinuity, and then a rarefaction wave. For $\varepsilon = -1$, the states are connected via a rarefaction wave, the contact discontinuity, and a compression wave. These different paths are known as the natural order and the reverse order, respectively. Osher originally proposed using the reverse order, but other researchers have suggested that the natural order is preferable for some situations [2].

In fact, it is more appropriate to select the order for each interface, rather than using the same order for the whole grid. At the local interface level, using the wrong order can produce nonphysical fluxes, since the method will solve the Riemann problem with the locations of the compression and rarefaction waves switched. In practice, this does not seem

to affect the overall solution for many problems, and and may surprisingly improve stability for certain problems. However, it is more rigorous to choose ε so that the compression wave lies closest to the lower pressure state, so that

$$\varepsilon = \begin{cases} 1, & p_L \leq p_R \\ -1, & p_L > p_R \end{cases} . \tag{2.51}$$

The algorithm for finding the intermediate states U_1 and U_2 is outlined in Appendix A. Once U_1 and U_2 are determined, the antidiffusive flux can be calculated from

$$\Delta F = \begin{cases} -F^-(U_2) + F^-(U_1), & v_n^* > 0 \\ +F^+(U_2) - F^+(U_1), & v_n^* \leq 0 \end{cases} , \tag{2.52}$$

so that ultimately

$$F_{EFMO}(U_L, U_R) = \begin{cases} F^+(U_L) + F^-(U_R) - F^-(U_2) + F^-(U_1), & v_n^* > 0 \\ F^+(U_L) + F^-(U_R) + F^+(U_2) - F^+(U_1), & v_n^* \leq 0 \end{cases} . \tag{2.53}$$

The antidiffusive correction reduces the magnitude of most of the fluxes, although the normal momentum flux tends to be larger with the correction. The greatest relative correction is for the energy flux, which can be reduced by as much as 40% by the antidiffusive correction.

2.4 Chemistry

The introduction of dissociation chemistry to EFM requires another state variable, the degree of dissociation α. For a mixture of molecules A_2 and dissociated atoms A, the degree of dissociation gives the ratio of the dissociated A atoms to the total number of A atoms, or

$$\alpha = \frac{[A]}{[A] + 2\,[A_2]} . \tag{2.54}$$

There is no consideration of diffusion of species, and there are no boundary conditions applied to α at the wall. This is equivalent to a non-catalytic wall boundary condition.

2.4.1 Ideal Dissociating Gas Model

The Lighthill [3] Ideal Dissociating Gas (IDG) model with the Freeman [4] reaction rate is used to represent the chemical dynamics of the flow. This is a simple one-temperature model which is adequate for assessing the first-order effects of gas-chemistry interaction at temperatures of up to 7000 K. There are also other alternatives for more complex chemistry, such as Park's two-temperature model [43].

Consider the flow of pure nitrogen. The dissociation reactions

$$N_2 + N \overset{k_1}{\rightleftarrows} 2N + N \tag{2.55}$$

$$N_2 + N_2 \overset{k_2}{\rightleftarrows} 2N + N_2 \tag{2.56}$$

can be treated in either equilibrium or non-equilibrium modes. The degree of dissociation α is given by $\alpha = [N]/([N] + 2[N_2])$, and the effective gas constant for the mixture is $R = (1 + \alpha)R_{N_2}$. This means that the equation of state is given by

$$p = \rho(1 + \alpha)R_{N_2}T, \tag{2.57}$$

where p is the pressure, ρ is the density, T is the temperature, and R_{N_2} is the gas constant for the diatomic species.

For the mixture, the internal energy e_{int} consists of the sum of the random translational energy e_{tr}, the energy in the molecular structure e_{st} and the chemical potential energy, or dissociation energy e_{diss}. The structural energy can be further decomposed into rotational energy e_{rot} and vibrational energy e_{vib}. So

$$e_{int} = e_{tr} + e_{rot} + e_{vib} + e_{diss} \ . \tag{2.58}$$

The first three terms are modeled by the specific heat at constant volume C_v, which is constant for the IDG model ($C_v = 3R_{N_2}$). The dissociation energy is equal to $\alpha\,\theta_d R_{N_2}$, where θ_d is the characteristic dissociation temperature, a gas constant. Therefore the total internal energy is given by

$$e_{int} = R_{N_2}(3T + \alpha\,\theta_d). \tag{2.59}$$

The ratio of specific heats γ for the mixture is given by

$$\gamma = \left(\frac{4+\alpha}{3}\right), \tag{2.60}$$

and the mixture enthalpy is given by

$$h = R_{N_2}[\alpha\,\theta_d + (4+\alpha)T\,]. \tag{2.61}$$

2.4.2 Frozen Flow

A distinction should be made between frozen flow and flow with no dissociation. A freestream flow with non-zero dissociation can be run in frozen mode. This means that chemical reactions are turned off, and the degree of dissociation in every cell will be constant. This is not equivalent to running the simulation with zero dissociation, because the degree of dissociation affects the gas dynamics through the ratio of specific heats γ and the effective gas constant $R(1+\alpha)$.

2.4.3 Non-equilibrium Flow

The Lagrangian reaction rate for α is given by

$$D\alpha/Dt = \partial\alpha/\partial t + \mathbf{u}\cdot\nabla\alpha. \tag{2.62}$$

The first term (the reaction rate) is decoupled from the second (the convection term). The convection term is computed by calculating the mass flux of each species separately. The chemical reactions are frozen as the cells exchange mass, momentum, and energy appropriately based on the mixture in each cell. The Lagrangian reaction rate is computed as shown below, allowing the evaluation of $\partial\alpha/\partial t$. Finally, the species composition of each cell is updated by computing an adiabatic reaction for the timestep Δt.

The rate equation for the IDG model is

$$\frac{D\alpha}{Dt} = \rho\, C(\alpha,T)\left[(1-\alpha)\exp\left(-\frac{\theta_d}{T}\right) - \frac{\rho}{\rho_d}\alpha^2\right] \tag{2.63}$$

Reference	C_1	η_1	C_1	η_2
Hanson & Baganoff [44]	2.2×10^{23}	-2.5	3.9×10^{30}	-4.5
Kewley & Hornung [45]	8.5×10^{22}	-2.5	2.3×10^{26}	-3.5

Table 2.2 Reported reaction rates for nitrogen (mks units)

where ρ_d is another gas constant, the characteristic density, and

$$C(\alpha, T) = [2\alpha C_1 T^{\eta_1} + (1-\alpha) C_2 T^{\eta_2}]/W, \tag{2.64}$$

with W being the molecular weight of the diatomic species. The characteristic density is an approximation to a collection of terms in the partition functions for N and N_2 which is not strongly dependent on temperature and is taken by Lighthill to be constant. This assumption is equivalent to representing the sum of electronic excitation for N and vibrational excitation for N_2 as a single degree of freedom for N_2 which is fully excited at all temperatures. For nitrogen, $\rho_d = 130000$ kg/m^3 and $\theta_d = 113200$ K.

The rate constants are matched so that

$$k_1 = 2\alpha C_1 T^{\eta_1} \exp(-\theta_d/T) \tag{2.65}$$

$$\text{and} \quad k_2 = (1-\alpha) C_2 T^{\eta_2} \exp(-\theta_d/T). \tag{2.66}$$

Several reaction rates are quoted in the literature. For nitrogen, Table 2.2 shows two sets of constants. It should be noted that these rates are given in mks units (meters, kilograms, seconds); often these rates are given in cgs units (centimeters, grams, seconds). Non-equilibrium simulations were performed for both sets, and the results were not very sensitive to the choice of reaction rate (among these two data sets). Simple Euler integration is used to advance the reaction for non-equilibrium flow. The reaction rate equation (2.63) is used to compute $D\alpha/Dt$, which is multiplied by the timestep Δt.

2.4.4 Equilibrium Flow

For equilibrium flow, local equilibrium is enforced in each cell at the end of each timestep. An adiabatic reaction is assumed, conserving mass, energy and momentum. Since this is a finite-volume method, the volume of each cell is fixed throughout the reaction, and since mass is conserved, the density is therefore also fixed. So the equilibrium calculation consists of finding the corresponding equilibrium values of α and T.

The law of mass action gives the equilibrium degree of dissociation. It can be obtained by setting the expression in brackets to zero in the rate equation (2.63), which yields

$$\frac{\alpha^2}{1-\alpha} = \frac{\rho_d}{\rho} \exp\left(-\frac{\theta_d}{T}\right). \tag{2.67}$$

This can be used to determine the equilibrium dissociation for a given density and temperature.

2.4.5 Transport Properties

For reacting flow, species viscosity and conductivity rules are used, then mixing rules based on Chapman-Enskog theory are used to compute mixture properties. This is discussed in Appendix B.

2.5 Time Stepping

This section describes the methods of time stepping that have been used in this work. This includes the standard time stepping schemes of time marching and space marching, and also two newer methods developed for use specifically on conical flows, the stepback method and the partial grid technique.

2.5.1 Time Marching

The computations presented in this work are all steady-state computations, so the accuracy of the time integration is not an important issue. One can easily perform unsteady simulations with these same techniques, although a more sophisticated time integration scheme such as a second-order Runge-Kutta or a predictor-corrector method would be necessary for better accuracy in time (see Section 2.1.4). These simulations are integrated in time to a steady state via Euler integration, which yields first-order accuracy in time.

The size of the timestep taken is given by the CFL number, which is specified for each computation. The CFL number (or Courant number) is named after Courant, Friedrichs, and Lewy, who recognized that a necessary condition for stability is that the domain of dependence of the finite difference method must contain the domain of dependence of the

partial differential equation it models, at least in the limit of zero cell size. Generally,

$$\mathrm{CFL} = \left| \frac{\lambda \Delta t}{\Delta x} \right|, \tag{2.68}$$

for each eigenvalue λ of the flux Jacobian. For a stable timestep with an explicit scheme, a necessary (but not sufficient) stability condition is that $\mathrm{CFL}_{\max} \leq 1$. In other words, the largest stable timestep Δt is limited by the cell with the largest value of $\lambda/\Delta x$. Since the timestep scales linearly with the cell size, a finer grid can still be run at the same CFL number (which corresponds to a smaller timestep). However, for a viscous computation, the presence of diffusion imposes an additional stability criterion, which scales with the square of the cell size [46]. This means that an explicit viscous computations may have to be run at CFL numbers substantially lower than CFL=1.

Convergence statistics are computed for the percent change of each state variable in each cell. The maximum, average, and sum over all cells are recorded. If the change in the state U of cell i is given by ΔU_i, we can define ε to be

$$\varepsilon = \max_{grid} \left[\frac{\sum_{faces} \Delta U_i}{\max(|\Delta U_i|)} \right]. \tag{2.69}$$

For a perfectly converged steady-state solution, the numerator will be zero since there will be no net change in the state. Typically, a converged solution has grid-maximum residuals on the order of $\varepsilon \approx 1 \times 10^{-4}$.

For a time-marching computation, the values of ghost or dummy cells are either dictated by the the geometry (see Sections 2.1.6 and 2.2.2), or set to the freestream value.

2.5.2 Space Marching

Space marching can be used for hyperbolic flows, where the solution is not dependent on downstream conditions. The computational domain may be broken up into several downstream slices, and each slice is successively time-marched to a steady state. The last plane of each slice becomes the upstream boundary condition for the next slice, with the other dummy cells for that slice being dictated in the normal manner. Normally, a zero-gradient boundary condition is used on the downstream side of space marching slices. Since

this is not the correct boundary condition, the last few downstream planes of any slice are not to be trusted and should be discarded.

2.5.3 The Stepback Method

When simulating a cone flow, the region near the tip poses difficulties owing to the tip singularity. The cells near the tip must become extremely small to resolve the flow. Additionally, for the most general conical flows (i.e., inviscid frozen or inviscid equilibrium flow past a cone at incidence), the flow field is two-dimensional, but not axisymmetric. The two-dimensionality of the flow may be exploited by writing the Euler (or Navier-Stokes) equations in a conical coordinate system and neglecting the derivatives along rays. However, this still requires a fully three-dimensional domain resolving the tip.

The stepback method is a technique for efficiently computing conical flows with a much smaller domain, and has the added advantage that the flow near the tip need not be resolved. The stepback method may be applied to any gas dynamics equations with no modifications to them. In terms of executing a simulation, the stepback method is really only an unusual boundary condition applied to the upstream boundary of the domain.

The original version of the stepback method arose from space-marching simulations of the parabolized Navier-Stokes (PNS) equations [47], although there are some important differences in how it is implemented in this work. Originally, the method was considered to be a special case of a PNS space marching technique, but the stepback method may be applied more generally. With PNS, the streamwise viscous diffusion terms of the Navier-Stokes equations are neglected. Typically, PNS schemes involve several other assumptions. In the PNS scheme which led to the stepback method, the streamwise convective flux vector was modified to allow stable space marching, and the pressure gradient normal to the body was neglected. In another approach [48], a portion of the streamwise pressure gradient is neglected. In the original stepback scheme, the *entire* streamwise pressure gradient was neglected. None of the PNS assumptions, or the further assumptions made with the original stepback method are necessary, and none of them are used here.

Presently the stepback method is applied to a computational domain which is a spherical shell centered on the tip of the cone (see Figure 2.6). This shell is only two cells thick in the radial direction away from the cone apex; the radial thickness of these cells is greatly

exaggerated for clarity in the figure. In the original use of the stepback method [47], a planar grid normal to the cone axis was used. But a conical flowfield will have no streamwise gradients ($\partial/\partial r = 0$), and so a no-gradient outflow condition will be exact if the grid lies on a sphere. For a cone at a high angle of incidence, a planar grid will have significant errors on the leeward side of the cone away from the cone surface. Here the radial direction can be quite different than the axial direction, and if a no-gradient boundary conditions is applied, the errors can be significant.

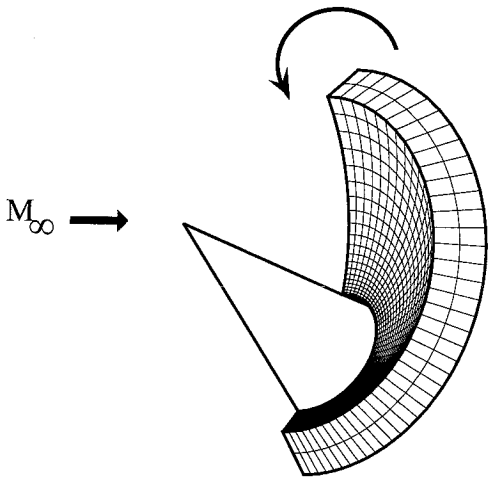

Figure 2.6 Schematic for the stepback method

The technique is implemented presently as follows: first the domain is initialized with the freestream conditions. This is followed by a flux calculation at all cell interfaces, and cell states are updated according to standard EFM or EFMO. At the end of each timestep, the cell states of the downstream side of the domain are projected along rays onto the upstream domain boundary and become upstream boundary conditions for the cells corresponding to the same ray from the tip. This process is repeated until the solution reaches steady state. In order to reach a steady state, the solution must become constant along rays, or conical. In some sense, the method allows the freestream to travel infinitely far down the length of the cone, until it reaches a self-similar solution. The basic assumption is an approximation in which radial derivatives are assumed negligible in comparison with lateral derivatives on the surface of the sphere. This is enforced indirectly through the stepback process rather than by modifying the actual equations.

For inviscid frozen and inviscid equilibrium hypersonic flow about conical bodies, the

stepback method is exact in the sense that these flows contain no length scales and are truly conical. However, the technique can also be used to compute approximate solutions to viscous cone flows, both frozen and equilibrium. There is no theoretical guarantee that this technique will converge for a viscous solution, but in practice it is extremely robust, and can sometimes even enhance stability in the sense that higher CFL numbers may be used for the same grid resolution.

It should be noted that the stepback method may *not* be used for chemically non-equilibrium flow. When run in non-equilibrium mode, the stepback method converges to the equilibrium solution, which is consistent with the idea that the method allows the flow to travel infinitely far down the cone.

2.5.4 The Partial Grid Scheme

The errors associated with using the stepback method for viscous flows suggested the "partial grid" method. Here a stepback solution is computed at some small radius from the tip $r = R_1$. A "partial grid" is then constructed for $R_1 < r < R_2$, and the stepback solution at $r = R_1$ is used as the upstream boundary condition (see Figure 2.7, where the grid shown has much fewer cells depicted for clarity). At $r = R_2$, a no-gradient outflow condition is used. The partial grid may then be time-marched to a steady state. The flow recovers from the errors associated with the stepback method a few cells downstream of the front of the partial grid, meaning that the boundary layer grows from the stepback solution and reaches an appropriate thickness. In this fashion, the errors from the stepback method are "washed out," but computation of the tip region is avoided. For clarity, several views of a typical partial grid are shown in Figure 2.8, with the stepback grid shown as well.

A partial grid may be run in frozen, non-equilibrium, or equilibrium modes. For a frozen calculation, the stepback solution used to initialize the partial grid should obviously be a frozen stepback solution, and an equilibrium partial grid should be initialized with an equilibrium stepback solution. In these cases, the partial grid solution only has to recover from the errors due to the stepback technique. However, to perform a non-equilibrium calculation, the partial grid must be initialized with a frozen stepback solution. Ideally, this stepback solution is at such a small distance from the tip that the frozen assumption is valid, and the partial grid will capture the whole chemically active region. If the stepback solution

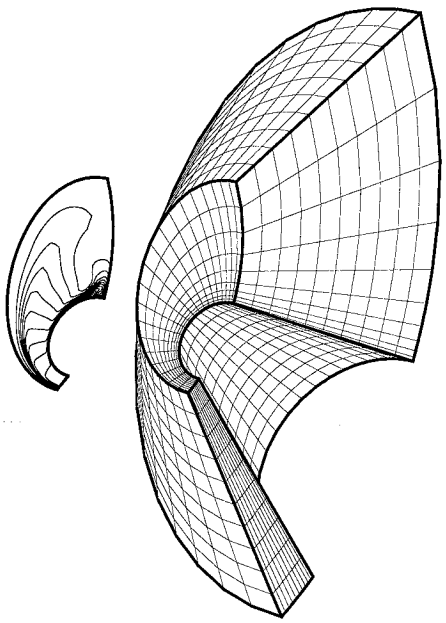

Figure 2.7 Stepback solution and partial grid

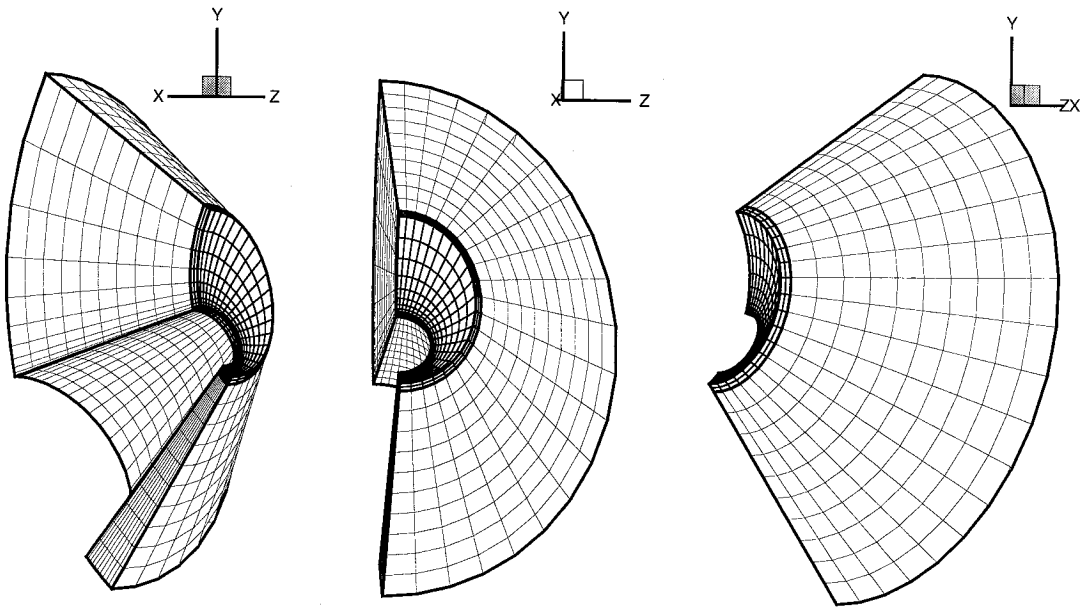

Figure 2.8 Different views of a typical partial grid

is at a larger radius, then the partial grid will have "missed" some of the chemistry, and must recover from these errors as well. Therefore a non-equilibrium partial grid generally takes longer to recover from the stepback solution than a frozen or equilibrium partial grid.

2.6 PGP3D

Option	PGP3D.2	PGP3D.4
Flux integrator	EFM Roe	EFM Roe EFMO van Leer & others
Chemistry	Frozen	Frozen Non-equilibrium Equilibrium
Time-integration	Time-marching Space-marching	Time-marching Space-marching Stepback
Formulation	Explicit	Explicit Implicit

Table 2.3 Developments to PGP3D

The code used for these simulations is PGP3D (Parallel General Purpose 3-Dimensional). The previous version of PGP3D (PGP3D.2) was written by Mallett [49], and does not contain many of the features used for these simulations. PGP3D has switches for many different options. One has the choice of several different patch integrators, including EFM, EFMO, Roe's method [50], and van Leer's method [35]. However, only EFM and EFMO have been used for these computations. The code may be run in time-marching, space-marching, or stepback modes. Both explicit and implicit versions of EFM and EFMO have been formulated. For frozen flow, there is a greater advantage in using the implicit formulation, which can allow CFL numbers as high as 10 or more. For reacting flows, the stability of the implicit version is not considerably better than the explicit one. The implicit formulation uses an approximate factorization for the inversion of the Jacobian matrix, and is due to Moschetta [51]. Several flux-limiters and slope-limiters are available for achieving

higher-order accuracy (e.g., van Leer's flux-limiter [35], Roe's "superbee" limiter [36], and van Leer's minmod technique [38]), although the minmod technique has proven very reliable and has been used for all computations here. The code accommodates frozen flow for nitrogen, oxygen, and air; it accommodates nitrogen and oxygen for dissociating flows. For dissociating flows, PGP3D may be run in frozen, non-equilibrium, and equilibrium modes. The improvements made between PGP3D.2 and PGP3D.4 are summarized in Table 2.3.

Chapter 3

Frozen Flow Past a Cone at Zero Incidence

This chapter describes the computations performed on a simple test case, the boundary layer on a cone at zero incidence in a viscous frozen flow. Comparisons were made between an approximate analytical solution and simulations performed with a time marching method, the stepback method, and the partial grid method. The errors associated with the stepback method were quantified, and the partial grid scheme is shown to be an effective way of getting very good approximate results with much less computation than required for a full time marching scheme.

3.1 Test of the Stepback Method

The test case used was viscous frozen flow past a cone at zero incidence, because an approximate analytical solution exists for the boundary layer. The inviscid flow past the cone was computed with the stepback method, and these conditions were then used as the edge conditions for an analytical boundary layer solution.

First, the flat plate boundary layer equations were solved using the Dorodnitsyn-Howarth transformation [52]. The Mangler transformation [52] was used to find the corresponding cone boundary layer. Initial guesses were made for the derivative of velocity at the wall, and for either the wall temperature for an adiabatic wall or the wall temperature gradient for an isothermal wall. Then a shooting method was used, where the equations were integrated to the edge of the boundary layer and the initial guesses were modified if the edge conditions were not met.

Several computations were performed to assess the errors associated with the stepback and partial grid methods. The first computation was made using only the stepback method. For the second computation, a grid was used which extended from very near the tip of the cone to a radius (or distance down the cone) larger than the radius of interest. This will be referred to as the full grid solution.

It was observed that the pure stepback consistently underestimated the size of the boundary layer, while capturing its profile and wall values well. This led to the idea for the new method proposed here. Whereas the stepback method has certain problems, it was hoped that these errors would "wash out" when combined with conventional time marching techniques. So for the third computation, a stepback computation was preformed at a lower radius, and this solution was used as an upstream boundary condition for a grid which extended from the lower radius to the radius of interest. This type of solution will be referred to as the partial grid solution.

This partial grid solution is obtained in much less time than the full grid solution for two reasons. First, since the smallest cells in the partial grid are much larger than the very small cells at the tip of the full grid, the viscous runs can be made at substantially larger CFL numbers. For viscous computations, the time scale is proportional to the square of the cell size. A full grid solution may have to be run at CFL numbers as low as 0.05, while the corresponding partial grid can be run at CFL=0.25. Combined with the difference in smallest cell size, a partial grid timestep can be as much as a hundred times the corresponding full grid timestep. Since the partial grid also has less cells in the downstream direction, the solution may be obtained in much less time than the full grid.

3.2 Analytical Solution

An approximate analytical solution was calculated for the frozen compressible conical boundary layer. The compressible flat plate boundary layer equations were solved using the Dorodnitsyn-Howarth transformation, and this solution was transformed into a conical boundary layer profile with the Mangler transformation [52]. These transformations are discussed in Appendix C. This solution assumes zero pressure gradient at the edge of the boundary layer, but since the cone will actually have a positive pressure gradient, the analytical solution will slightly overestimate the thickness of the boundary layer.

Gas	Air
Cone half-angle	10°
Incidence	0°
Length (m)	0.117
M	7.95
ρ (kg/m^3)	0.012
u (m/s)	1186
T (K)	55.4
p (kPa)	0.191
H_0 (MJ/kg)	0.759
Re_L	480000
Pr	1.0

Table 3.1 Test conditions for the zero incidence Tracy test. H_0 is the stagnation enthalpy. Re_L is the Reynolds number based on the freestream conditions and the body length.

3.3 Test Conditions

The zero incidence tests were done at the conditions which Tracy used, which are summarized in Table 3.1. It should be noted that the Tracy tests used a different Pr and wall boundary condition.

The governing parameter for viscous effects is the Reynolds number (Re), which is defined as

$$Re = \frac{\rho U L}{\mu}, \tag{3.1}$$

where ρ, U, and μ are the conditions at the state which the Reynolds number is based on, e.g. the freestream conditions or post-shock conditions. L is a geometrical scale, usually either the body length or x. Here, the Reynolds number will always be based on the freestream conditions, and the subscript will denote whether the Reynolds number is based on body length or distance (i.e., Re_L or Re_x). For the Tracy test conditions, $Re_L = 480000$.

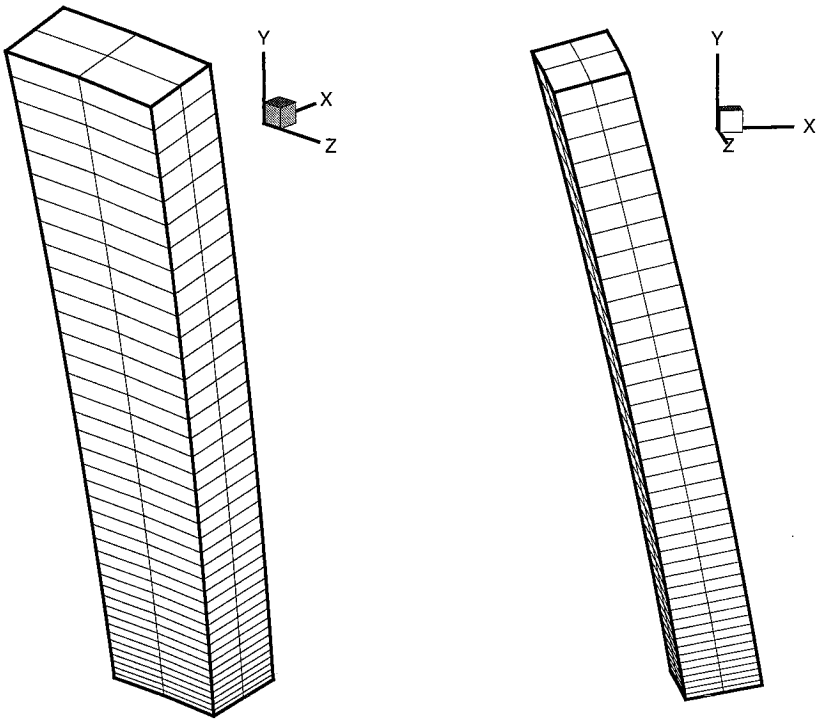

Figure 3.1 Typical stepback mesh for a cone at zero incidence $(2 \times 40 \times 2)$. The freestream is moving in the positive x-direction, and the cone sits below the mesh.

3.4 Computational Grids

As discussed previously, the stepback grid uses only two cells in the axial direction. For these zero incidence cases, axial symmetry was invoked, so only two cells were used in the azimuthal direction. Forty cells were used in the direction normal to the cone surface, stretched tighter towards the cone surface. We will use the convention $(i_{max} \times j_{max} \times k_{max})$ to denote the resolution of grids, where the **i**-direction is down the length of the cone, the **j**-direction is away from the surface of the cone, and the **k**-direction is the azimuthal direction around the cone. Therefore the zero incidence stepback meshes had a resolution of $(2 \times 40 \times 2)$. Figure 3.1 shows a typical zero incidence stepback grid, with the freestream moving in the positive x-direction, and the cone sits below the mesh.

The included angle of the whole mesh varies with the distance from the tip, since near the tip of the cone, the boundary layer is relatively thicker. Similarly, for equilibrium flow, both the boundary layer and the shock layer will be relatively thinner. Various angles and stretchings were tried to find grids which were most appropriate for each particular case.

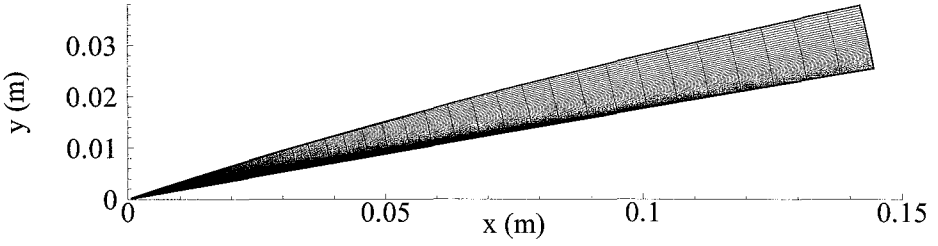

Figure 3.2 Typical full grid domain for a cone at zero incidence ($40 \times 40 \times 2$)

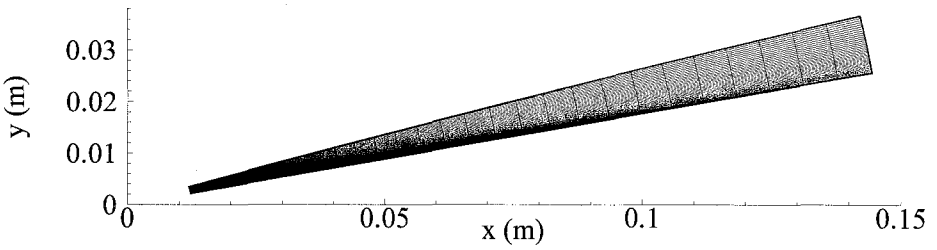

Figure 3.3 Typical partial grid domain for a cone at zero incidence ($33 \times 40 \times 2$)

For the same reason, some of the full and partial grid domains have a slight degree of concavity, since the front end of the grid needs a larger included angle than the rear end. A strictly conical grid could have been used, but this would waste a significant number of cells near the back of the mesh.

For the full grid computations, the meshes used had forty cells in the axial direction, with two cells in the azimuthal direction and forty cells normal to the cone ($40 \times 40 \times 2$). These calculations can take as long as several weeks on a Pentium Pro processor, due to the range of scales and the limit on the CFL number imposed by the size of the smallest cells. Typically, the whole grid runs were made with CFL numbers around 0.05. Figure 3.2 shows a typical full grid mesh.

The partial grids were selected to be truncations of the full grids. By this we mean that all cells ahead of the radius of the initial stepback radius are dropped, and cells behind that radius are the same size as the corresponding cells in the full grid. The number of cells in the axial direction is smaller with the partial grid, but cell dimensions are the same in other directions. For the results shown in this work, the initial stepback radius was taken to be

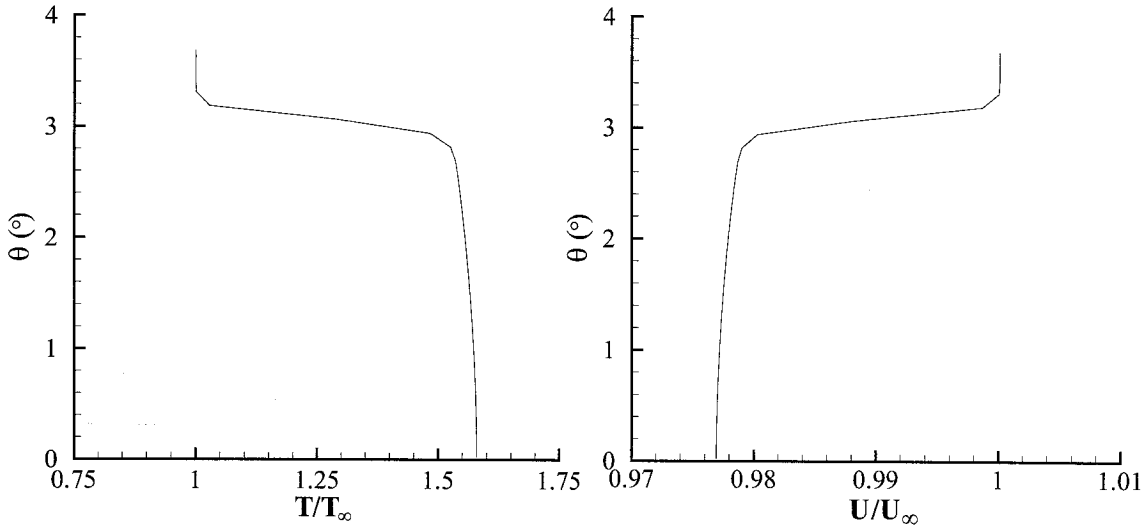

Figure 3.4 Inviscid shock layer profiles for a 10° cone at zero incidence. Tracy conditions, M=7.95. Stepback, EFMO. θ is the angle from the cone surface, T_∞ is the freestream temperature, U_∞ is the freestream velocity.

1/9 the radius of interest. With the stretchings used, this was equivalent to truncating the first seven cells of the full grid, so the partial grid resolution was (33 × 40 × 2). Figure 3.3 shows a typical partial grid domain. CFL numbers are similar to the CFL numbers from the stepback grid, as high as 10 or more, and computational times are on the order of several days on a Pentium Pro processor.

3.5 Results

The first computation performed was the inviscid stepback calculation, which provides the edge conditions for the analytical solution. The temperature and velocity profiles are shown in Figure 3.4. These edge results agree well with the values at the edge of the boundary layer from the viscous stepback results, which will be discussed below.

Figure 3.5 shows a comparison of profiles for the analytic and stepback solutions for both EFM and EFMO. These profiles are taken at a constant radius, meaning that they are extracted from a spherical surface centered on the cone tip. For completeness, the first two plots of Figure 3.5 include the shock layer, although for the purposes of this test, we are really interested in the boundary layer thickness. The third and fourth plots of Figure 3.5 show the same profiles, concentrating only on the boundary layer. The remainder of the

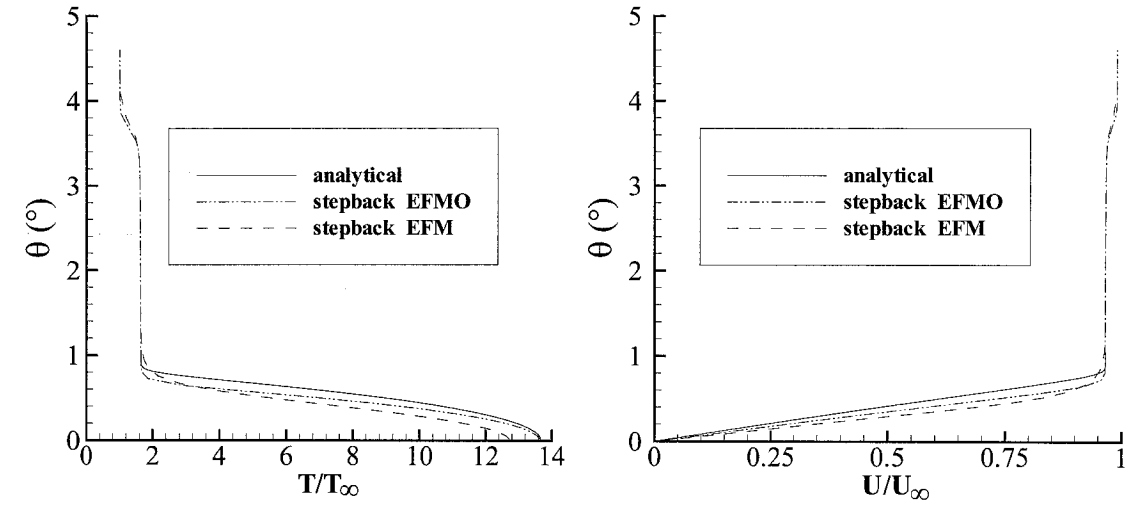

Shock layer and boundary layer

Shock layer and boundary layer

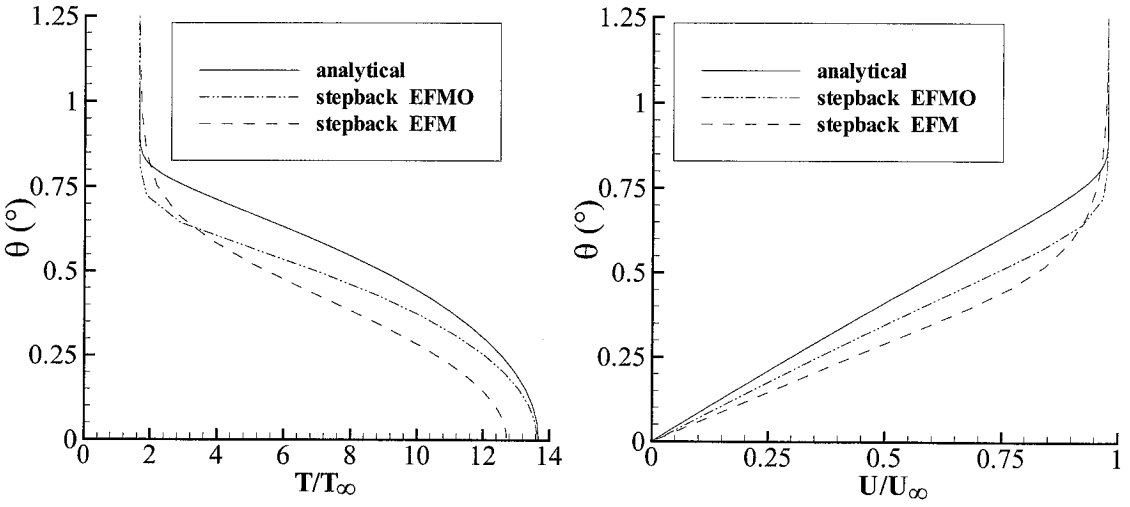

Boundary layer

Boundary layer

Figure 3.5 Shock layer and boundary layer profiles for a 10° cone at zero incidence. Tracy conditions. Adiabatic wall, $M = 7.95$, $Pr = 1$, $Re_x = 4.2 \times 10^5$. θ is the angle from the cone surface, T_∞ is the freestream temperature, U_∞ is the freestream velocity.

boundary layer profiles will be presented in this fashion. It can be seen that EFMO captures the shape of the profile well, whereas EFM's diffusivity results in a thicker boundary layer, and a lower adiabatic wall temperature. It should be noted that a higher resolution EFM solution would agree well with the EFMO solution (see Section 3.5.2).

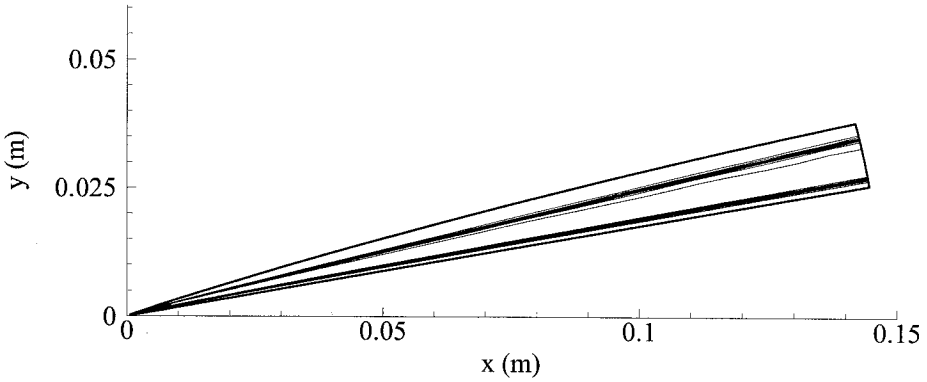

Figure 3.6 Density contours for full grid computation showing shock wave and boundary layer thickness. 10° cone at zero incidence. Tracy conditions, EFMO. Adiabatic wall, M = 7.95, Pr = 1. At end of grid, r=0.15, and $Re_x = 6.15 \times 10^5$.

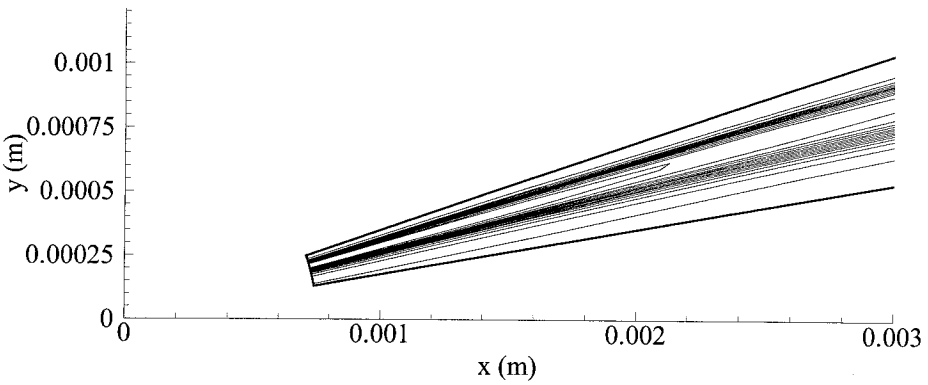

Figure 3.7 Density contours at tip of full grid computation. 10° cone at zero incidence. Tracy conditions, EFMO. Adiabatic wall, M = 7.95, Pr = 1. At r=0.15, $Re_x = 6.15 \times 10^5$.

The first viscous calculation, using only the stepback method, showed that while the stepback method with the EFMO method accurately reproduces the shape of the boundary layer profile and gives accurate adiabatic wall temperatures, the thickness of the boundary layer is consistently underestimated. It should be remembered that the stepback method is not exact for viscous flow, so some error is to be expected.

If the boundary layer were conical, it would have the same relative thickness (i.e., when scaled by the distance from the tip) at any location on the cone. A real boundary layer will grow as it travels down the cone, but will become relatively thinner because the growth goes like $\sqrt{r}$. Consider a hypothetical stepback calculation carried out on a thick shell with many cells in the radial direction. The boundary layer would be considerably thinner at the downstream side, and when the downstream solution is stepped back to the upstream side, the boundary layer would be too thin, although the shape of the profile would be correct. Perhaps this is occurring on a smaller scale with a real stepback calculation. Although the difference between the upstream and downstream solutions is very small, perhaps the repeated application of the stepback algorithm compounds these errors, leading to the results that are seen here.

Stepback solutions of this resolution can take about a day on a Pentium Pro processor when started from the freestream. However, for a given freestream, a stepback solution from another Reynolds number may be used as an initial condition for the Reynolds number of interest. The boundary layer and shock wave must adjust to their new positions, and the included angle of the mesh may need to be adjusted, but these computation take only a few hours when initialized from a previous stepback solution. They can be run in implicit mode at large CFL numbers of 10 or more.

The second computation (full grid) agreed very well with the analytical solution, except near the tip. This is not surprising since EFMO has already been shown to accurately reproduce viscous effects [2]. The tip was a region of concern, since the singularity at the tip of the cone has produced problems with previous simulations. Figure 3.6 shows the contours from a full grid computation, where Figure 3.7 shows the very tip of the same grid. The grid must be composed of quadrilaterals, so every cell must have a finite thickness at the upstream edge of the grid. With a grid lying on rays from the tip, it was impossible to have the first cell go right down to $r=0$, so the first cell starts at a small finite value ($r=1\times10^{-9}$ m) and is relatively long ($\Delta r \approx 5\times10^{-4}$ m). Whereas the shock should be attached to the cone at the start of the grid, it sits off of the cone, intersecting the upstream boundary. However, further downstream the results agree very well with the analytical solution. This can be seen in Figure 3.8, which shows temperature and velocity profiles at $Re_x=4.2\times10^{-5}$ for the analytical solution and for all three computational methods (stepback, full grid, and partial grid) performed with EFMO. The full grid gives a boundary layer thickness slightly

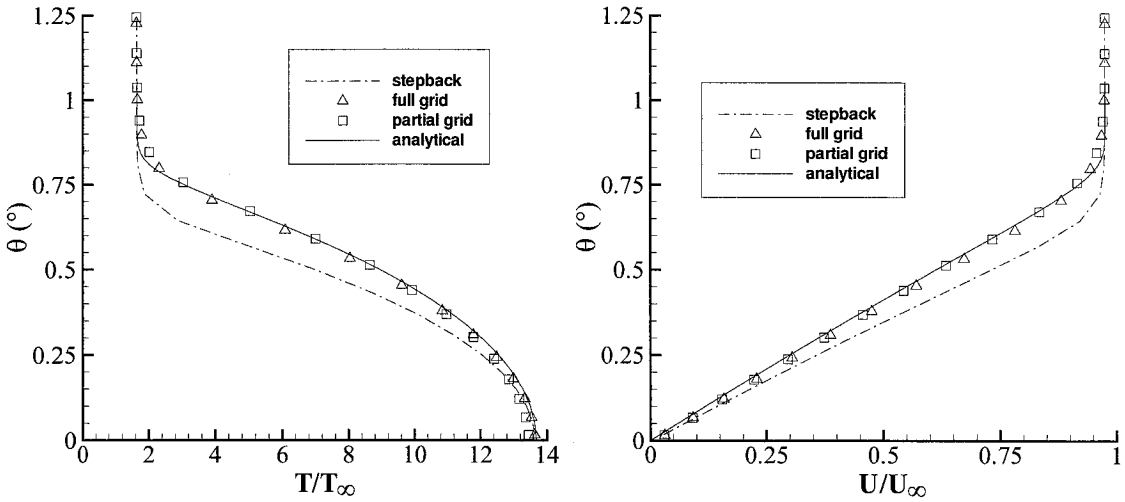

Figure 3.8 Temperature and velocity profiles without shock layer for a 10° cone at zero incidence. Tracy conditions, EFMO. Adiabatic wall, $M = 7.95$, $Pr = 1$, $Re_x = 4.2 \times 10^5$. θ is the angle from the cone surface, T_∞ is the freestream temperature. U_∞ is the freestream velocity.

less than that predicted by the analytical solution (which will overpredict the thickness, as explained earlier), and agrees very well with the predicted adiabatic wall temperature.

The third computation shows that a calculation which uses a stepback solution as a boundary condition needs only a few downstream cells to wash out the errors introduced by the use of the stepback method. In Figure 3.8, the partial grid boundary layer is nearly indistinguishable from the full grid boundary layer, except for the small error in the adiabatic wall temperature. Figure 3.9 shows how the boundary layer thickness adjusts downstream of the stepback solution. This figure compares the profiles from the first four downstream cells of the partial grid with the respective profiles from the full grid. In the first cell, the partial grid solution still underestimates the boundary layer thickness by about 20%. As the flow moves down the cone, the boundary layer thickness decreases, as seen in the full grid profiles. The partial grid profiles do not decrease in thickness as quickly, and by the fourth cell, the predicted boundary layer thicknesses are almost identical. There is a slight error in the adiabatic wall temperature. At low Reynolds numbers, such as these cells near the tip, the partial grid slightly overpredicts the adiabatic wall temperature, but at higher Reynolds numbers (such as those in Figure 3.8), the method slightly underpredicts it.

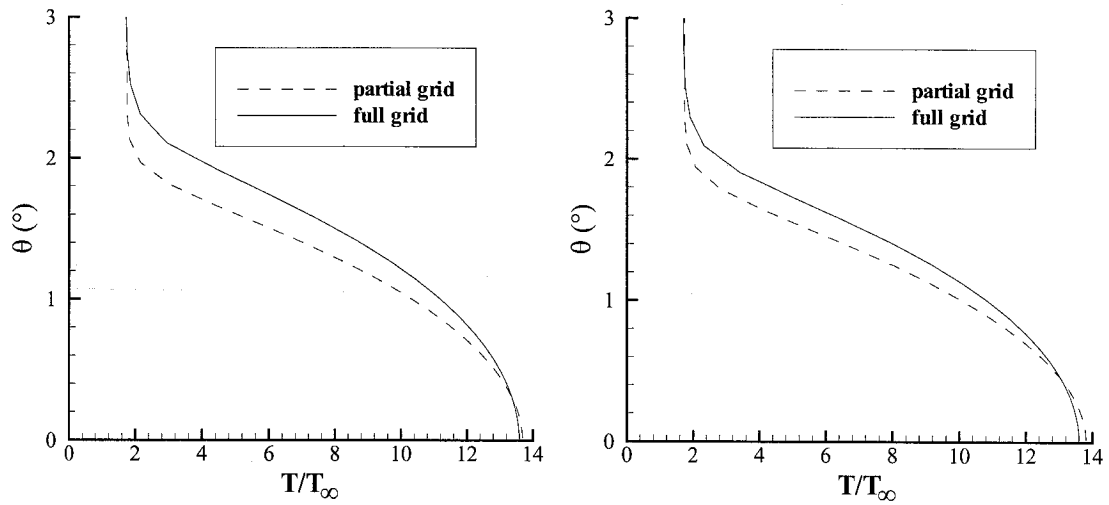

(a) First cell, $Re_x = 55000$ (b) Second cell, $Re_x = 62800$

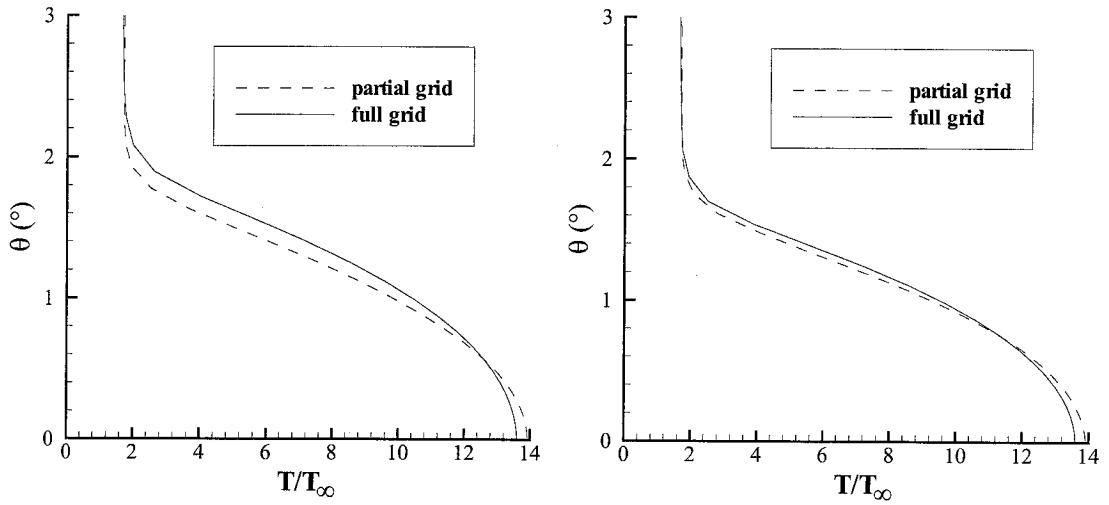

(a) Third cell, $Re_x = 71000$ (b) Fourth cell, $Re_x = 80400$

Figure 3.9 Boundary layer adjustment from a stepback solution. 10° cone at zero incidence. Tracy conditions, EFMO. Adiabatic wall, M = 7.95, Pr = 1. θ is the angle from the cone surface, T_∞ is the freestream temperature. The caption indicates the corresponding streamwise cell number from the partial grid.

3.5.1 Recovery of Partial Grid Solution

The partial grid method recovers from initial errors in the boundary layer. The Blasius boundary layer solution will also recover from an initial error in the following sense: if there is an error in the downstream coordinate, the boundary layer thickness will also be incorrect. However, if the incorrect coordinate system is used at larger distances down the body, the relative error will be less for both the coordinate and the boundary layer thickness.

The non-dimensionalized Blasius boundary layer displacement thickness δ is proportional to the inverse square root of the distance x down the body, or

$$\frac{\delta}{x} \propto \frac{1}{\sqrt{x}}. \tag{3.2}$$

If the origin is shifted by Δx, so that the distance is now $x' = x + \Delta x$, the solution will predict a displacement thickness

$$\frac{\delta'}{x'} \propto \frac{1}{\sqrt{x'}}. \tag{3.3}$$

Formally, the recovery of the solution means than

$$\lim_{x \to \infty} \left(\frac{\delta}{\delta'} \right) = \frac{\sqrt{x}}{\sqrt{x'}} = 1. \tag{3.4}$$

In a similar manner, the analytical solutions discussed in Section 3.2 can be computed with shifted coordinates, and the recovery of these solutions may be compared to the partial grid results.

The thickness of the stepback solution used at the front of the partial grid was used to calculate the shift in coordinates necessary to produce an analytical solution with the same thickness. Analytical solutions were then computed using the shifted coordinates at the radii corresponding to the first four cells of the partial grid. The results are shown in Figure 3.10, which shows velocity profiles. The partial grid results recover more quickly than the shifted analytical solutions, although the difference is not large in the first three cells. By the fourth cell, the partial grid profile is quite similar to the analytical solution, predicting the same thickness with slight differences in the outer part of the boundary layer; the shifted analytical solution underpredicts the boundary layer thickness by about 10%.

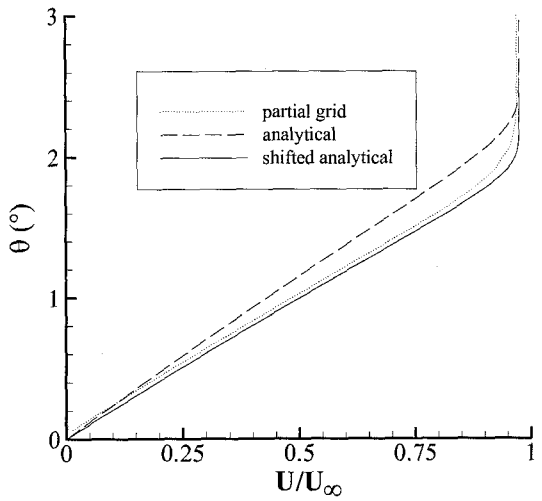

(a) First cell, $Re_x = 55000$

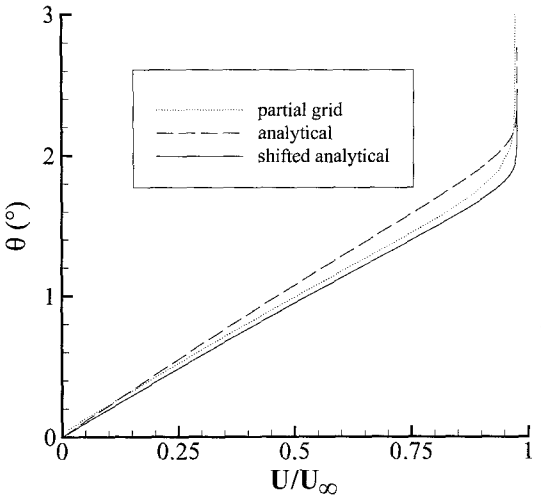

(b) Second cell, $Re_x = 62800$

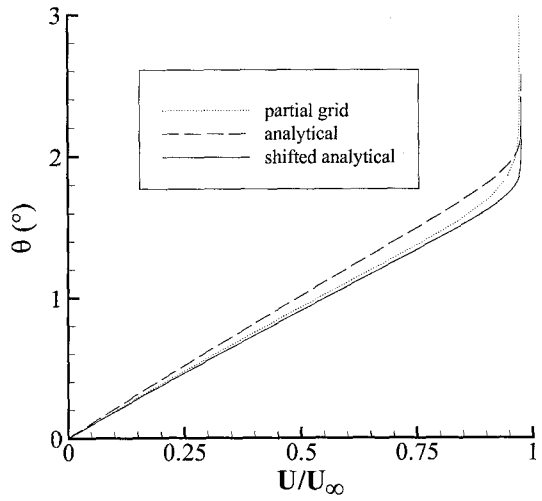

(a) Third cell, $Re_x = 71000$

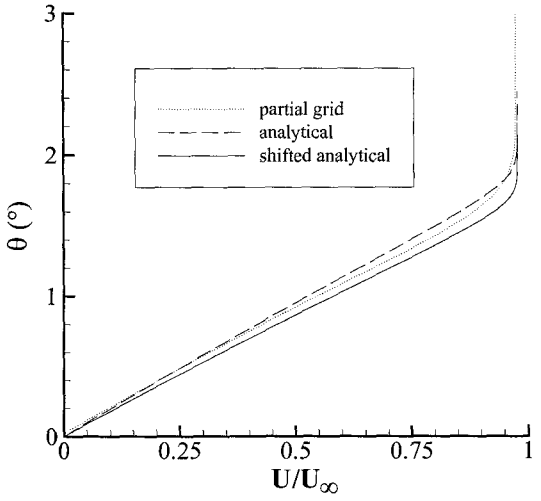

(b) Fourth cell, $Re_x = 80400$

Figure 3.10 Comparison of the partial grid boundary layer adjustment from a stepback solution with a shifted analytical solution (an analytical solution with an error in the downstream coordinate which would predict the same displacement thickness as the stepback solution). 10° cone at zero incidence. Tracy conditions, EFMO. Adiabatic wall, M = 7.95, Pr = 1. θ is the angle from the cone surface, U_∞ is the freestream velocity. The caption indicates the corresponding streamwise cell number from the partial grid.

3.5.2 Grid Convergence Study

The following section shows some of the practical differences between EFM and EFMO. A grid convergence study was performed for the stepback boundary layer solution for both methods. A series of grid resolutions were used to solve the boundary layer, doubling the grid resolution each time.

Figure 3.11 shows stepback temperature and velocity profiles for the boundary layer at $Re_x = 4.2 \times 10^{-5}$ on a 10° cone at zero incidence. EFM solutions were performed with 40, 80, 160, 320, and 640 cells. EFMO solutions were computed with 40, 80, 160, and 320 cells. EFMO was too unstable to provide a solution with 640 cells.

The EFM results overestimated the boundary layer thickness and underestimated the wall temperature, but the solutions converge monotonically to a limit solution. The EFMO solutions predict the thickness well at all resolutions, although there are some errors at the outer edge of the boundary layer. The wall temperature does converge for EFMO, but not monotonically. With 40 cells, the temperature is underpredicted, but with 160 cells, it is overpredicted. However, EFMO converges more quickly than EFM. In terms of wall temperature, an EFMO solution of a given resolution is about as accurate as an EFM solution of twice that resolution.

The errors at the outer edge of the EFMO boundary layer are due to a slight oscillation in the pressure at the edge of the boundary layer. Both EFM and EFMO suffer from this oscillation, which disappears at higher resolutions. EFMO is more sensitive to this oscillation, and it affects the EFMO temperature and velocity profiles; the EFM profiles are relatively unaffected by the pressure oscillation.

At high resolutions, the EFM and EFMO profiles are very similar. Figure 3.12 shows a comparison of the highest resolutions tested for each method: 640 cells for EFM, and 320 cells for EFMO. These profiles agree extremely well, and show that EFM and EFMO converge to the same solution.

These results show that at lower resolutions, the dissipation of EFM is too high to achieve an accurate solution. This is not true at high resolutions. However, at very high resolutions, EFMO is too unstable to converge to a solution. If computational resources allow for high resolution, EFM can be used to obtain accurate solutions. Otherwise, EFMO should be used to achieve high accuracy with fewer cells.

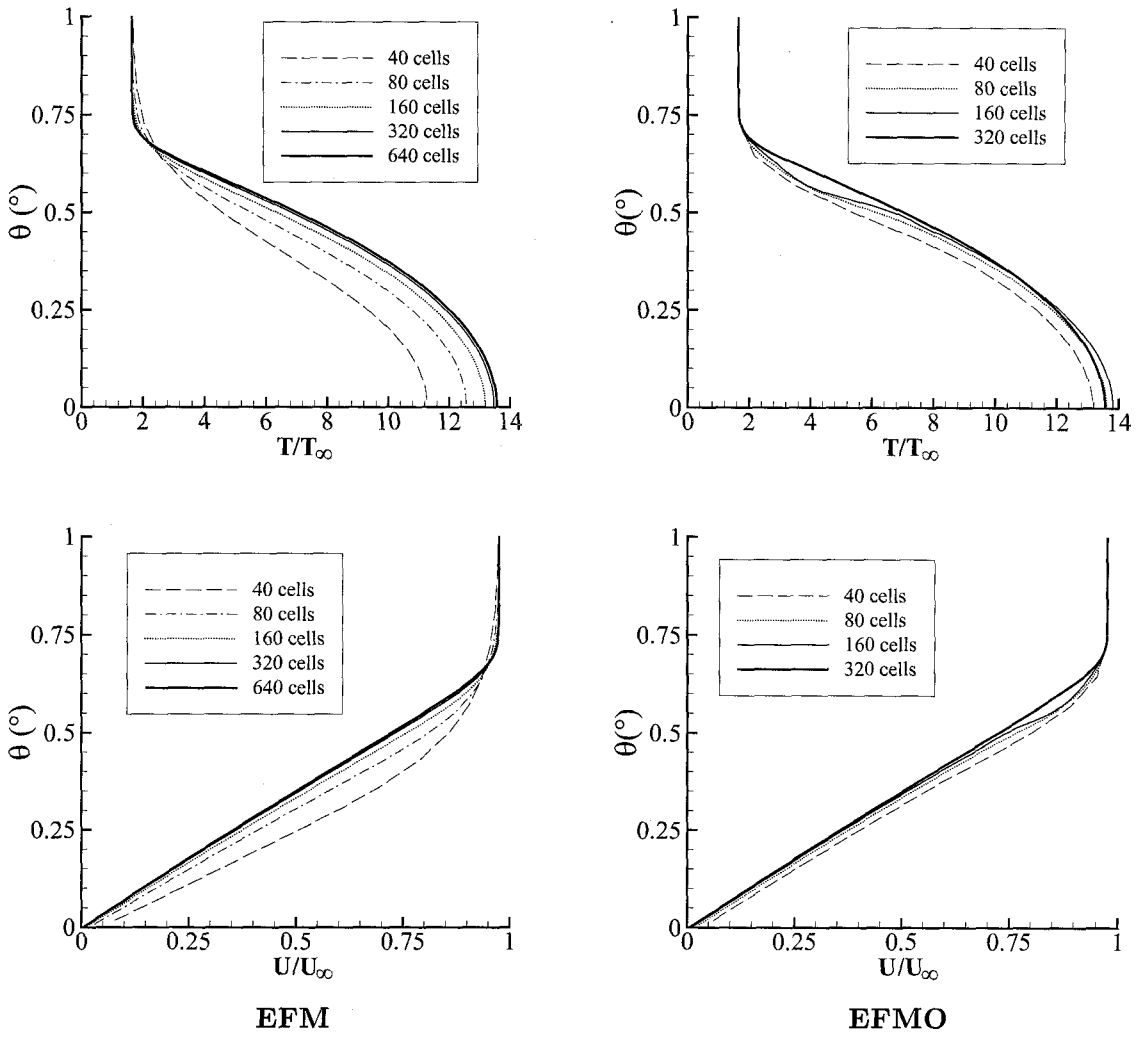

Figure 3.11 Grid convergence for the stepback boundary layer, 10° cone at zero incidence. Tracy conditions. Adiabatic wall, $M = 7.95$, $Pr = 1$, $Re_x = 4.2 \times 10^5$. θ is the angle from the cone surface, T_∞ is the freestream temperature. U_∞ is the freestream velocity.

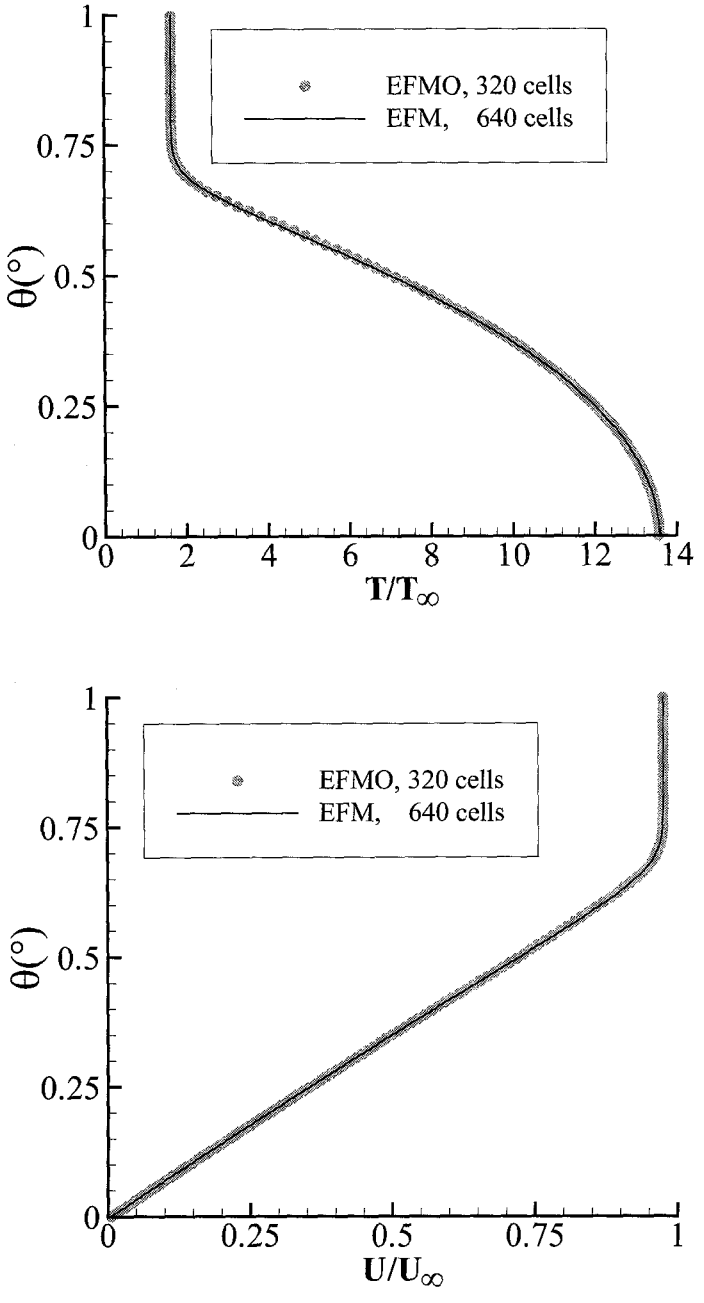

Figure 3.12 Comparison of high resolution EFM and EFMO boundary layer profiles, 10° cone at zero incidence. Tracy conditions. Adiabatic wall, M = 7.95, Pr = 1, $Re_x = 4.2 \times 10^5$. θ is the angle from the cone surface, T_∞ is the freestream temperature. U_∞ is the freestream velocity.

Chapter 4

Frozen Flow Past a Cone at Incidence

This chapter describes the computations performed to test the stepback method when applied to cones at incidence. High-resolution stepback computations are compared against experimental measurements of flow features and surface conditions.

4.1 Test Conditions and Experimental Details

In order to examine the effectiveness of the stepback method for frozen viscous flow, comparisons were made against the results of Tracy [5]. In the Tracy experiment, a hypersonic isothermal cone was tested in air in the GALCIT hypersonic facility at Caltech. Measurements were taken at various incidence angles; only the highest incidence produced the full shock-vortex system that we are interested in, so comparisons were made only for that incidence angle. These numbers are summarized in Table 4.1.

The calculations at incidence were done using the same freestream conditions as the zero incidence calculations (see Section 3.3), however the surface boundary condition was different. Recall that the zero incidence computations were performed with an adiabatic boundary condition at the wall, but in Tracy's experiment, the cone surface was isothermal at a temperature of 317 K. The temperature of the model was maintained with cooling water which was continuously pumped through the cone. For the computations, the Prandtl number was assumed to be constant, and for the relatively cold test conditions, it was assumed to have the value Pr=0.72.

Tracy's results include surface pressure and heat transfer measurements around the circumference of the cone, as well as flow field surveys. For the flow field surveys, a pitot probe was traversed through the flow field in circular paths at various radii from the cone, and the changes in pitot pressure were used to determine the location of flow features such as shock waves and viscous shear regions. The surface measurements were taken at a Reynolds number (based on freestream conditions and distance from the tip) Re_x=3.6×10^5, and the

Gas	Air
Cone half-angle	10°
Incidence	24°
Length (m)	0.117
M	7.95
ρ (kg/m^3)	0.012
u (m/s)	1186
T (K)	55.4
p (kPa)	0.191
H_0 (MJ/kg)	0.759
Re_L	480000
Pr	0.72

Table 4.1 Test conditions from Tracy. H_0 is the stagnation enthalpy. Re_L is the Reynolds number based on the freestream conditions and the body length.

flow features are presented for $Re_x = 4.2 \times 10^5$. For the entire cone, the flow was laminar.

Figure 4.1 shows several numerical pitot pressure traces, taken from the simulations discussed in this chapter at various values of θ, the angle from the surface of the cone. These traces are taken from the $Re_x = 4.2 \times 10^5$ simulation discussed in Section 4.3.3, but are shown here to facilitate discussion of the pitot traces. These traces show the characteristic behavior that corresponds to the domains of the flow field, and show that pitot pressure traces are sufficient to define these domains.

The numerical pitot pressure can be computed from the static pressure p, the Mach number M, and the ratio of specific heats γ [53]. Different expressions must be used for subsonic and supersonic flow, to account for the shock wave upstream of the numerical pitot tube, yielding

$$\frac{p_p}{p} = \begin{cases} \left(1 + \dfrac{\gamma - 1}{2} M^2\right)^{1/(\gamma-1)}, & M < 1 \\ \left[\dfrac{(\gamma+1)^2 M^2}{4\gamma M^2 - 2(\gamma - 1)}\right]^{\gamma/(\gamma-1)} \left(\dfrac{1 - \gamma + 2\gamma M^2}{\gamma + 1}\right), & M \geq 1 \end{cases} . \tag{4.1}$$

At small values (θ=1.64°), a traverse around the cone will not cross the bow shock, but the expansion is clearly seen. The outer edge of the viscous region is seen as a drop in pitot

pressure at $\phi \approx 130°$. At small θ, this is not extreme, but at larger θ, the drop in pitot pressure is fairly rapid. The pitot pressure reaches a minimum at the inner edge of the separated shear layer, and rises again in the vortex system.

At larger values of θ (θ=3.16°, 5.02°, 8.33°), the pitot pressure rises behind the bow shock, then drops as the flow expands around the cone. The pressure rises again at the leeward shock (twice if both branches of the λ-shock are intersected by θ). This is followed by the rapid drop in pitot pressure at the outer edge of the shear layer, and the minimum at the inner edge of the shear layer. This is followed by a slight rise in the vortex towards the leeward plane of symmetry, except in the case of $\theta = 8.33°$. This pitot trace does not intersect the vortex. Rather, it crosses the separated shear layer at the leeward plane of symmetry where it is meeting its counterpart from the opposite side of the cone, and so the minimum value lies at the plane of symmetry.

4.2 Computational Grids and Simulation Details

Initially, calculations were carried out on the Intel iPSC Touchstone Delta. The Delta is a 512-node parallel machine based on i860 processors. When it was commissioned in 1991, this machine was the world's fastest supercomputer [54]. Parallel instructions can be either machine-specific calls, or the Express environment [55] may be invoked. With Express, the code is portable to any parallel machine supporting Express and the Fortran 77 language, or to any sequential machine supporting Fortran 77, regardless of Express. However, there proved to be some problems with obtaining good high-resolution solutions on the Delta. This will be discussed below, in Appendix D. More recently, new sequential machines became available which allowed for similarly high-resolution computations, and the Tracy case was recomputed, with the results agreeing well with the previous ones.

Only pure stepback runs were made for these comparisons. The resolution of the Tracy runs was $(2 \times 150 \times 200)$, or 150 cells normal to the cone and 200 in the azimuthal direction. It was not possible to obtain such high crossflow resolution with either full or partial grid runs. A typical grid (of lower resolution) for a cone at incidence is shown in Figure 4.2. The first view is from the tip of the cone, looking down the axis of the cone. This is the viewpoint from which contours and flow features will be presented. As discussed in Section 2.5.3, the stepback grids lies on a spherical surface centered on the cone tip. All data here are taken

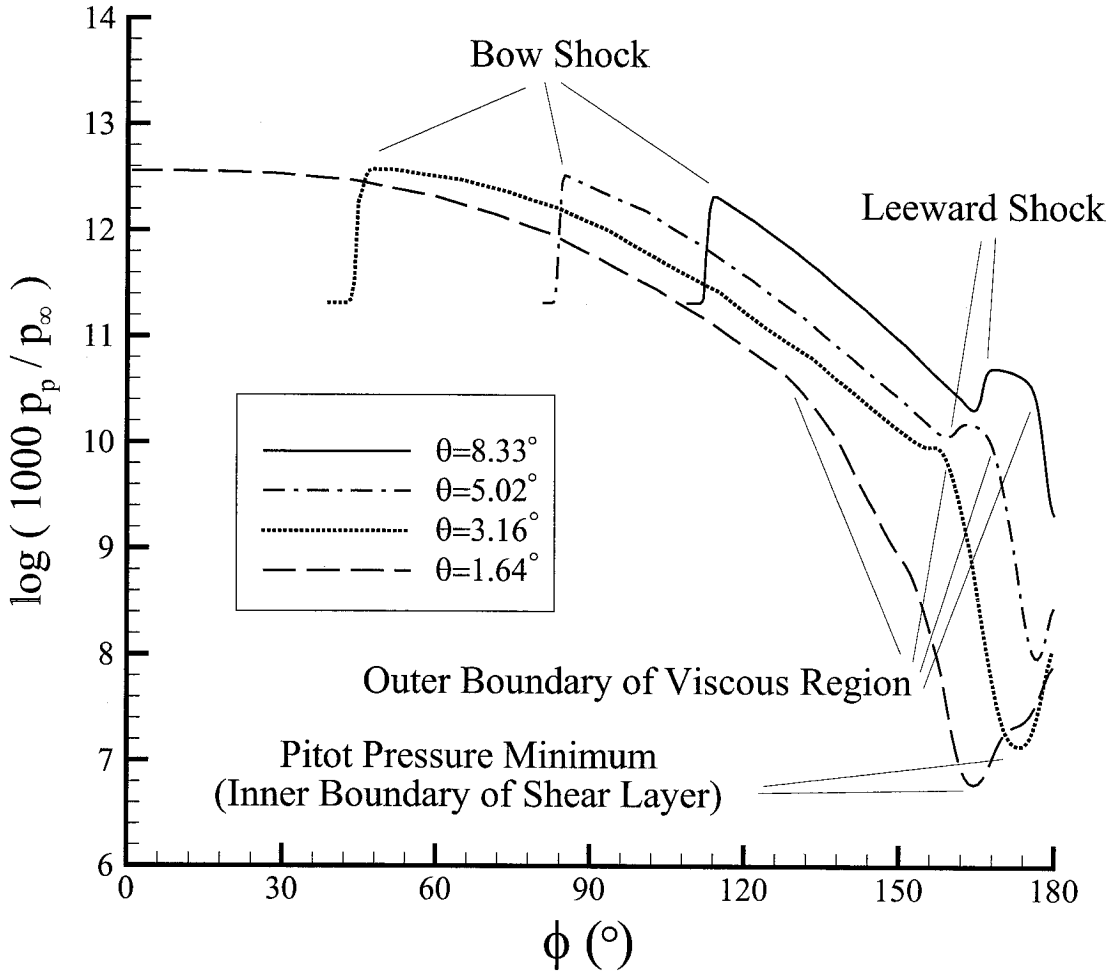

Figure 4.1 Criteria for defining domains of field from pitot pressure traverses at constant radii from the cone. θ is the angle from the surface of the cone, ϕ is the azimuthal angle, and p_p is the pitot pressure.

from this surface. Contour plots and profiles are taken at a constant radius from the tip, and streamlines shown are crossflow streamlines, where only the components of velocity lying on the sphere are integrated to obtain the streamlines. The second view is from the side of the cone, with the freestream moving horizontally from left to right and the cone axis lying in the plane of the page, inclined to the horizontal. The third view shows the curvature of the spherical surface which the grid lies on. Note that the grid presented in Figure 4.2 has a much lower resolution than the grids used in this section so that the cell stretching

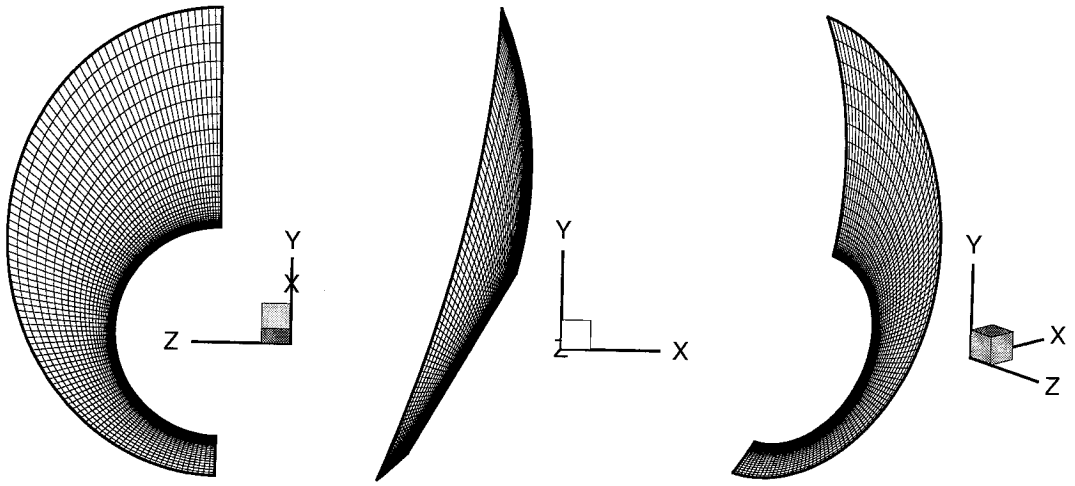

Figure 4.2 Typical stepback grid for a cone at incidence ($2 \times 45 \times 100$)

can be better seen. At this high resolution, the very small cell sizes rendered an explicit calculation impractical, so these results were obtained with the implicit formulation. For the cone at zero incidence, the stepback computation used 150 cells away from the surface of the cone ($2 \times 150 \times 2$).

4.3 Comparison with Experimental Results

This section details the results from the calculations performed, and the comparison with experiment.

4.3.1 Zero Incidence Case

The first calculation performed was a stepback calculation used to measure the heat transfer on a zero incidence cone. Due to the high resolution, there were only minor differences between the EFM and EFMO results here (see Section 3.5.2). Figure 4.3 shows a comparison of the EFM and EFMO boundary layers at Re_x=4.2×10^5. The boundary layer is very thin, about 0.5° thick. Contrast this with the adiabatic boundary layers from the

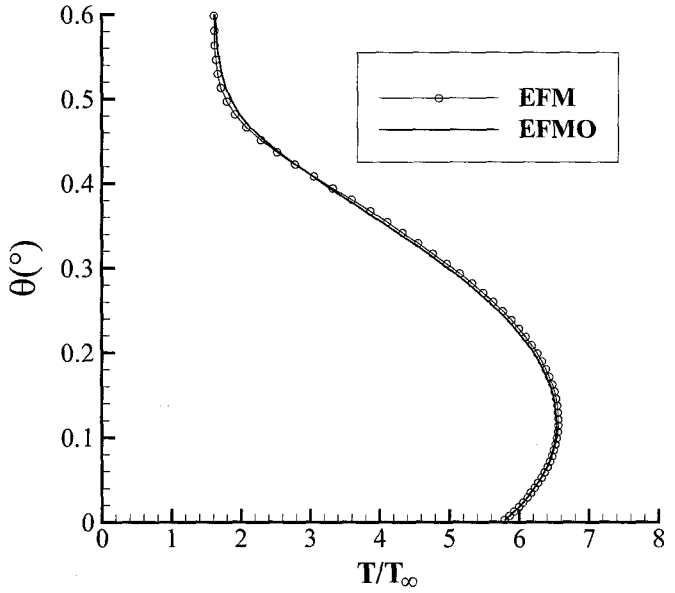

Figure 4.3 Comparison of EFM and EFMO boundary layer profiles for a 10° cone at zero incidence. Stepback, Tracy conditions, M=7.95. Isothermal wall at 317 K, Pr = 0.72, $Re_x = 3.6 \times 10^5$. θ is the angle from the cone surface, T_∞ is the freestream temperature, U_∞ is the freestream velocity.

previous chapter, which were almost twice as thick. The slight difference between EFM and EFMO in the temperature gradient at the wall is enough to cause a significant difference in the heat transfer. For EFM, the computed zero incidence heat transfer $q_0 = 7576$ W/m^2, while for EFMO, $q_0 = 8919$ W/m^2. Figure 4.4 shows the boundary layer including the shock wave for the EFMO computation.

4.3.2 Surface Conditions

Next, the cone at incidence was calculated using the high-resolution stepback grid. Figure 4.5 shows the surface pressure versus azimuthal angle, while Figure 4.6 shows heat transfer versus azimuthal angle. Both have been normalized in the same way that Tracy did. The non-dimensional surface pressure is presented as 1000 times the surface pressure divided by the freestream stagnation pressure, or

$$\widetilde{p} = 1000 \left(\frac{p}{p_{0\infty}} \right). \tag{4.2}$$

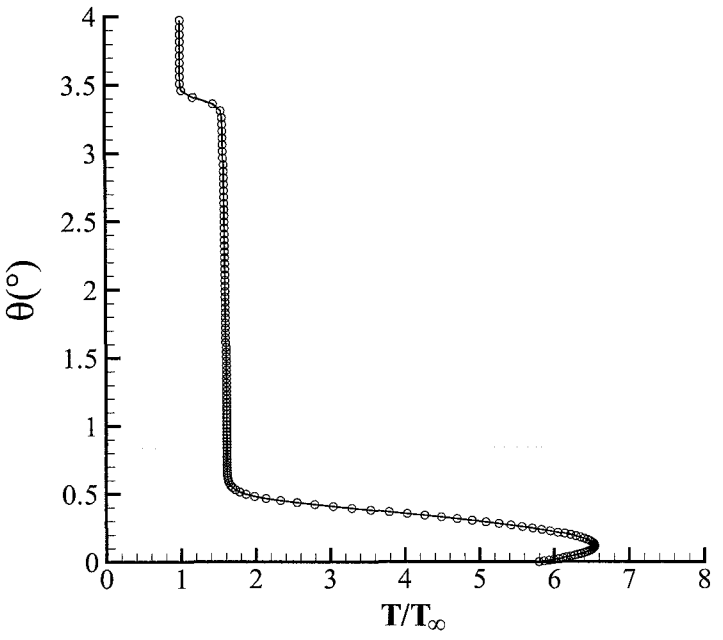

Temperature

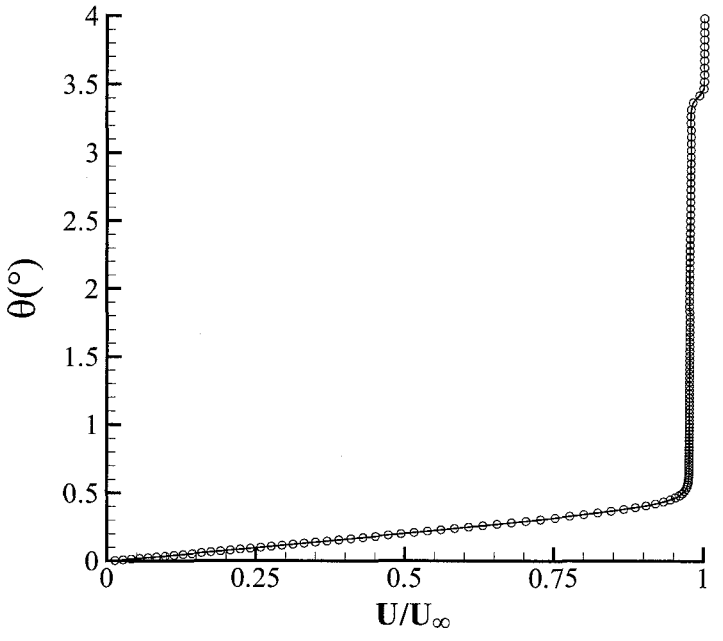

Velocity

Figure 4.4 Boundary layer profiles for a 10° cone at zero incidence. EFMO step-back, Tracy conditions, M=7.95. Isothermal wall at 317 K, θ is the angle from the cone surface, T_∞ is the freestream temperature, U_∞ is the freestream velocity. $Pr = 0.72$, $Re_x = 4.2 \times 10^5$.

The non-dimensional heat transfer is presented as the ratio of the heat transfer to the heat transfer at the same Reynolds number on a cone at zero incidence,

$$\tilde{q} = \left(\frac{q}{q_0}\right). \tag{4.3}$$

The agreement is good with the pressure slightly underpredicted for both methods. There

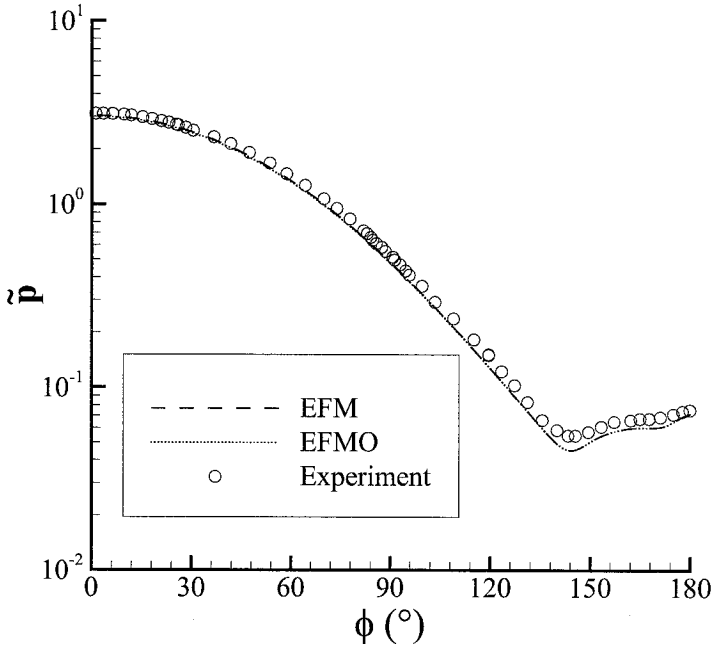

Figure 4.5 Normalized surface pressure ($\tilde{p} = 1000\, p/p_{0\infty}$) vs. azimuthal angle for a 10° cone at 24° incidence. Tracy conditions, M=7.95. Stepback. Isothermal wall at 317 K, Pr = 0.72, $\mathbf{Re_x = 3.6 \times 10^5}$.

is no difference between the EFM and EFMO calculations. Both profiles agree very well with the experiment for the location of minimum pressure, the surface pressure plateau, and the subsequent rise in pressure at the leeward plane. The surface pressure drops as the flow expands around the cone, reaching a minimum value just upstream of the shock-boundary layer interaction at $\phi \approx 144°$. Here the pressure rises until it reaches the separation point, at $\phi = 152.5°$, as determined from the crossflow streamlines. This is the beginning of the pressure plateau in the separated region, which is followed by the local pressure maximum where the separated shear flow reattaches at the leeward plane of symmetry. The crossflow streamlines are useful for determining the posisiton of separation. Recall that only the

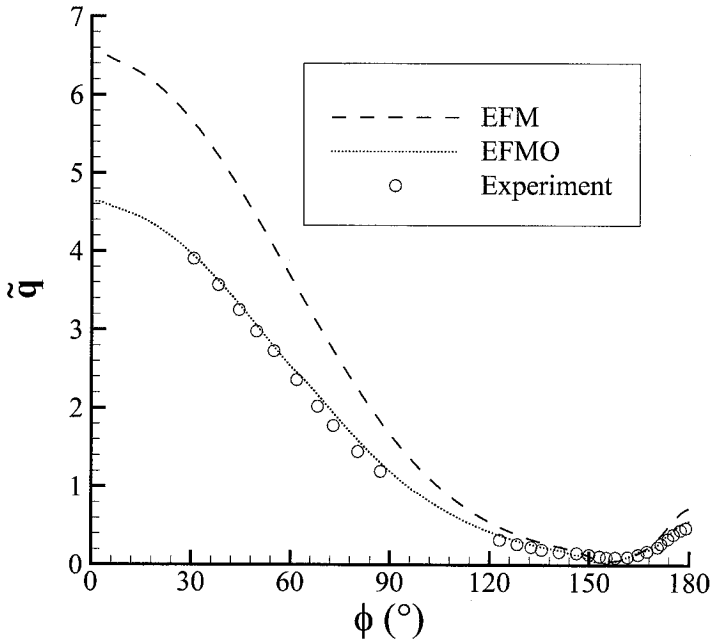

Figure 4.6 Normalized heat transfer ($\tilde{q} = q/q_0$) vs. azimuthal angle for a 10° cone at 24° incidence. Tracy conditions, M=7.95. Stepback. Isothermal wall at 317 K, $\mathbf{Pr = 0.72, Re_x = 3.6 \times 10^5}$.

components of velocity lying on the sphere are integrated to obtain the crossflow streamlines. Streamlines may be plotted very close to the separation point to determine quite accurately where the crossflow streamlines lift from the surface.

The heat transfer is the flow feature most sensitive to the method. Whereas neither contour plots nor surface pressure show any distinction between the methods (at least for a very high-resolution simulation such as this one), the heat transfer plot displays the superiority of EFMO for viscous simulations. With the exception of the region near separation ($144° < \phi < 162°$), the heat transfer is remarkably well-predicted by EFMO at this resolution, except near the separation point, where it slightly underpredicts the heat transfer. EFM overpredicts the heat transfer everywhere at this resolution. Like the pressure, the heat transfer drops as the flow expands around the cone. The heat transfer reaches a minimum at the separation point, and rises in the separated region.

The non-dimensionalized EFM heat transfer is approximately 1.4 times the EFMO heat transfer. Coincidentally, the zero incidence heat transfer q_0 for EFM was approximately $\sqrt{1.4}$ times the q_0 for EFMO, leading one to the possible conclusion that the EFM heat transfer scales linearly with the EFMO heat transfer, and that this was compounded by normalizing the heat transfer by q_0. However, this sort of behavior has not been seen in any other comparisons of EFM and EFMO.

4.3.3 Flow Features

Figure 4.7 shows comparisons of Tracy's flow field with the high-resolution stepback EFM run. Mach number contours from the simulation have been superimposed over Tracy's findings[1]. Many features agree well, including the thickness of the boundary layer, the point of separation, and the position of the separated shear layer. The position of the leeward shock system is fairly good, although slightly skewed. The windward shock standoff was not well-predicted by the simulation; the thickness of the shock layer was slightly overpredicted and the pressure was slightly underpredicted. This suggested that perhaps the Tracy freestream Mach number was not accurately reported and was in fact higher than 7.95. An estimate was made for the Mach number which might produce the same

[1]The image was created by superimposing two postscript files. This was accomplished in a six-line *Amrita* script. Amrita [56] is a software system for numerical investigations, and its scripting language *Amrita* has many commands for performing otherwise arduous documentation tasks. This is one example of a mundane use of Amrita, which is a powerful framework for rigorous numerical sumulations.

shock standoff distance as Tracy's findings. Another simulation was performed with the freestream raised to M=8.3. The shock position and surface pressure agreed more closely with Tracy's findings, but only slightly.

This simulation was repeated with the EFMO method, and Figure 4.8 shows a comparison of temperature contours for the two methods. There is virtually no discernible difference between the contours from the two calculations, and the remainder of the contours shown here are for EFMO. Figure 4.9 shows contours of $\log p$, which emphasize the λ-shock, and contours of $\log p_p$, where p_p is the pitot pressure. The utility of the pitot pressure in defining domains of the flow has been discussed above. Finally, Figure 4.10 shows Mach number contours and contours of $\log \rho$.

4.3.4 Profiles from the Surface

The next two figures show profiles away from the cone surface. Figure 4.11 shows a comparison of temperature profiles at the windward plane of symmetry for EFM and EFMO. Again, there is not a large difference between the two methods. The viscous region is larger for EFM, and the temperature gradient at the wall is slightly higher. This results in a higher dimensional heat transfer for EFM, which is compounded in the non-dimensional form $\widetilde{q}$ because the zero incidence heat transfer q_0 is smaller for EFM than for EFMO.

A number of temperature profiles were taken at constant values of ϕ. These were taken along the rows of cells $k = 200$, 150, 100, 50, 10, and 1, where the first cell $k = 1$ lies on the leeward plane of symmetry. These rows correspond to $\phi = 0.6°, 58.3°, 109.6°, 150.4°, 175.1°$, and 179.7°, respectively. The lines which these profiles were taken from are shown in Figure 4.12, which shows Mach number contours. The temperature profiles are shown in Figure 4.13.

At $\phi = 0.6°$, the profile is typical of stagnation region flow. The bow shock is quite strong, and stands off the cone at $\theta \approx 2.5°$. The temperature is nearly constant behind the bow shock, and the boundary layer is about 0.25° thick. Because the adiabatic wall temperature is higher than the prescribed wall temperature, the temperature profile overshoots the wall temperature before dropping to meet the boundary condition.

At $\phi = 58.3°$, the qualitative features of the profile are much the same. The bow shock stands off here at $\theta \approx 3.5°$, and the temperature rise behind the shock is less due to the

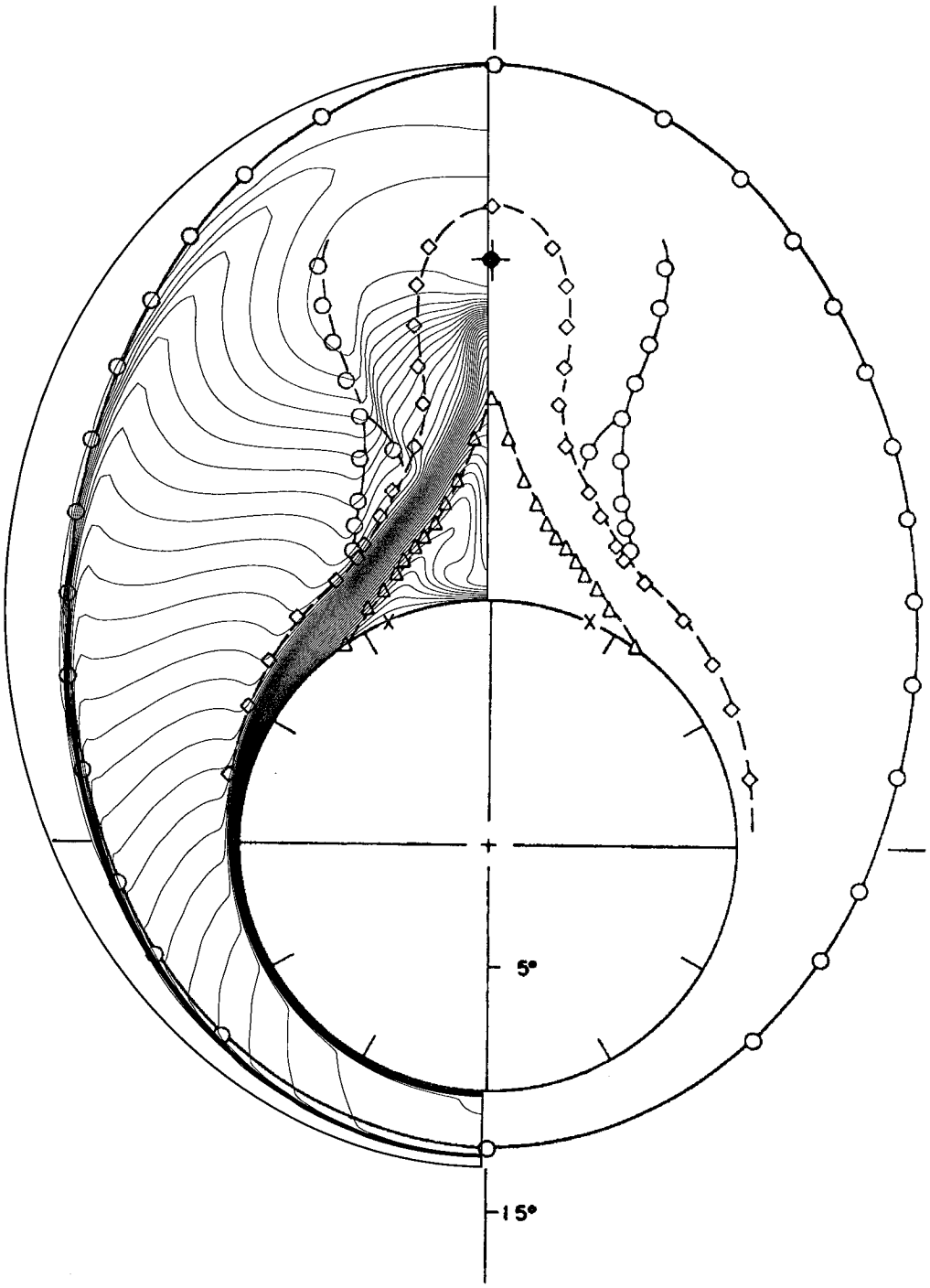

Figure 4.7 Comparison of EFM Mach number contours and the Tracy flow field as determined from pitot probe traverses. 10° cone at 24° incidence. Stepback, Tracy conditions, M=7.95. Isothermal wall at 317 K, Pr = 0.72, $Re_x = 4.2 \times 10^5$. In the Tracy flow field, ○ denotes shocks, ◇ denotes viscous boundaries, △ denotes the minimum pitot pressure, and × denotes the surface pressure plateau.

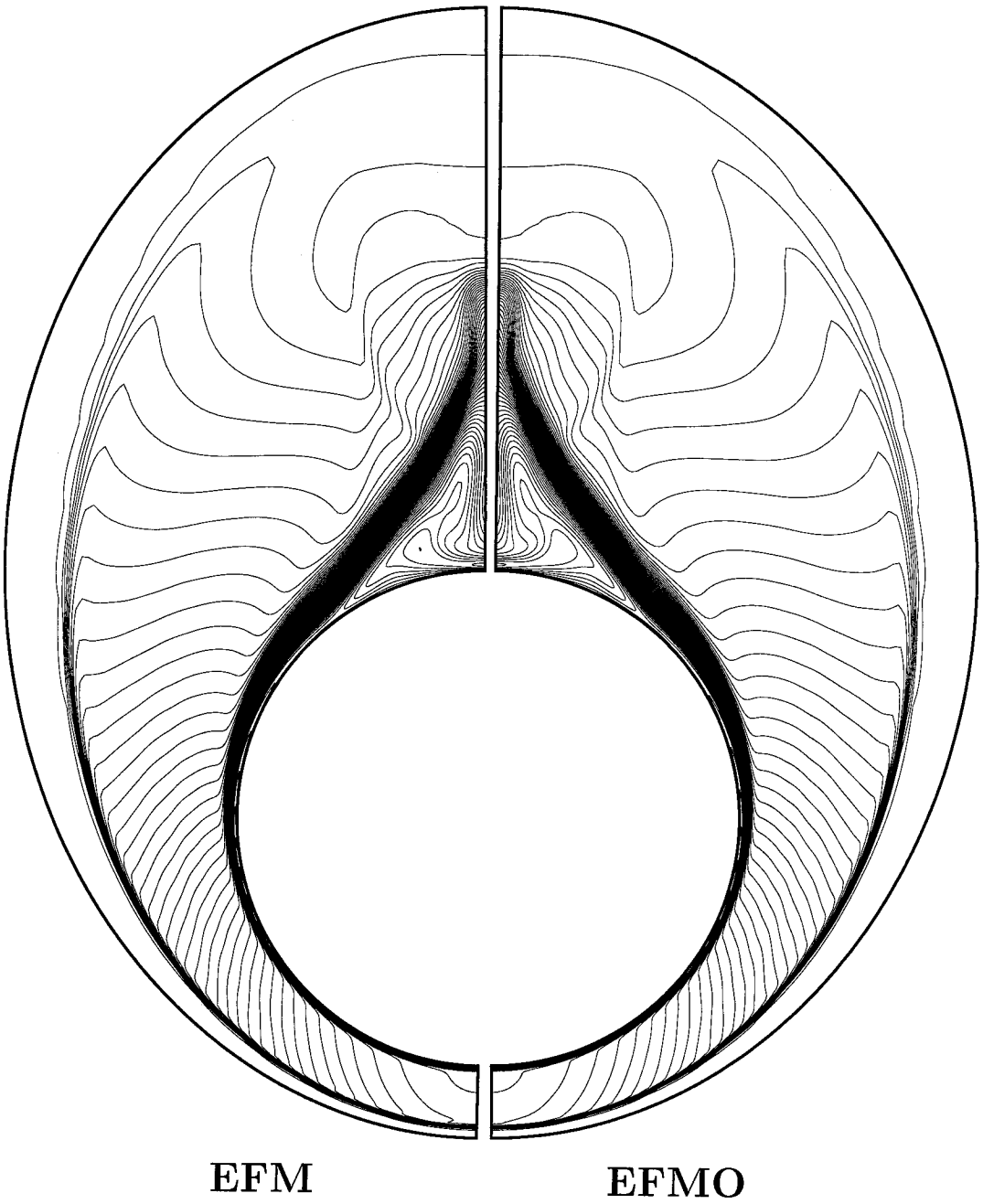

Figure 4.8 Temperature contours comparing EFMO and EFM methods for a 10° cone at 24° incidence. Stepback, Tracy conditions, M=7.95. Isothermal wall at 317 K, $Pr = 0.72$, $Re_x = 4.2 \times 10^5$.

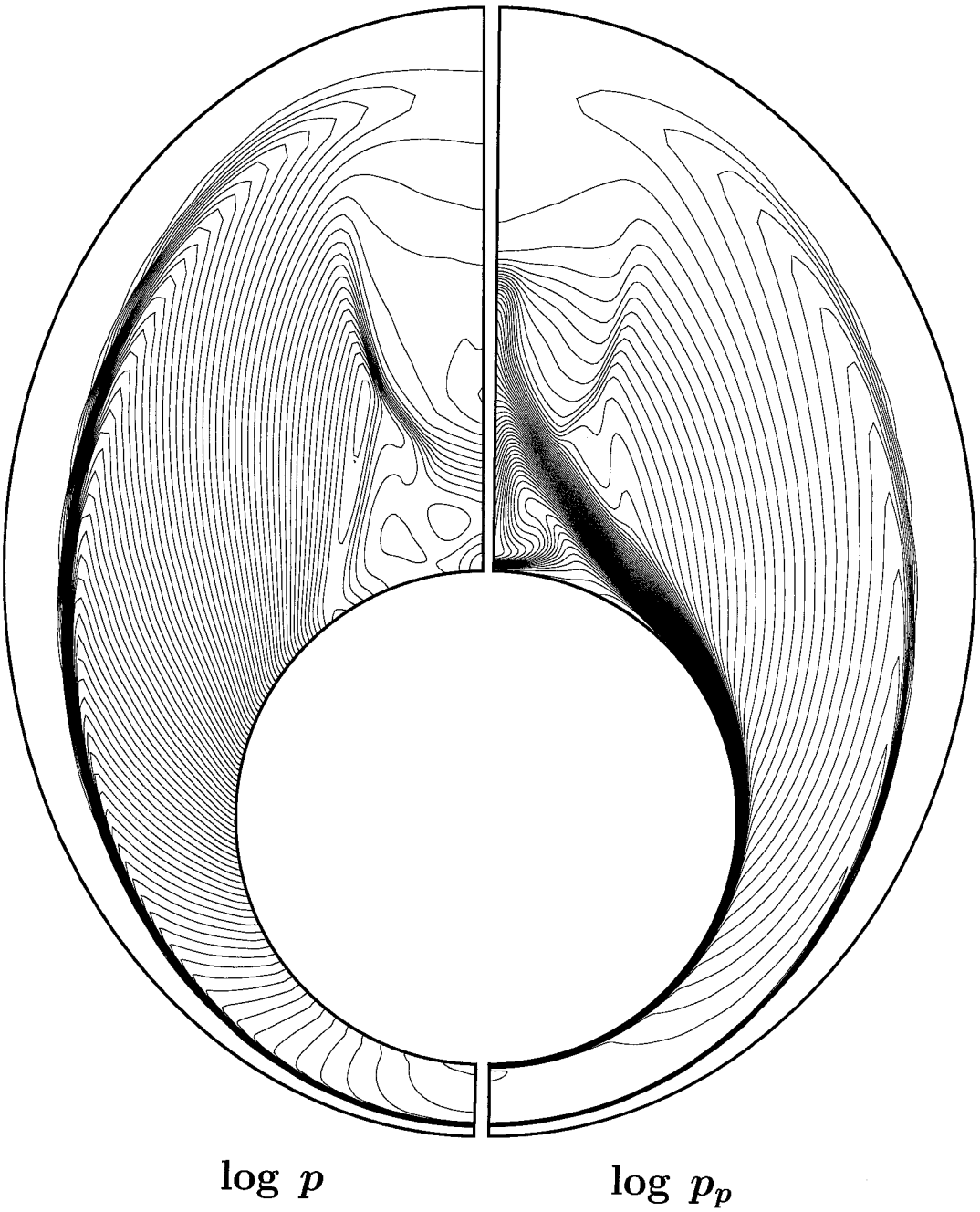

Figure 4.9 Pressure and pitot pressure contours for a 10° cone at 24° incidence. EFMO stepback, Tracy conditions, M=7.95. Isothermal wall at 317 K, Pr = 0.72, $Re_x = 4.2 \times 10^5$.

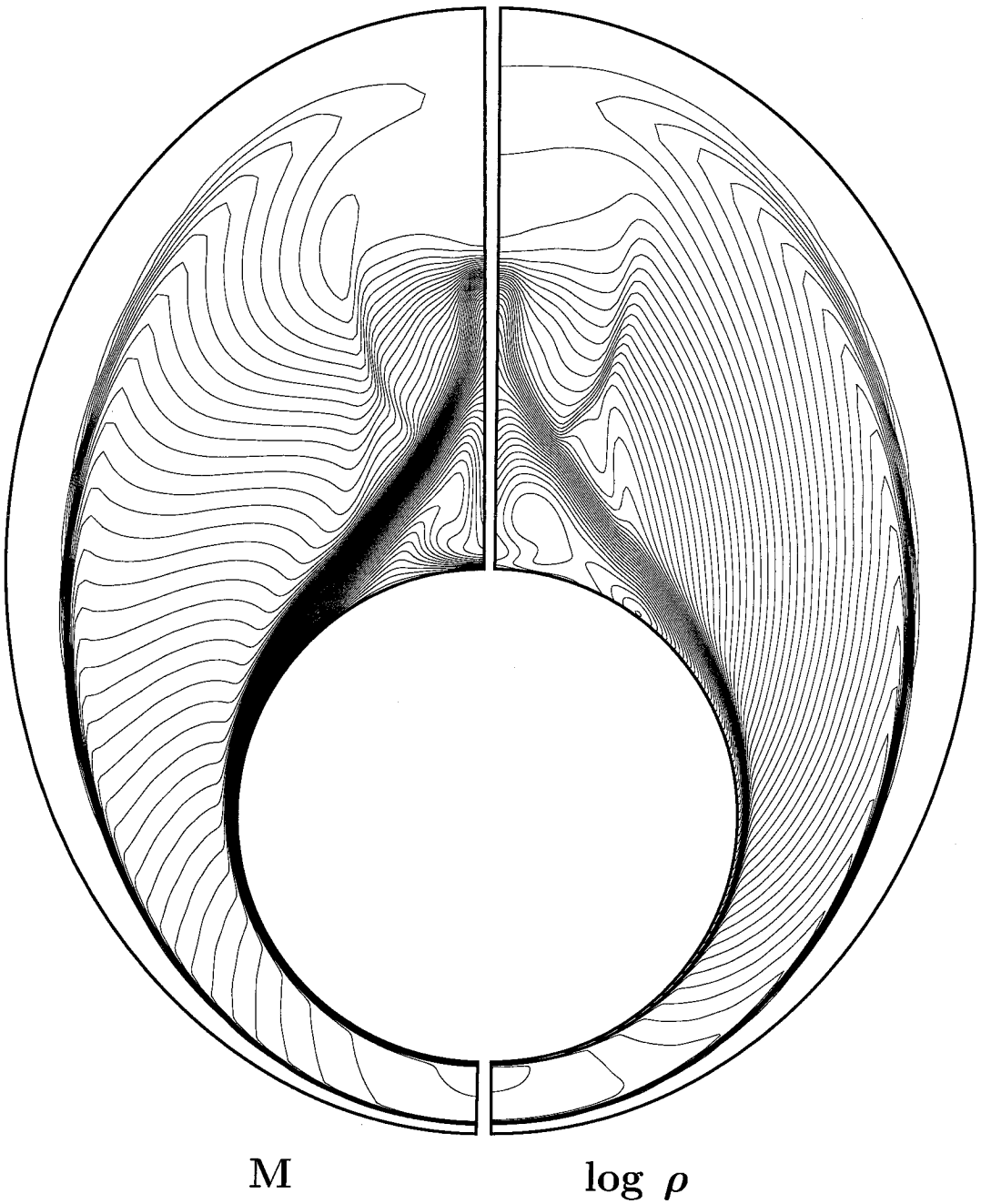

Figure 4.10 Mach number contours and density contours for a 10° cone at 24° incidence. EFMO steoback, Tracy conditions, M=7.95. Isothermal wall at 317 K, $Pr = 0.72$, $Re_x = 4.2 \times 10^5$.

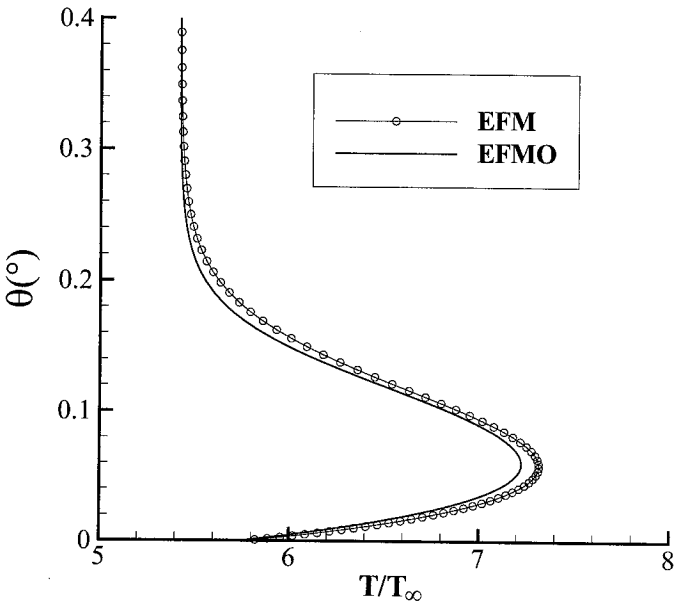

Figure 4.11 Comparison of EFM and EFMO profiles at windward plane ($\phi = 0°$) of a 10° cone at 24° incidence. Stepback, Tracy conditions, M=7.95. Isothermal wall at 317 K, Pr = 0.72, $Re_x = 4.2 \times 10^5$.θ is the angle from the cone surface, T_∞ is the freestream temperature.

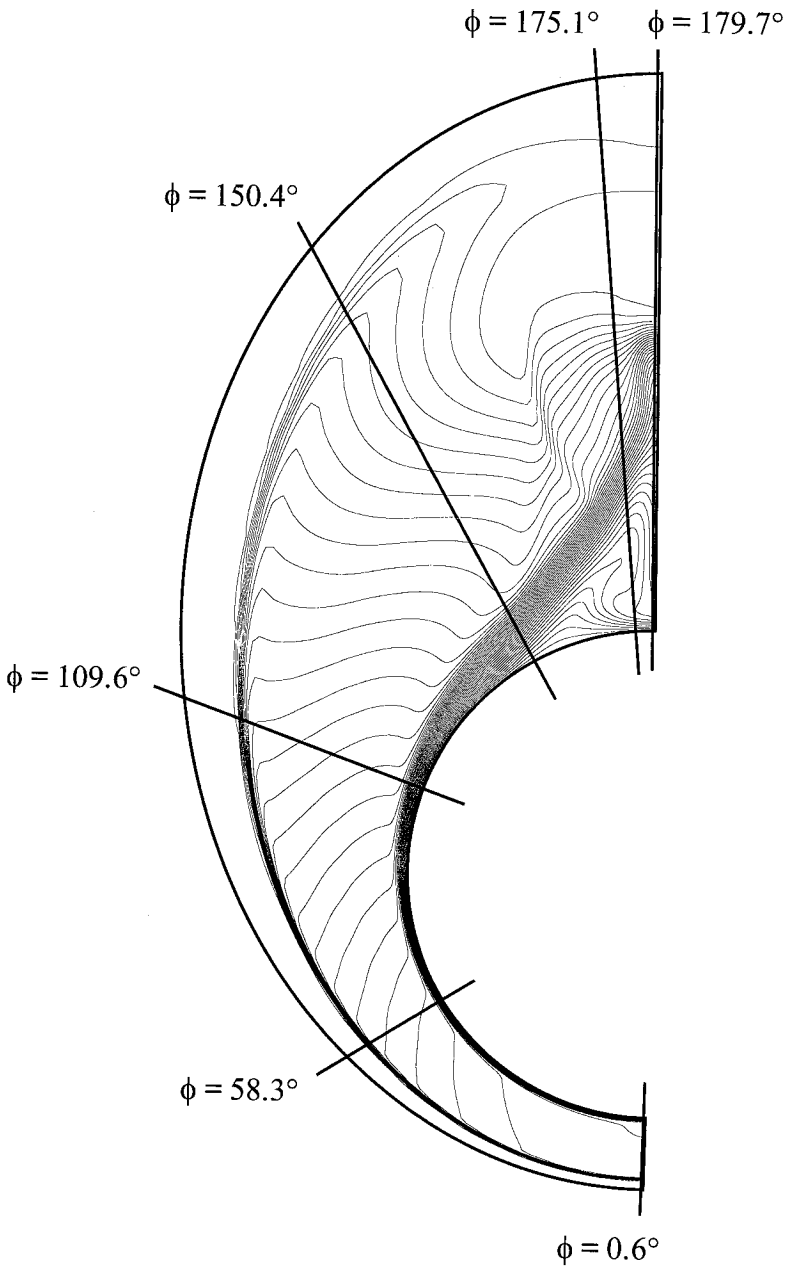

Figure 4.12 Lines of constant ϕ for Figure 4.13

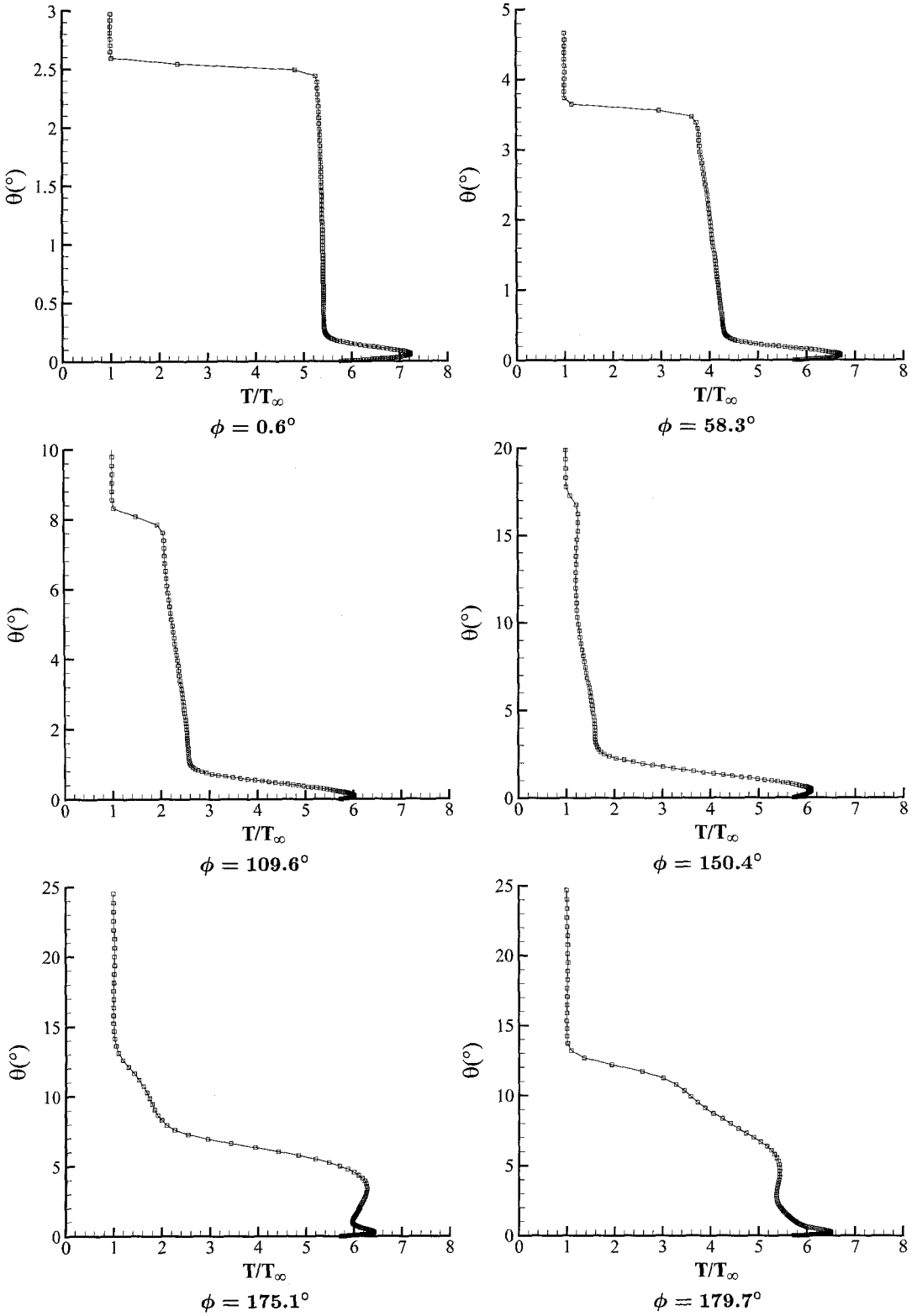

Figure 4.13 Temperature profiles along constant values of ϕ for a 10° cone at 24° incidence. Stepback EFMO, Tracy conditions, M=7.95. Isothermal wall at 317 K, $Pr = 0.72$, $Re_x = 4.2 \times 10^5$. θ is the angle from the cone surface, T_∞ is the freestream temperature.

expansion around the cone.

At $\phi = 109.6°$, the shock stands at $\theta \approx 8°$, and is substantially weaker. The boundary layer thickness has grown to about 1°.

At $\phi = 150.4°$, the bow shock stands at $\theta \approx 17.5°$, and is quite weak. The temperature drops below the post-shock value due to the expansion, and the boundary layer has grown to 2.5°.

At $\phi = 175.1°$, the bow shock is so weak that it is not seen on the temperature profiles (it stands at $\theta \approx 22°$). The temperature rises behind the leeward shock system from $\theta = 14°$ to $\theta = 7.5°$. This increase is not discontinuous because the leeward shock system has a strength gradient, as discussed in Section 1.1. The first part of this temperature rise (from $\theta = 14°$ to $\theta = 11°$) is due to the outermost part of the λ-shock. The second part of the rise is due to the lower part of the shock, where the fluid has been shocked twice. Following this, there is a large temperature rise as the profile cuts across the separted shear layer and enters the hot recirculation zone. The temperature drops as the fluid is accelerated into the vortex, only to rise again in the boundary layer and finally drop back to the surface temperature.

Finally, for $\phi = 179.7°$, the first significant rise in temperature is seen at the node point on the leeward plane of symmetry (the node can be seen more clearly in Figure 4.15 below). The temperature rises further where the the two separated shear layers collide at the leeward plane of symmetry, and then follows the same behavior as for $\phi = 175.1°$.

4.3.5 Leeward Shock-Vortex System

Figures 4.14–4.15 show closeups of the calculated leeward shock-vortex system plotted with contours of various quantities. These figures show many features of the leeward flow. The streamlines are crossflow streamlines, and crossflow separation occurs at $\phi = 152.5°$. The distance between the arrows on the streamlines is proportional to the velocity, and show the relative speed of the flow.

In Figure 4.14, contours of $\log p$ are plotted, and the λ-shock is clearly visible. The node point on the leeward plane of symmetry is clearly seen where the streamlines converge. All of the fluid which does not enter the vortex ends up asymptotically approaching the radial line passing through the node point.

Figure 4.15 shows Mach number contours. Here the sonic contour (M=1) is the thick contour near the surface of the cone. It is interesting to note that the fluid nearest the surface is subsonic upstream of the separation point, but is accelerated to supersonic speeds as it enters the leeward vortex. Some of this fluid crosses the sonic line again as it flows past the surface in the reversed region, only to finally remain supersonic as it enters the essentially inviscid vortex core.

In Figure 4.16, the contours are temperature contours. The λ-shock is still visible, but the most prominent feature of this figure is the shear layer. Although it might be tempting to believe that the inner edge of the area with the densest contours is the edge of the shear layer, the crossflow streamlines show that separation actually occurs about 8°–10° later. The edge of the dense contours corresponds to the maximum temperature. The shock-boundary layer bends the shear layer away from the cone, but this does not immediately cause separation. The hot, slow fluid near the surface of the cone expands to accomodate this, and separation does not occur until slighty later. Lastly, Figure 4.17 shows color temperature contours for the Tracy case. Most of the flow features are clearly seen, especially the λ-shock and the separated boundary layer.

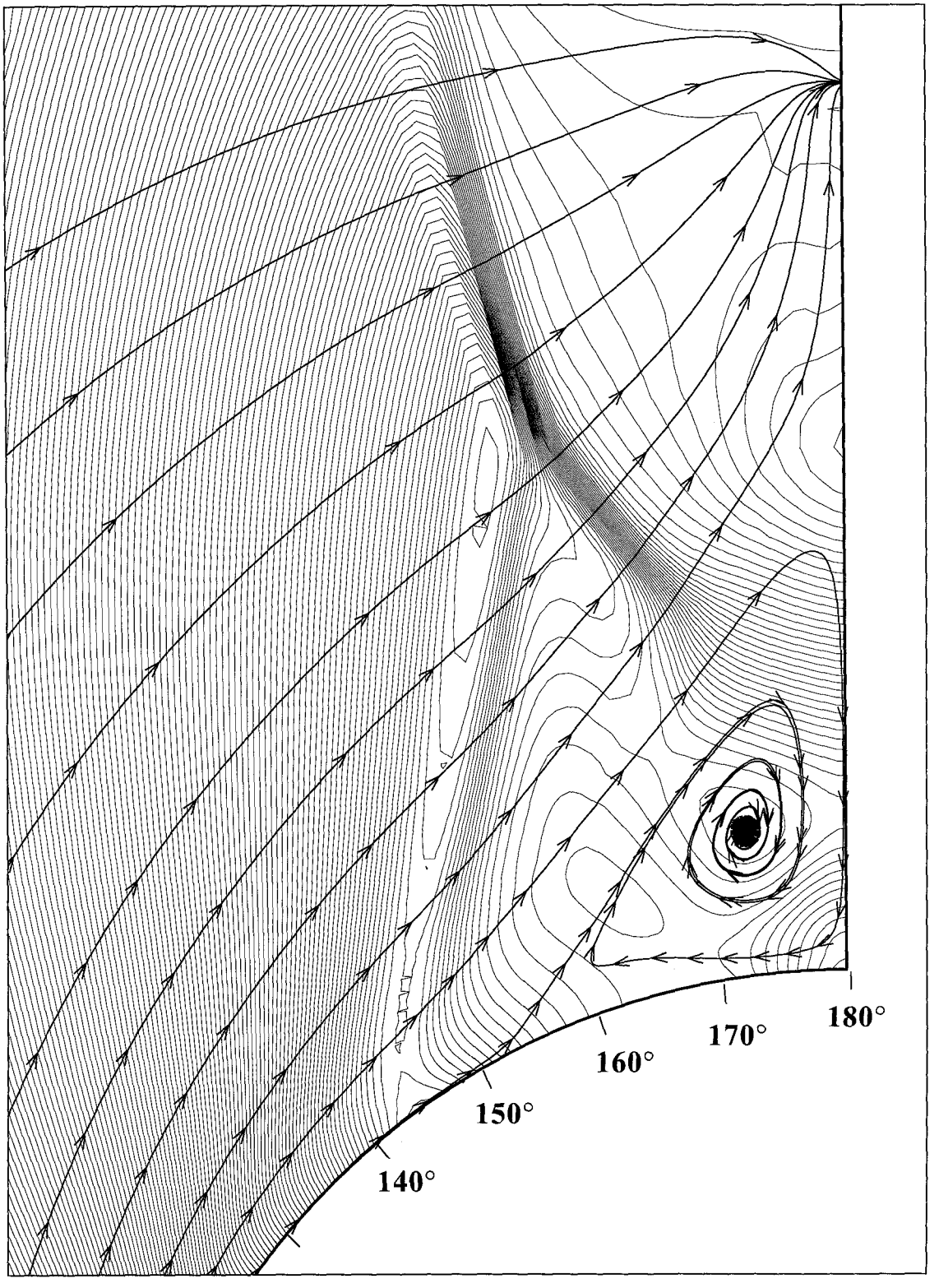

Figure 4.14 Leeward shock-vortex system. Contours of $\log p$ and crossflow streamlines are plotted, and the value of ϕ is indicated. Stepback EFMO, Tracy conditions, M=7.95. Isothermal, T_w=317 K, Pr = 0.72, $Re_x = 4.2 \times 10^5$.

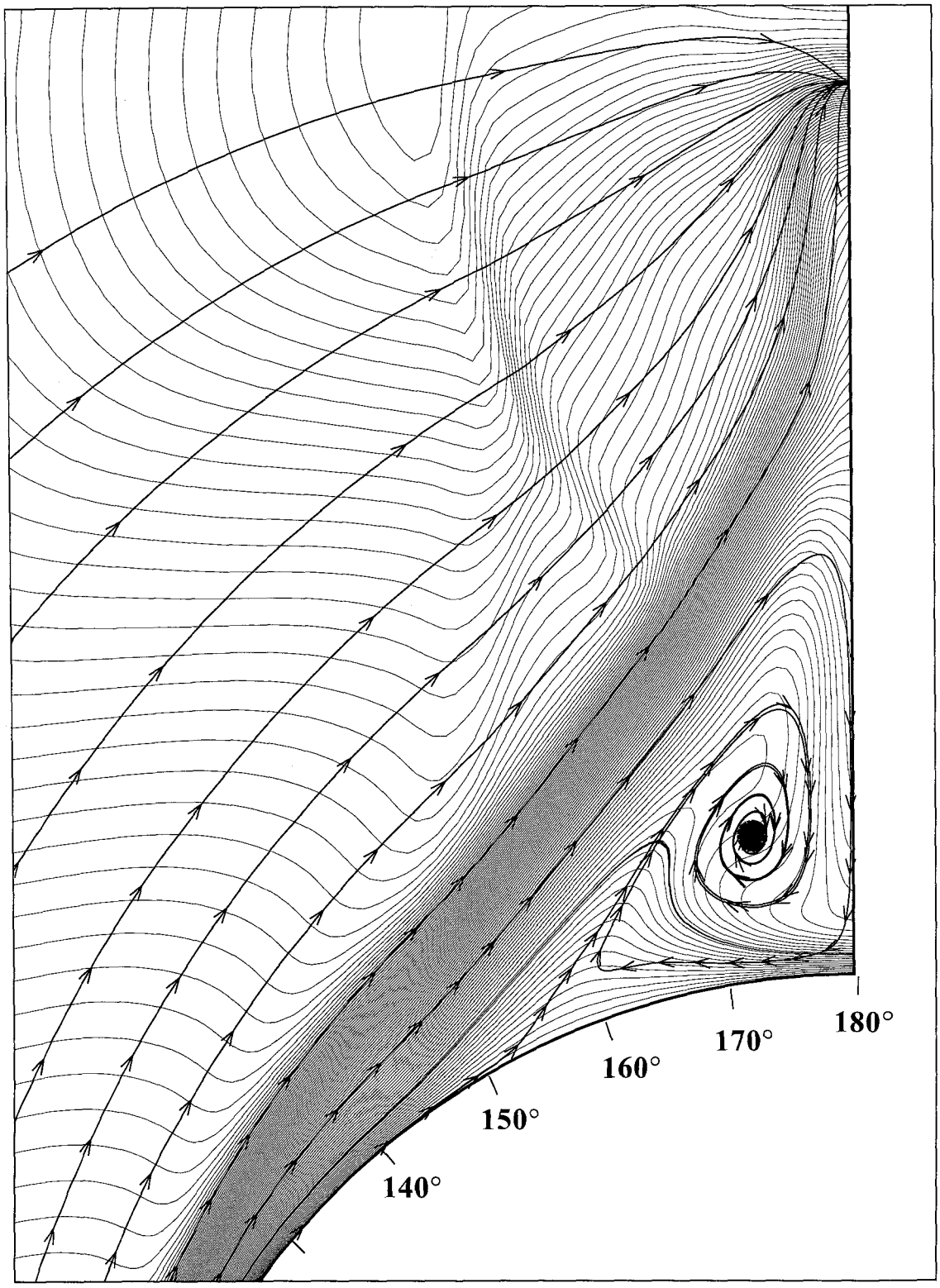

Figure 4.15 Leeward shock-vortex system. Contours of M and crossflow streamlines are plotted, and the value of ϕ is indicated. The dark contour is the sonic line. Stepback EFMO, Tracy conditions, M=7.95. Isothermal, T_w=317 K, Pr = 0.72, $Re_x = 4.2 \times 10^5$.

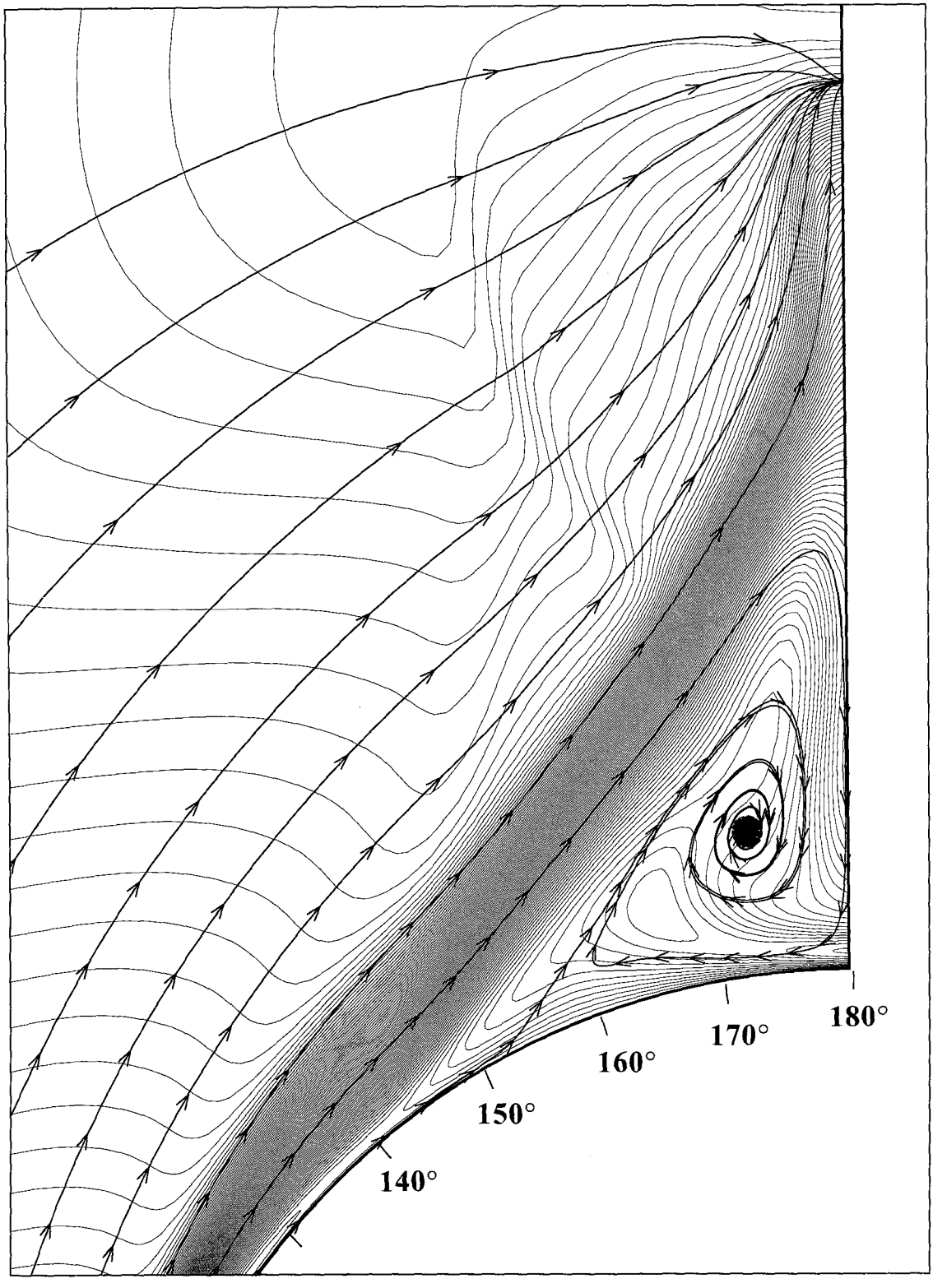

Figure 4.16 Leeward shock-vortex system. Contours of T and crossflow streamlines are plotted, and the value of ϕ is indicated. Stepback EFMO, Tracy conditions, M=7.95. Isothermal, T_w=317 K, Pr = 0.72, $Re_x = 4.2 \times 10^5$.

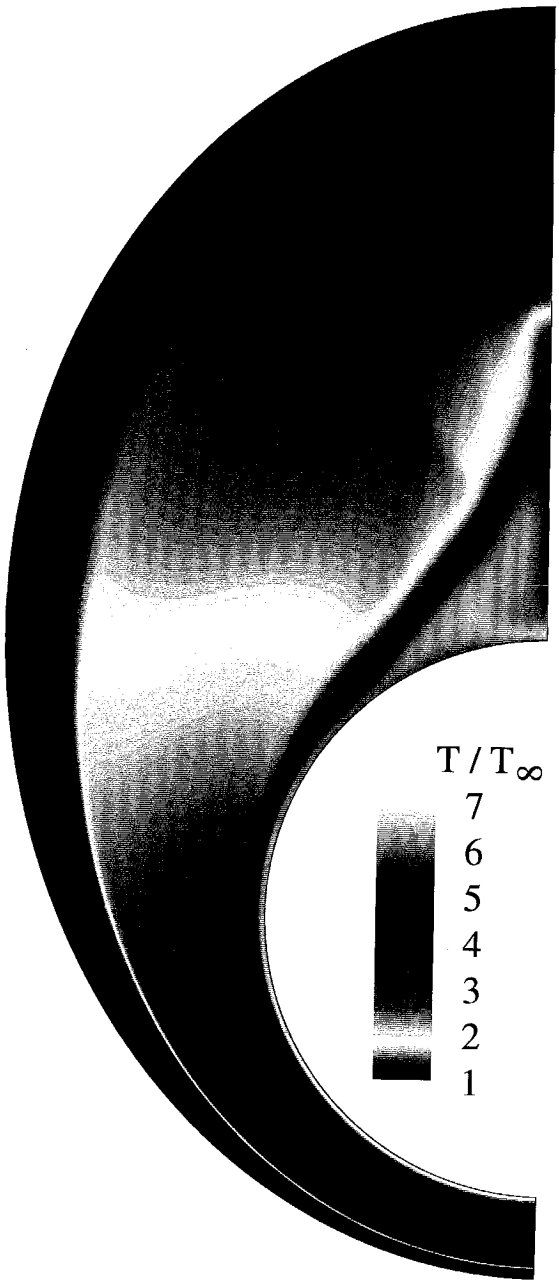

Figure 4.17 Temperature contours from stepback simulation. 10° cone at 24° incidence. Tracy conditions, M=7.95. EFMO. Isothermal, T_w=317 K, Pr = 0.72, $Re_x = 4.2 \times 10^5$.

Chapter 5

Dissociating Cone Flow

This chapter describes the reacting flow simulations. Comparisons were made with the experiments of Krek [6], who examined heat transfer and surface pressure measurements on a cone at incidence. Krek's experiments were performed on a 15° half-angle cone at 30° incidence in nitrogen. Its length $L = 0.18$ m, and the Reynolds number (based on cone length and freestream conditions) was 9.9×10^4. Circumferential heat transfer and pressure measurements were taken at five downstream stations, and these are compared to stepback calculations and partial grid calculations. Results have been measured experimentally at $(r/L) = 0.34, 0.46, 0.58, 0.69$, and 0.81, where r is the distance from the cone tip. Stepback solutions using EFMO were computed for all of these locations, as well as at $(r/L) = 0.10$, which was used as the boundary condition for the partial grid runs.

5.1 Test Conditions and Experimental Details

Krek's experiment was conducted in the University of Queensland's free piston shock tunnel, known as T4. In a shock tunnnel, a high pressure reservoir forces a piston down a compression tube, which compresses the driver gas (here, the driver gas was helium). At sufficient pressure, the driver gas ruptures the primary diaphragm, sending a strong shock wave into the test gas. The shock moves down the shock tube, compressing and heating the test gas. The shock reflects off the end of the shocktube, and travels back up the shocktube, raising the pressure high enough to rupture the secondary diaphragm. This allows the test gas to flow through the nozzle and into the test section.

It has been shown that T4 can experience considerable driver gas contamination [57]. This means that the contact surface between the driver gas and the test gas has allowed some of the driver gas to enter what should be a plug of constant state test gas.

This was known at the time of the Krek experiments, and care was taken to limit the test times to before the onset of driver gas contamination. The tunnel was operated in

an undertailored condition, meaning that the pressure on the contact surface between the driver gas and the test gas is not matched. When the reflected shock hits an undertailored contact, it creates an expansion wave which moves through the test gas. This allows a longer test time, because it delays contamination of the test gas by the driver gas. The drawback of operating undertailored is that the stagnation pressure is not constant during the test. However, as the stagnation pressure drops, so does the pitot pressure. The ratio of stagnation pressure to pitot pressure is fairly constant throughout the tests, so Krek normalized the static pressure measurements by the pitot pressure with

$$\bar{p} = \left(\frac{p}{p_P}\right). \tag{5.1}$$

Similarly, the heat transfer measurements drop during the tests, but followed the pitot pressure's decay in time. To account for this effect, Krek's heat transfer data were normalized by the ratio of the instantaneous pitot pressure to the inital pitot pressure at the beginning of the test. They were further normalized by the heat transfer at the same Reynolds number for the zero incidence cone:

$$\bar{q} = \left(\frac{p_P}{p_{P0}}\right)\left(\frac{q}{q_0}\right). \tag{5.2}$$

Since the numerical freestream pitot pressure is constant, the notation q_0 is used hereafter, keeping in mind that the experimental results were normalized by the variable pitot pressure.

The heat transfer measurements were made with two types of devices: thermocouples and thin film heat flux gauges. The thermocouples were used on the windward side of the cone ($0° < \phi < 90°$), and the thin film gauges were used on the leeward side ($90° < \phi < 180°$). The thermocouples were not a good quantitative measure, but rather a qualitative measure. The thin film gauges provide a good quantitative measurement, but were not robust enough to withstand the harsh conditions on the windward side of the cone.

The Krek freestream conditions are shown in Table 5.1. These conditions are calculated freestream conditions, based on the fill conditions for the shock tube and driver gas. Two codes are used; one calculates the conditions in the shock tube, and the other computes the flow leaving the nozzle and entering the test section [6]. This table includes the stagnation

enthalpy h_0, where

$$h_0 = R_{N_2}[\alpha\,\theta_d + (4+\alpha)T\,] + \frac{1}{2}u^2. \tag{5.3}$$

An isothermal wall boundary condition was assumed, since the test times are so short in a shock tunnel that the cone does not heat up significantly during the duration of the measurements. The cone was assumed to be at a constant temperature $T_w = 317$ K.

At the Reynolds numbers of this test, the boundary layer was laminar everywhere.

5.2 Chemical Freezing and Equivalent Conditions

The flow at the end of the shock tube of the T4 tunnel is expanded through a hypersonic nozzle. When the gas enters the nozzle, it is in chemical equilibrium with a high degree of dissociation. As the gas expands through the nozzle, the species composition departs from equilibrium, with the recombination reaction "freezing." The dissociation rate is highly dependent on the temperature, but the recombination rate depends on density and can be turned off or "quenched" by the expansion. This leaves the gas with a large degree of dissociation, far from equilibrium. When the gas crosses the bow shock of the model, the gas can further dissociate but the compression of the shock wave reinitiates the recombination term of the rate equation, and the chemistry then proceeds as the gas expands toward the leeward plane of symmetry.

This presents a problem in terms of utilizing the stepback method (or the partial grid method, since it must start from a stepback solution). Stepback solutions must be either in chemical equilibrium or frozen. In order to apply the stepback method, an equivalent equilibrium flow had to be selected for the freestream. It is not clear which flow quantities should be maintained, and the initial selection of an equivalent freestream was too different to bear comparison with the experimental results.

The system has four degrees of freedom. The first choice of conditions was based on maintaining the same mass, momentum, and total enthalpy of the Krek freestream, while enforcing the law of mass action. These are the same relations which would be used to to pass the flow through an equilibrium shock. However, since the flow was not initially in equilibrium, there are two solutions, one subsonic solution and one supersonic solution.

	Krek conditions	Shocked conditions	Low-α conditions
M	4.57	3.60	4.99
ρ (g/m^3)	9.33	9.53	9.33
u (m/s)	5683	5565	5683
T (K)	3273	5381	3273
p (kPa)	10.43	16.67	9.071
h_0 (MJ/kg)	27.17	27.17	20.04
h_{0d} (MJ/kg)	5.79	3.67	4.44×10^{-3}
h_{0nd} (MJ/kg)	21.38	23.5	20.04
α	0.150	0.095	1.15×10^{-4}
Ω	1.23	3.80	1.15
L_s (m)	0.146	0.047	0.157

Table 5.1 Test conditions for reacting case. h_0 is the stagnation enthalpy, h_{0d} is the stagnation enthalpy due to dissociation, $h_{0nd} = h_0 - h_{0d}$, Ω is the Damkohler number, and L_s is the chemical length scale.

The supersonic state was used as the equivalent freestream. This process is unphysical and the Krek experimental conditions would not be expected to relax to this state. This process is only used to obtain a set of equilibrium conditions which should lead to similar post-shock conditions as the Krek experimenntal conditions. The process of "shocking" the flow raises the entropy and lowers the total pressure just as a physical shock does. This set of conditions will be referred to as the "shocked Krek conditions." Table 5.1 shows the Krek conditions and the calculated shock-processed equivalent equilibrium conditions.

The Mach numbers in this table are based on the frozen speed of sound. When the flow is processed by the shock, the density and velocity are relatively unaffected, but the temperature rises significantly due to the energy released by recombination. This results in a fairly low Mach number for a hypersonic flow, but because of the high temperature, we can expect to see significant real gas effects behind the bow shock.

The non-dimensional Damkohler number Ω is often used to characterize the reaction rate. It is formed from the ratio of the body length L to the characteristic reaction length in the shock layer L_s. This length scale is defined as

$$L_s = \frac{U_\infty}{(d\alpha/dt)_f}, \tag{5.4}$$

and

$$\Omega = \frac{L}{L_s} = \frac{L}{U_\infty}\left(\frac{d\alpha}{dt}\right)_f, \tag{5.5}$$

where U_∞ is the freestream velocity and $(d\alpha/dt)_f$ is the reaction rate evaluated from the conditions behind a frozen shock wave. $\Omega = 0$ is the frozen limit, where the body length is negligible compared to the chemical length scale, and any reactions occur far downstream of the body. $\Omega = \infty$ is the equilibrium limit, where the chemical length scale is negligible compared to the body, and reactions occur so quickly that the flow may be considered to be in local equilibrium everywhere.

For bluff body flows, the characteristic shock wave would be a normal shock; here it is appropriate to use an oblique shock. Following Macrossan and Pullin [34], the characteristic shock was assumed to be a 45° oblique shock, which is the sum of the cone half-angle and the angle of incidence. Ω is comparable for the Krek conditions and the shocked conditions, as is seen in Table 5.1 . However, the shocked conditions were not close enough to the test conditions due to the large increase (about 60%) in the temperature and pressure. The increase in temperature comes from the conversion of the excessive dissociation energy (stored in the high value of α) into thermal energy. The density is relatively unaffected by the equilibrium shock wave, so the pressure rise is due primarily to the increase in temperature. This led to the selection of the second set of conditions.

The second set of conditions was based on discarding the value of α from the Krek freestream, and calculating the equilibrium value of α for the temperature and density of Krek's freestream. One final condition is necessary to close the system, and the choice here was to maintain the same mass flux as the Krek freestream. Therefore, the density, velocity, and temperature were the same as Krek's conditions, but the dissociation energy was discarded. This set of conditions will be referred to as the "low-α Krek conditions." These conditions are shown in Table 5.1.

The lower degree of dissociation has several consequences. The speed of sound is lowered because α, and hence γ and the effective gas constant have decreased. This raises the Mach number slightly. Also, the pressure decreases slightly for the same reasons. The most significant effect is seen in the stagnation enthalpy h_0, because of the large drop in dissociation energy. The stagnation enthalpy can be decomposed into the enthalpy due to

dissociation h_{0d} and the remainder of the enthalpy $h_{0nd} = h_0 - h_{0d}$, where

$$h_{0d} = R_{N_2} \alpha \, \theta_d, \tag{5.6}$$

and

$$h_{0nd} = R_{N_2}(4 + \alpha)T + \frac{1}{2} u^2. \tag{5.7}$$

The table shows values of h_{0d} and h_{0nd}, and it can be seen that h_{0nd} is similar for the Krek conditions and the equilibrium Krek conditions.

Once again, a distinction should be made between a frozen computation and a computation with zero dissociation. When a frozen computation is performed, chemical reactions are turned off. This means that every cell will have the same α, but this is not equivalent to zero dissociation because a non-zero α will result in a different mixture gas constant and a different mixture ratio of specific heats. Hence either of the equilibrium conditions listed above can be run in frozen or equilibrium mode to obtain stepback solutions, and a frozen stepback solution may be used as an upstream boundary condition for a non-equilibrium run.

5.3 Computational Grids and Simulation Details

Both stepback and partial grid calculations were performed. The stepback grid resolution was $(2 \times 45 \times 100)$. The bulk of these calculations assumed an isothermal wall for comparison with Krek's results, although some adiabatic wall simulations were performed. It was found that having 12-15 cells in the adiabatic boundary layer was sufficient to resolve it, in contrast to the isothermal case, where 25-28 cells in the boundary layer were required for adequate resolution. The isothermal grids were stretched dramatically towards the cone surface, and the bow shock is rather coarsely resolved. However, our main present interest is in the cold-wall, near-surface flow, where the boundary layer is extremely thin, and the thickened shock will still provide appropriate edge conditions, as discussed below in Section 5.4. The grids are stretched using Roberts' first stretching function [58]. The stretching function is discussed in Appendix E. The stretching for the grids is specified in

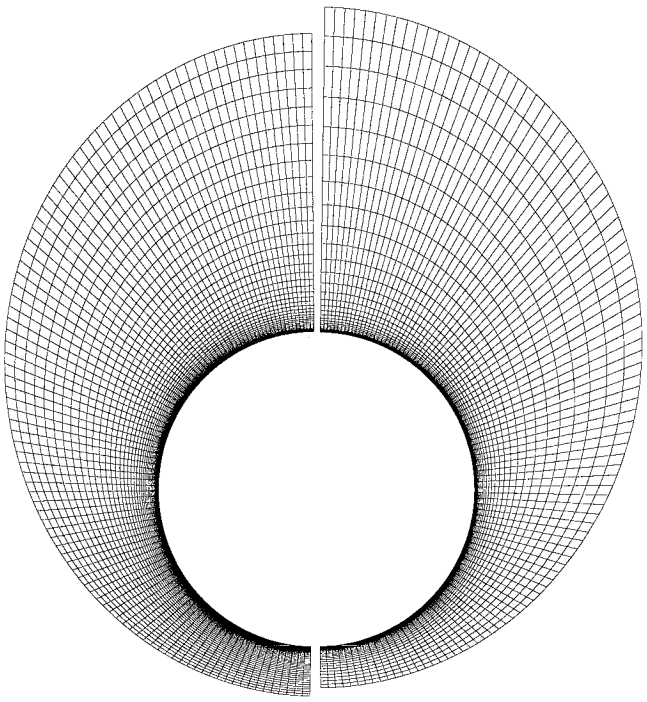

Figure 5.1 Grids for adiabatic and isothermal calculations.

terms of the included angle of the cell at the cone surface. For example, with a uniformly stretched grid with 100 cells that covered 10° from the cone's surface, the included angle of the first cell would be 0.1°. For the adiabatic grids, a typical included angle for the first cell was 0.01°, while for the isothermal grids, a typical included angle was 0.001°. Typical grids for adiabatic and isothermal calculations are shown in Figure 5.1.

Krek's heat transfer data was normalized by the heat transfer on the cone at zero incidence. These solutions were calculated using the stepback method on grids of resolution $(2 \times 100 \times 2)$.

The partial grid resolution was $(20 \times 45 \times 100)$. The partial grids extended from $r/L = 0.1$ to $r/L = 1.0$. The partial grids have the same resolution as the stepback grids at every downstream radius. Again, these grids are coarsely stretched, especially far from the cone on the leeward side. Accuracy in resolving the far field of the leeward flow, such as the vortical singularity and the outer part of the λ-shock, is sacrificed in favor of resolving the

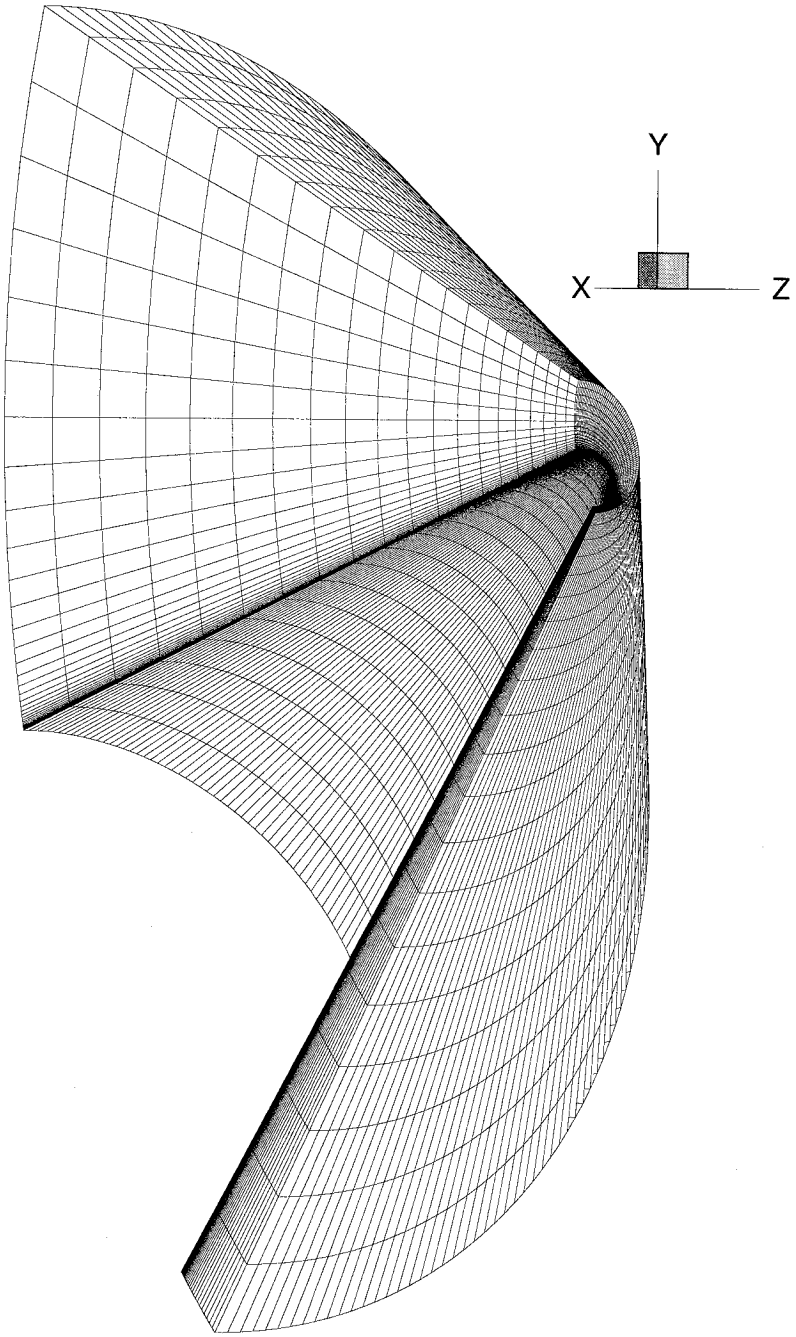

Figure 5.2 Isothermal partial grid ($20 \times 45 \times 100$), 15° cone at 30° incidence. Grid extends from $r/L = 0.1$ to $r/L = 1.0$. The freestream is moving in the positive x-direction, horizontal and into the page.

(r/L)	q_0 (MW/m^2)	
	Frozen	Equilibrium
0.10	11.740	11.460
0.34	6.257	6.102
0.46	5.357	5.214
0.58	4.749	4.622
0.69	4.339	4.222
0.81	3.932	3.825

Table 5.2 Zero incidence heat transfer q_0 for a 15° cone. Low-α Krek conditions, M=5.0. Stepback, EFMO. Isothermal wall at T_w = 300 K.

boundary layer. A typical isothermal partial grid is shown in Figure 5.2

5.4 Results and Discussion

This section compares the numerical findings with the experiments and discusses various aspects of the simulations. The zero incidence solutions are discussed. The windward shock standoff distance is calculated with an inviscid computation, and compared with previous simulations. The surface conditions are examined and compared with experiment for both stepback computations and partial grid computations. Finally, details of the leeward flow are discussed.

5.4.1 Zero Incidence Case

The zero incidence cone was computed with the stepback method at downstream stations (r/L) = 0.10, 0.34, 0.46, 0.58, 0.69, and 0.81. These stations correspond to Krek's stations, plus one calculation at the radius used to start the partial grid runs.

Figure 5.3 shows boundary layer profiles from the frozen stepback solutions, while Figure 5.4 shows profiles from the equilibrium stepback solutions. At the furthest downstream station, the boundary layer is still not self-similar. At zero incidence, the bow shock is not very strong, and the difference between the frozen and equilibrium profiles is not great. Although the frozen boundary layer is thicker than the equilibrium boundary layer, and the edge conditions are slightly different, the temperature gradient at the surface is almost

identical. Table 5.2 shows the computed heat transfer at the various stations for frozen and equilibrium calculations. The calulated heat transfer for the frozen case is only about 2–3% larger than for the equilibrium case. Figure 5.5 shows dissociation profiles for the equilibrium case.

Earlier, the extreme stretching required by the isothermal grids was mentioned. Figure 5.6 shows the results of two equilibrium stepback calulations, one with an isothermal wall at $T_w = 300\ K$, the other with an adiabatic wall. Both are based on the shocked Krek freestream, taken at r/L=0.69. Not only is the isothermal boundary layer about half as thick as the adiabatic one, but many more cells near the surface are required to resolve it. The isothermal boundary layer is considered unresolved if the temperature profile does not meet the prescribed temperature at the wall. Grid convergence is used to determine whether the adiabatic boundary layer is resolved. Although the isothermal criteria is less strict than grid convergence, the isothermal grids tend to require included angles in the first cell an order of magnitude smaller than the same grid for an adiabatic calculation. As mentioned above, it was found that having 12-15 cells in the adiabatic boundary layer was sufficient to resolve it, in contrast to the isothermal case, where 25-28 cells in the boundary layer were required for adequate resolution.

The result of this extreme stretching at the wall is that the bow shock is smeared over several degrees in θ, whereas the boundary layer is usually no more than 1° thick. The question may arise as to whether this poorly resolved bow shock will affect the quality of the solution in the boundary layer. Figure 5.7 shows the results from two frozen stepback calculations. Both are based on the low-α Krek conditions, at (r/L)=0.34. One grid is resolution $(2 \times 45 \times 2)$, while the other has twice as many cells away from the surface. The included angle of the first cell is the same, and near the surface the grids are very similar. Figure 5.7 shows both the shock layer and the boundary layer. From the temperature profiles, the shock wave is nearly 2.5° thick for the coarser grid, and about 1° thick for the finer grid. The closeup of the boundary layer shows that this has no effect on the profile there.

With a shock-capturing method, a shock wave will always smear over several cells. The boundary condition for this problem is applied at the surface. If the bow shock is underresolved, the effect will be to move the outer edge of the shock away from the body. As long as there is sufficient domain to capture the smeared shock as well as the freestream

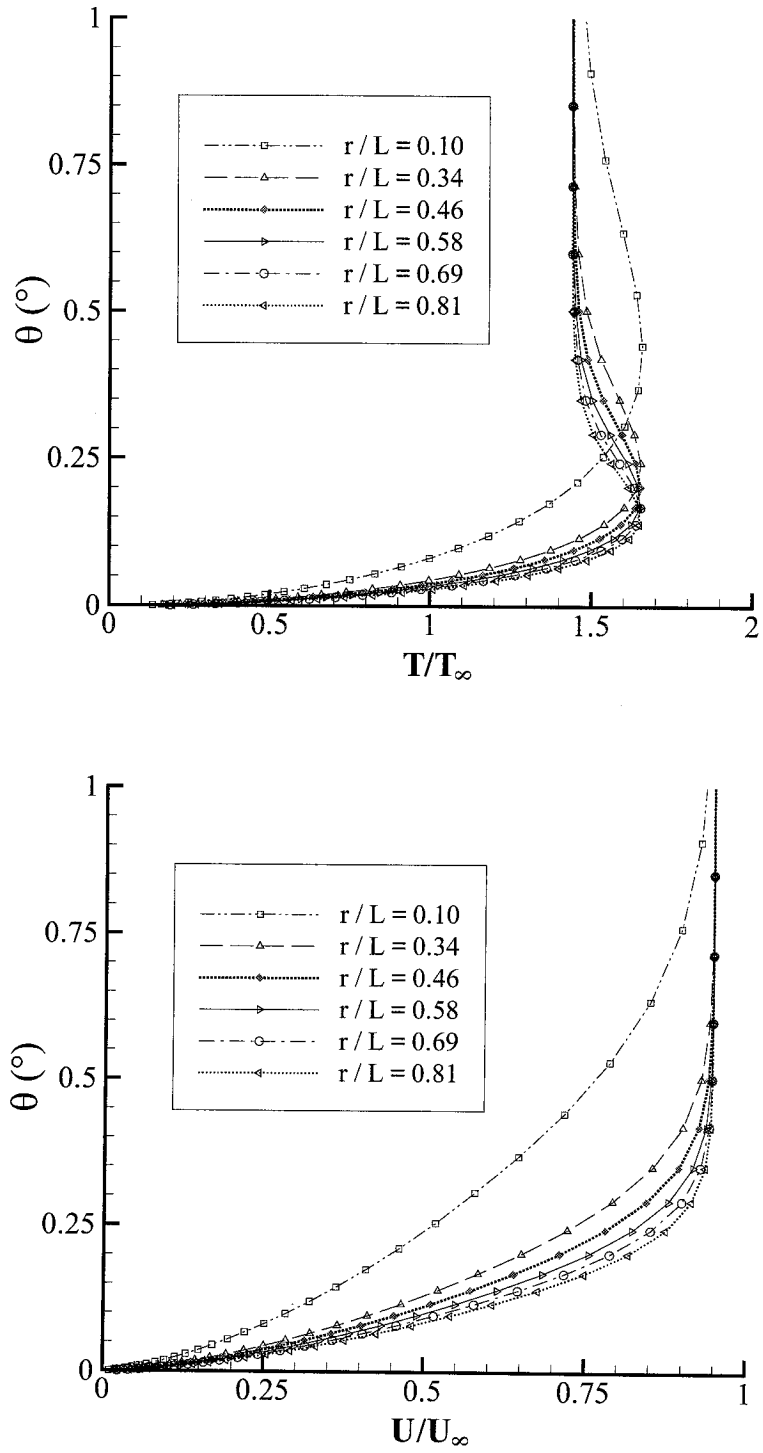

Figure 5.3 Frozen boundary layers for a 15° cone at zero incidence. Low-α Krek conditions, M=5.0. Stepback, EFMO. Isothermal wall at T_w = 300 K. T_∞ is the freestream temperature, U_∞ is the freestream velocity.

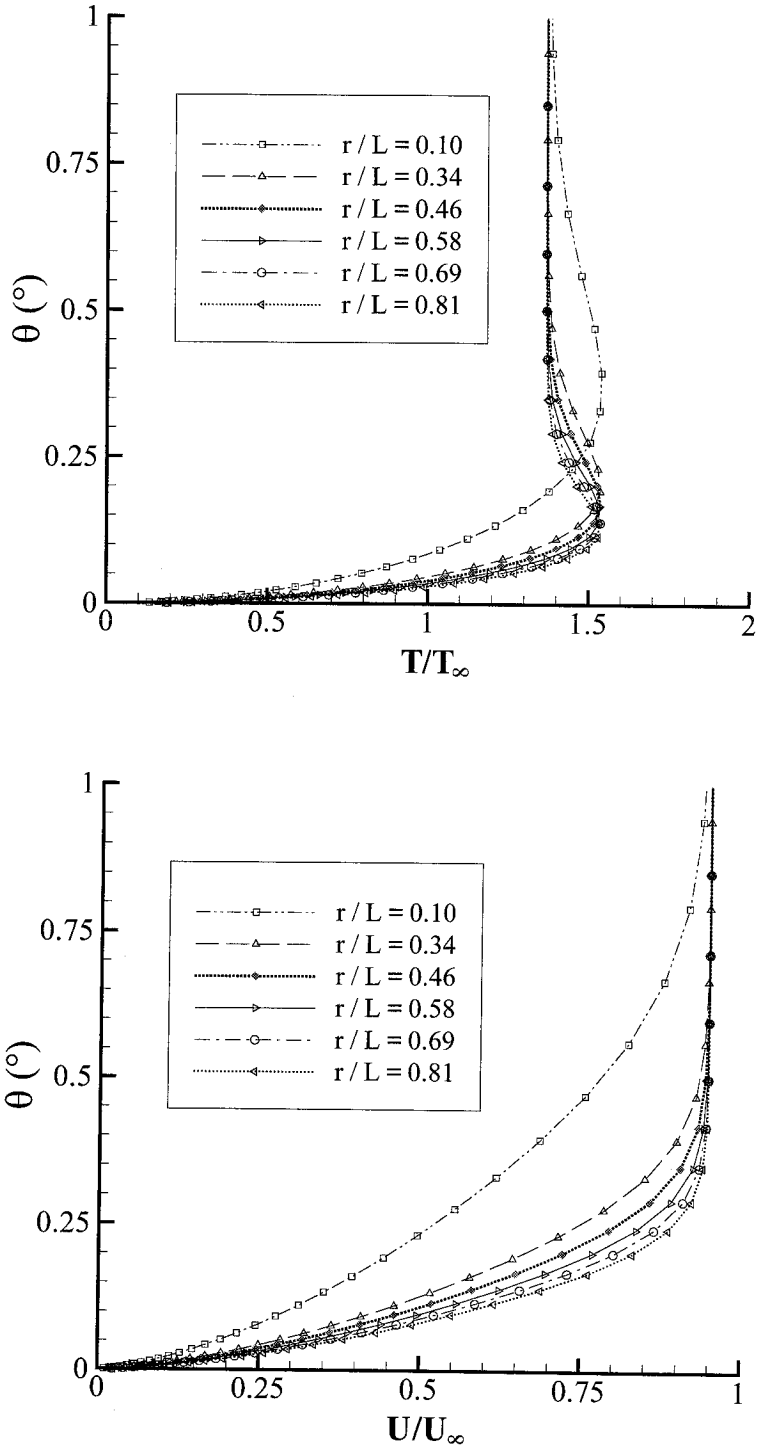

Figure 5.4 Equilibrium boundary layers for a 15° cone at zero incidence. Low-α Krek conditions, M=5.0. Stepback, EFMO. Isothermal wall at $T_w = 300$ K. T_∞ is the freestream temperature, U_∞ is the freestream velocity.

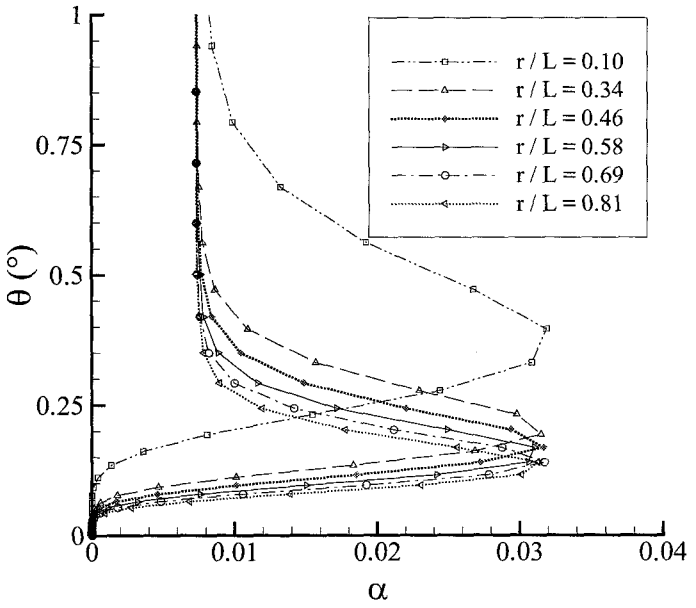

Figure 5.5 Equilibrium dissociation profile for a 15° cone at zero incidence. Low-α Krek conditions, M=5.0. Stepback, EFMO. Isothermal wall at T_w = 300 K. T_∞ is the freestream temperature, U_∞ is the freestream velocity.

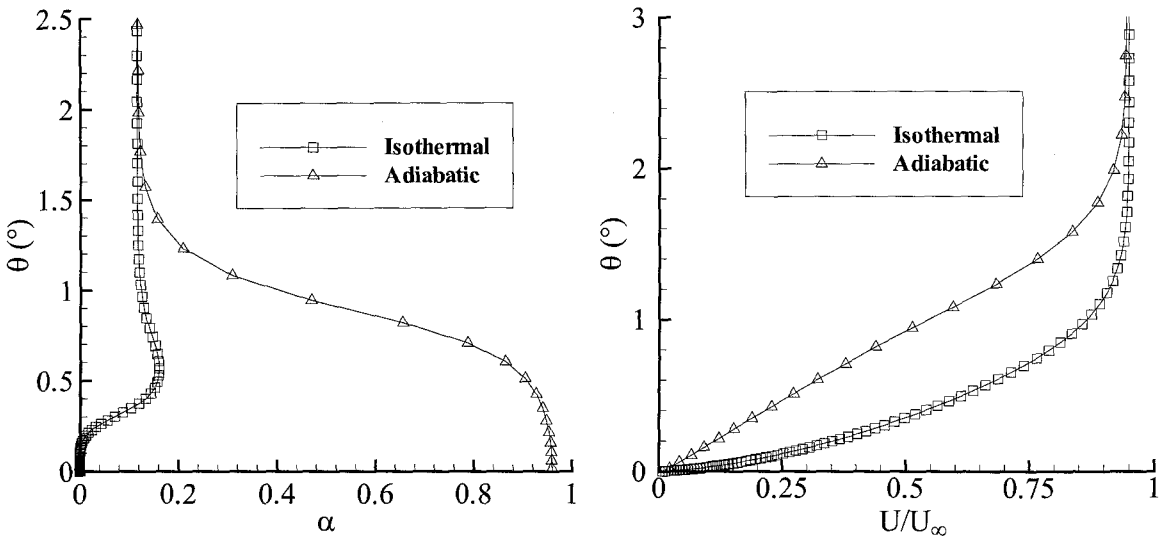

Figure 5.6 Comparison of adiabatic and isothermal boundary layers for a 15° cone at zero incidence. Shocked Krek conditions, M=3.6. Equilibrium stepback, EFMO. For the isothermal case, T_w = 300 K. U_∞ is the freestream velocity. $(r/L) = 0.69$.

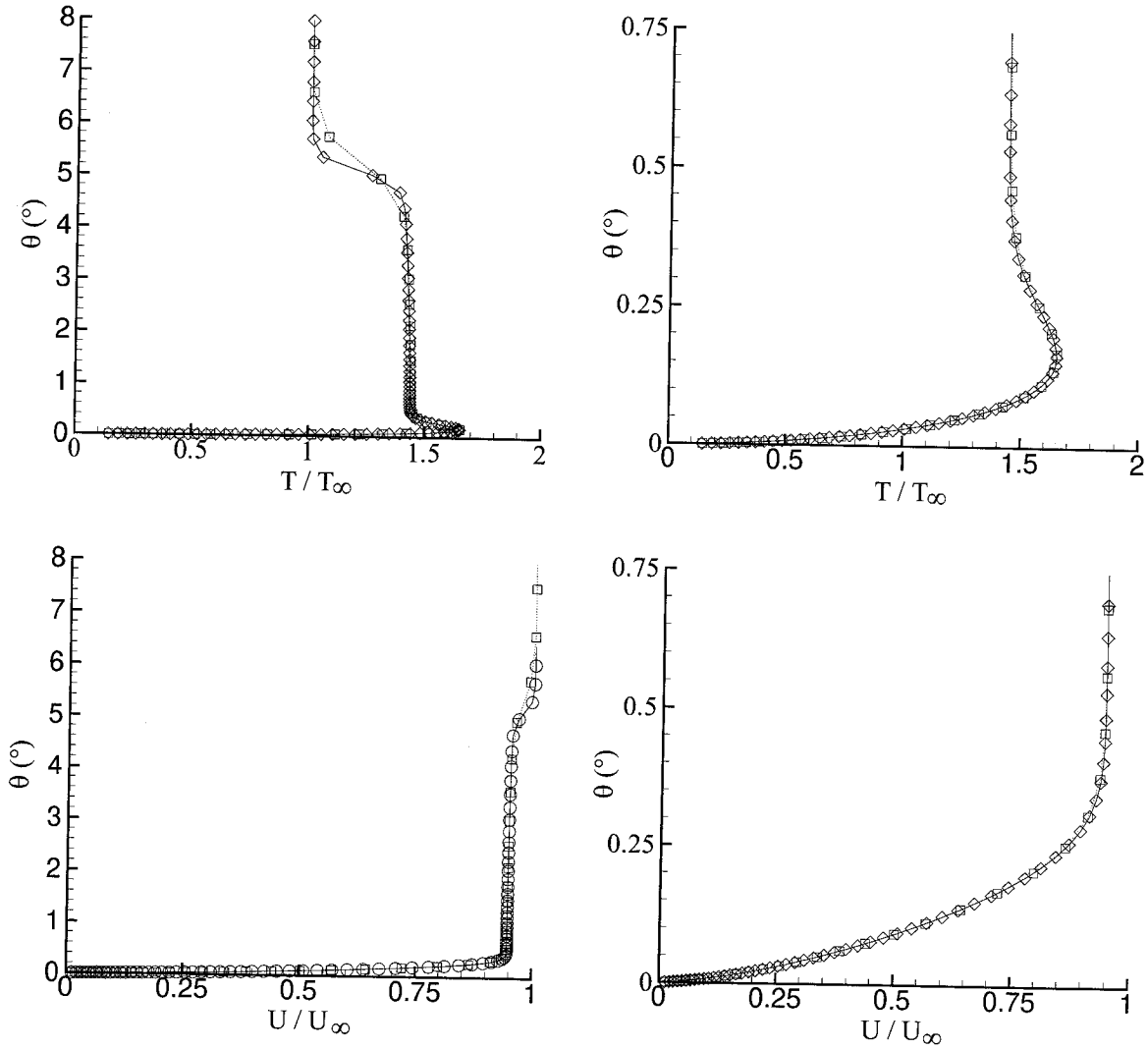

Figure 5.7 Effect of underresolved bow shock on boundary layer for a 15° cone at zero incidence. Low-α Krek conditions, M=5. Frozen, EFMO. Isothermal, T_w = 300 K. T_∞ is the freestream temperature, U_∞ is the freestream velocity. $(r/L) = 0.34$.

on the other side, the proper normal jump conditions will be met across it. An area of possible concern is the flow that passes tangentially through an excessively smeared shock. With the cone at incidence, the shock is smeared worst on the leeward side where it is the weakest. The flow that travels through this part of the shock ends up in the node on the plan of symmetry. The errors generated at the smeared bow shock should not be large enough to deflect this flow into the leeward shock-vortex system.

5.4.2 Stepback Profiles and Surface Conditions

Frozen and equilibrium stepback solutions were obtained for each station of Krek's data. An isothermal boundary condition was assumed, with T_w=300 K, since the test time is too short for a rise in the surface temperature to occur. Because of this boundary condition, the temperature gradients in the boundary layer are very large. Figure 5.8 shows temperature profiles along the windward plane of symmetry (ϕ=0°) at $(r/L) = 0.58$ for the frozen and equilibrium cases. Although the edge temperature for the frozen case is about twice that of the equilibrium case, the larger thickness of the frozen boundary layer and the huge temperature gradients there result in similar heat transfer between the frozen and equilibrium cases. In fact, in part of the boundary layer, the temperature is so low that all of the dissociated species recombine in the equilibrium case, although this is not allowed in the frozen case. Figure 5.8 also shows the degree of dissociation in the stagnation region for the equilibrium case.

The equilibrium chemistry has a pronounced effect on the windward shock standoff distance, which is consistent with similar results for inviscid cone flow [34]. Figure 5.9 shows a comparison of Mach number contours for the same Reynolds number, where $(r/L) = 0.10$, for frozen and equilibrium flows. The chemistry also plays a role in the location of separation. The equilibrium flow remains attached to the cone longer, and hence the leeward vortex associated with that separation is smaller in equilibrium. Figure 5.10 shows a closeup of the leeward vortex for frozen flow and for equilibrium flow. It can also be seen that the shape and size of the vortices is slightly different. This is also consistent with invisicid results [34], although the separation mechanisms are somewhat different.

Figure 5.11 shows comparisons of the heat transfer from frozen stepback and equilibrium stepback solutions with Krek's data for the four downstream stations. As discussed

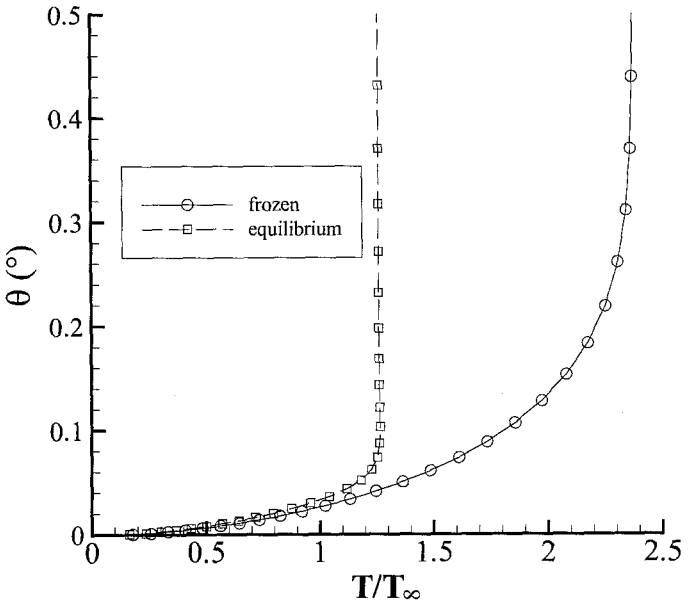

Temperature profiles (frozen and equilibrium)

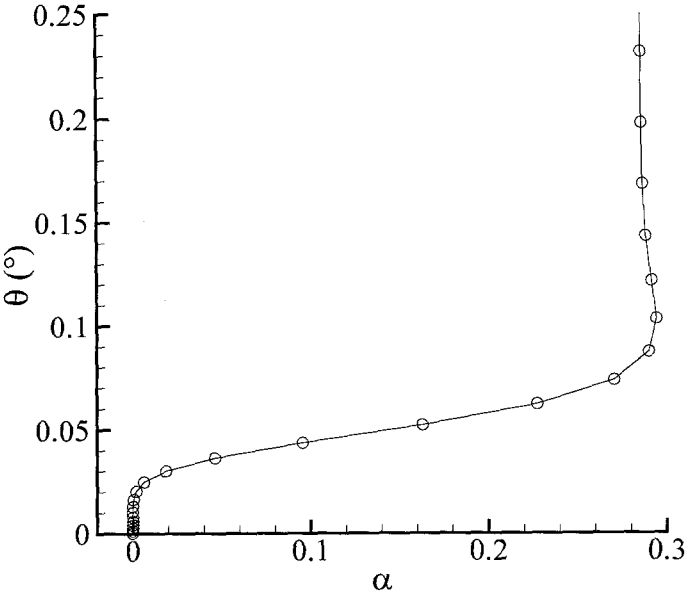

Dissociation profile (equilibrium)

Figure 5.8 Profiles along the windward plane of symmetry for a 15° cone at 30° incidence. Shocked Krek conditions, M=3.6. θ is the angle from the cone surface. Frozen and equilibrium stepback, EFMO. Isothermal wall, T_w=300 K. ($r/L = 0.58$.

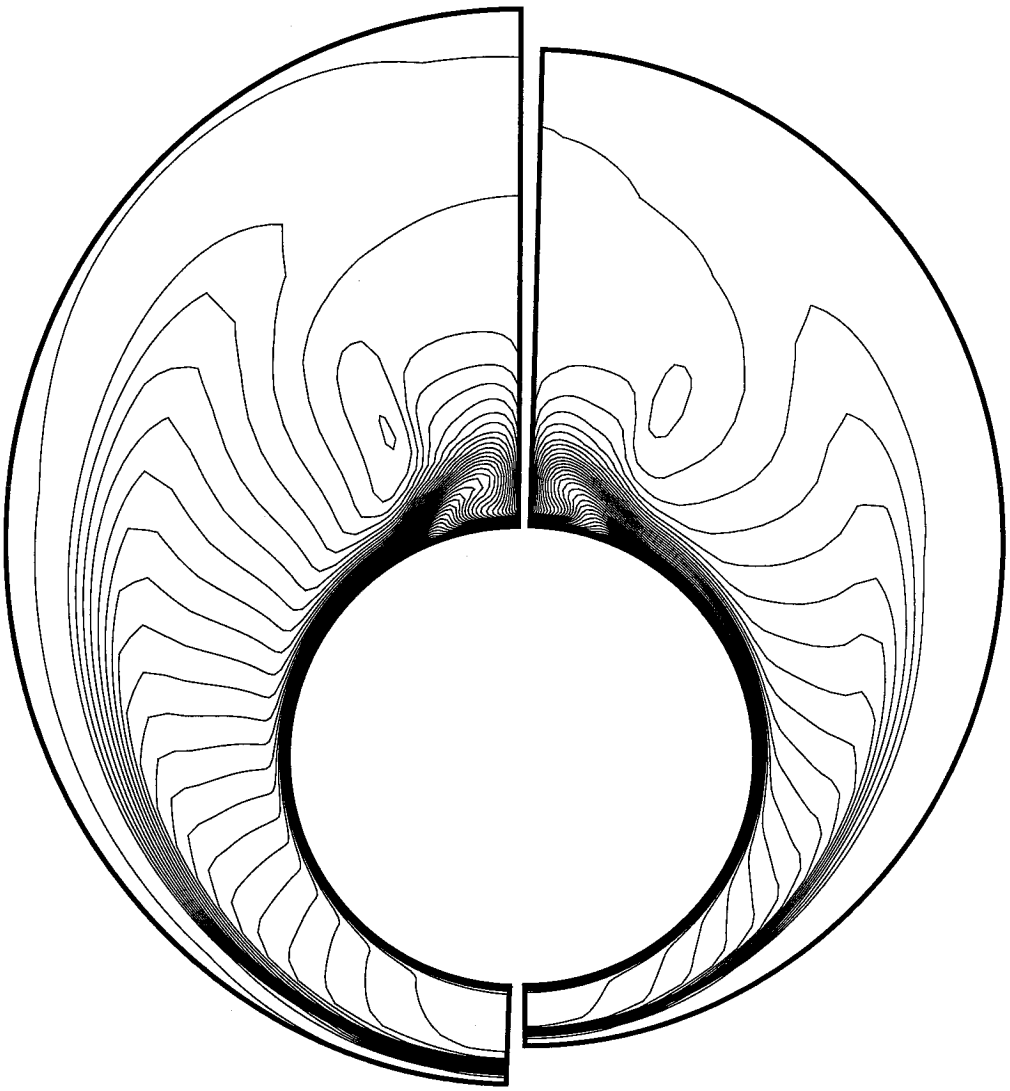

Figure 5.9 Frozen and equilibrium Mach number contours for a 15° cone at 30° incidence. Shocked Krek conditions, M=3.6. Stepback, EFMO. Isothermal, T_w=300 K. $(r/L) = 0.58$.

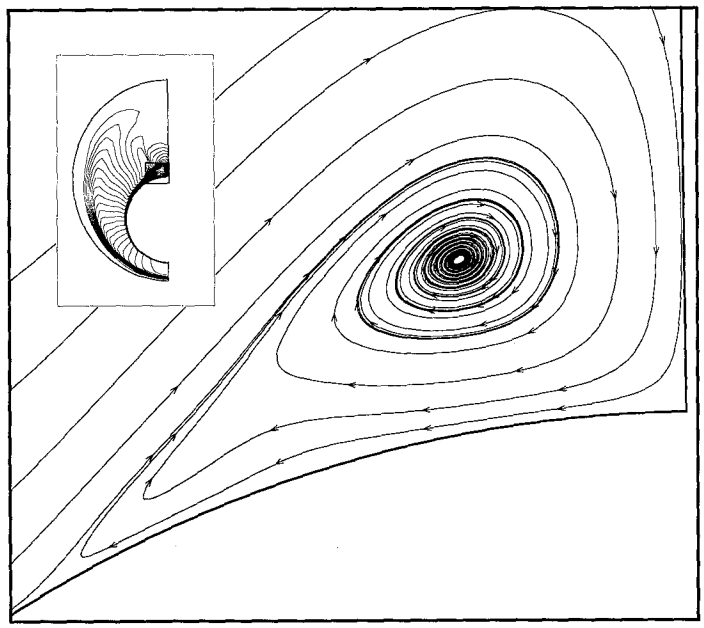

Frozen

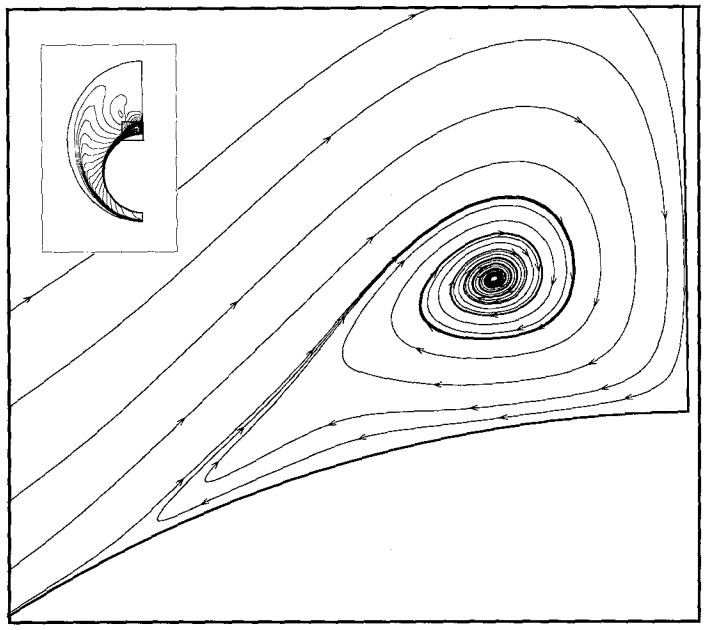

Equilibrium

Figure 5.10 Leeward crossflow streamlines for a 15° cone at 30° incidence. Shocked Krek conditions, M=3.6. Stepback, EFMO. Isothermal, T_w=300 K. $(r/L) = 0.34$. Inset shows computational domain. The box in the inset indicates the region shown in the plot.

in Section 5.1, two types of instruments were used to measure the heat transfer. The intrumentation changes at $\phi = 90°$, explaining the discontinuity in measured heat transfer there. The data on the leeward side of the flow is more accurate. The heat transfer data was normalized by the zero incidence heat transfer corresponding to the appropriate calculation (frozen or equilibrium).

Figure 5.11 shows typical behavior of the computed heat transfer results. The heat transfer is large at the windward plane and drops as the flow expands around the cone due to the cooling effect of the cold isothermal boundary layer. The heat transfer drops rapidly just upstream of separation (where the heat transfer is a minimum), and rises dramatically in the separated region, almost reaching the same levels as at the windward plane. On the windward side of the cone, the frozen calculation has higher heat transfer, while on the leeward side, the frozen heat transfer is lower than in the equilibrium case. The equilibrium case always separates later than the frozen case.

Figure 5.12 shows comparisons of the surface pressure from the frozen stepback and equilibrium stepback solutions with Krek's data. The pressure is highest at the windward plane, reduces as the flow expands around the cone, and reaches a minimum upstream of separation. Separation is indicated on the pressure plots by the plateau just after the minimum. The pressure increases at the leeward plane.

The calculations tend to give higher pressures than the experiment, but the separation point (taken as the location of minimum q_0) agrees well with the experimental results. The discrepancy in the magnitude of pressure may be due to the transducers used in the experiment. There is significant scatter in Krek's zero incidence pressure measurements, and very large error bars for some of the transducers. All of Krek's zero incidence pressure measurements for this test condition underestimate the computed surface pressure when compared with a Taylor-MacColl solution. At all test conditions Krek used, the transducers at (r/L)=0.58 and (r/L)=0.69 produced significantly lower readings than the other transducers, sometimes reading 60% less than the theoretical prediction. These stations are the ones with the poorest agreement between the simulation and the experiment.

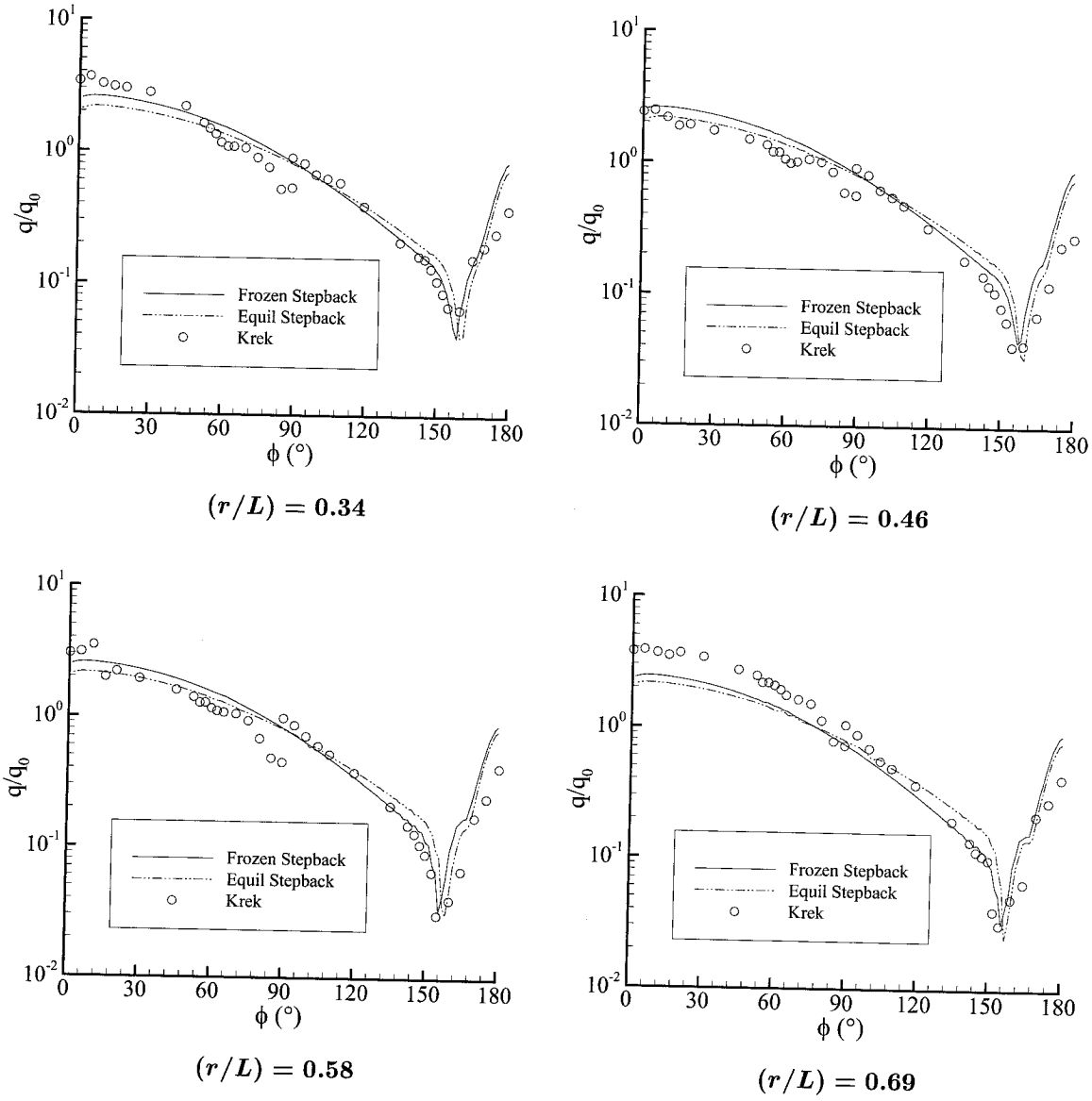

Figure 5.11 Frozen and equilibrium stepback heat transfer for a 15° cone at 30° incidence. Low-α Krek conditions, M=5. EFMO. Isothermal, T_w=300 K. q_0 is the heat transfer at the same station on the zero incidence cone.

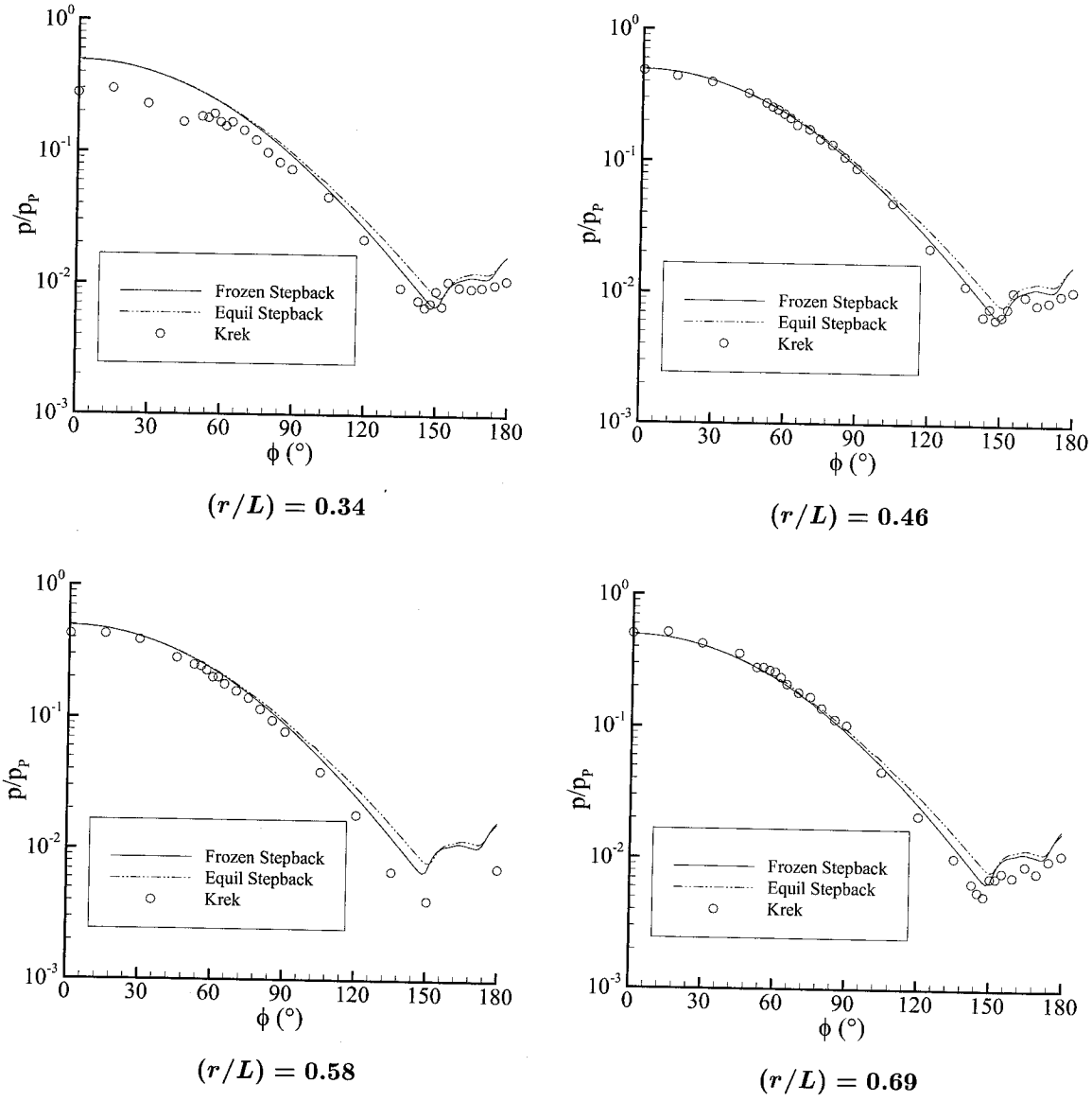

Figure 5.12 **Frozen and equilibrium stepback surface pressure for a 15° cone at 30° incidence. Low-α Krek conditions, M=5. EFMO. Isothermal, T_w=300 K. p_P is the pitot pressure in the freestream.**

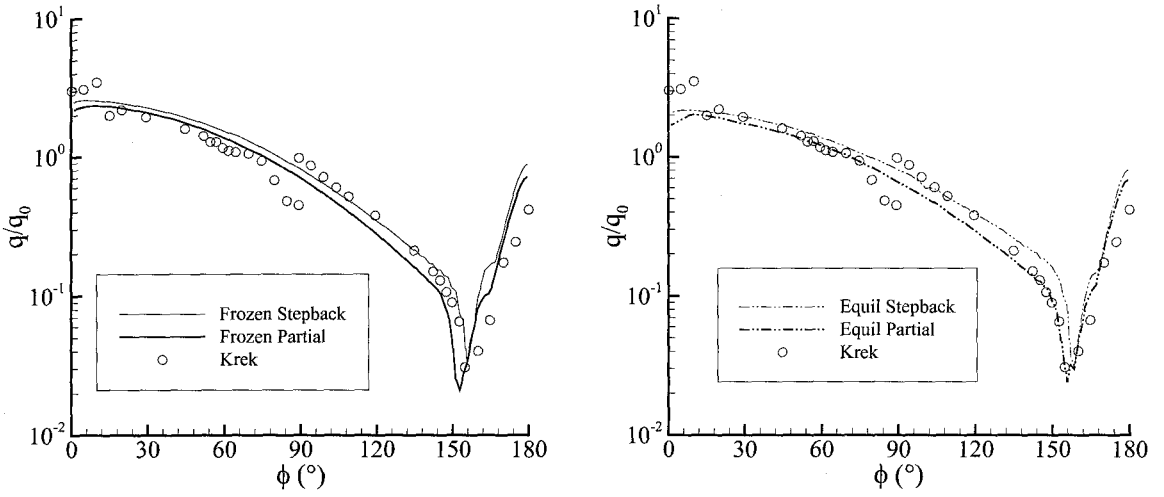

Figure 5.13 Stepback and partial grid heat transfer for a 15° cone at 30° incidence. Low-α Krek conditions, M=5. EFMO. Isothermal, T_w=300 K. q_0 is the heat transfer at the same station on the zero incidence cone.

5.4.3 Partial Grid Profiles and Surface Conditions

Frozen, non-equilibrium, and equilibrium partial grid calculations were performed for both the shocked conditions and the low-α conditions. Figure 5.13 shows a comparison of heat transfer for stepback and partial grid calculations at (r/L)=0.58. The frozen results are on the left, and the equilibrium are on the right. The partial grid solutions tend to exhibit lower heat transfer than the corresponding stepback solution, and separation occurs slightly earlier.

Similarly, Figure 5.14 shows a comparison of surface pressure for the frozen and equilibrium cases at the same station. Again, the frozen case is on the left, and the equilibrium case on the right. The pressures agree up to the point of separation. The partial grid results separate earlier, and have larger pressures in the separated region.

For the non-equilibrium case, the heat transfer was normalized by the frozen zero incidence heat transfer. Figure 5.15 shows the differences in heat transfer between the frozen, non-equilibrium, and equilibrium partial grid solutions at the various stations. The same observations that hold for the stepback cases hold here. The frozen heat transfer is higher than the equilibrium case on the windward side and lower on the leeward side, and the

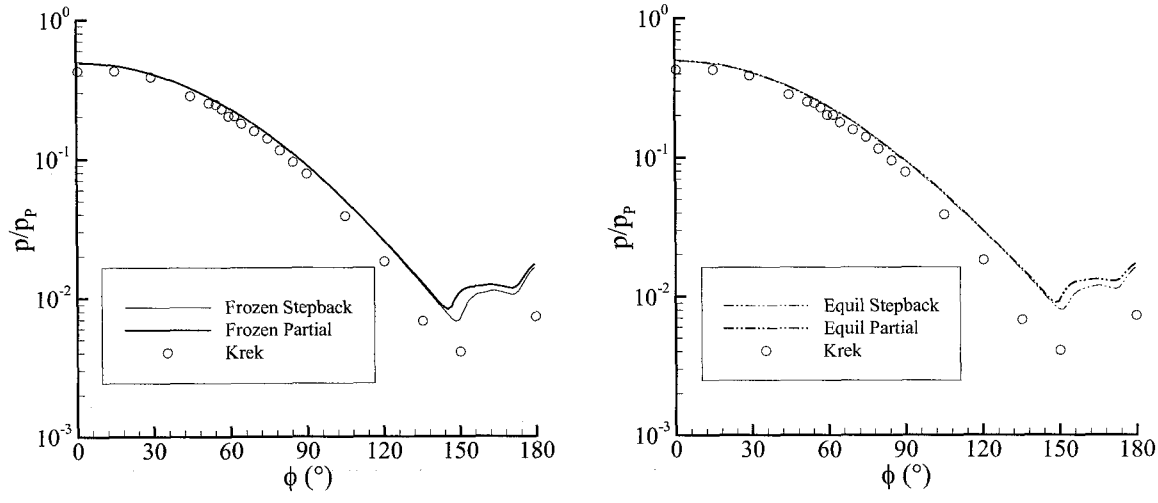

Figure 5.14 Stepback and partial grid surface pressure for a 15° cone at 30° incidence. Low-α Krek conditions, M=5. EFMO. Isothermal, T_w=300 K. p_P is the pitot pressure in the freestream.

frozen solution separates first. The non-equilibrium case is more interesting. On the windward side of the cone, the non-equilibrium heat transfer is lower than either the frozen or equilibrium cases. The non-equilibrium case separates at the same location or slightly earlier than the frozen case. The fact that the non-equilibrium solution is not bracketed by the frozen and equilibrium solutions is consistent with previous observations [34].

Figure 5.16 shows the differences in surface pressure between the frozen, non-equilibrium, and equilibrium partial grid solutions at the various stations. The non-equilibrium solution has the same pressure as the frozen solution upstream of the separation point, although the non-equilibrium pressure in the separated region is slightly lower.

Figure 5.17 shows how the dimensional heat transfer varies with distance from the tip for stepback and partial grid calculations. The heat transfer at the windward plane of symmetry $q_{\phi=0}$ is plotted versus Re_x. The partial grid results predict lower heat transfer than the stepback results. The non-equilibrium solution is not bracketed by the frozen and equilibrium solutions, and adjusts from the frozen stepback solution over five cells. At large Reynolds numbers, the computed heat transfer begins to decrease more rapidly. The boundary condition applied at the downstream end of the partial grid is a no-gradient condition. This is not correct for this problem, and causes errors in the last few downstream

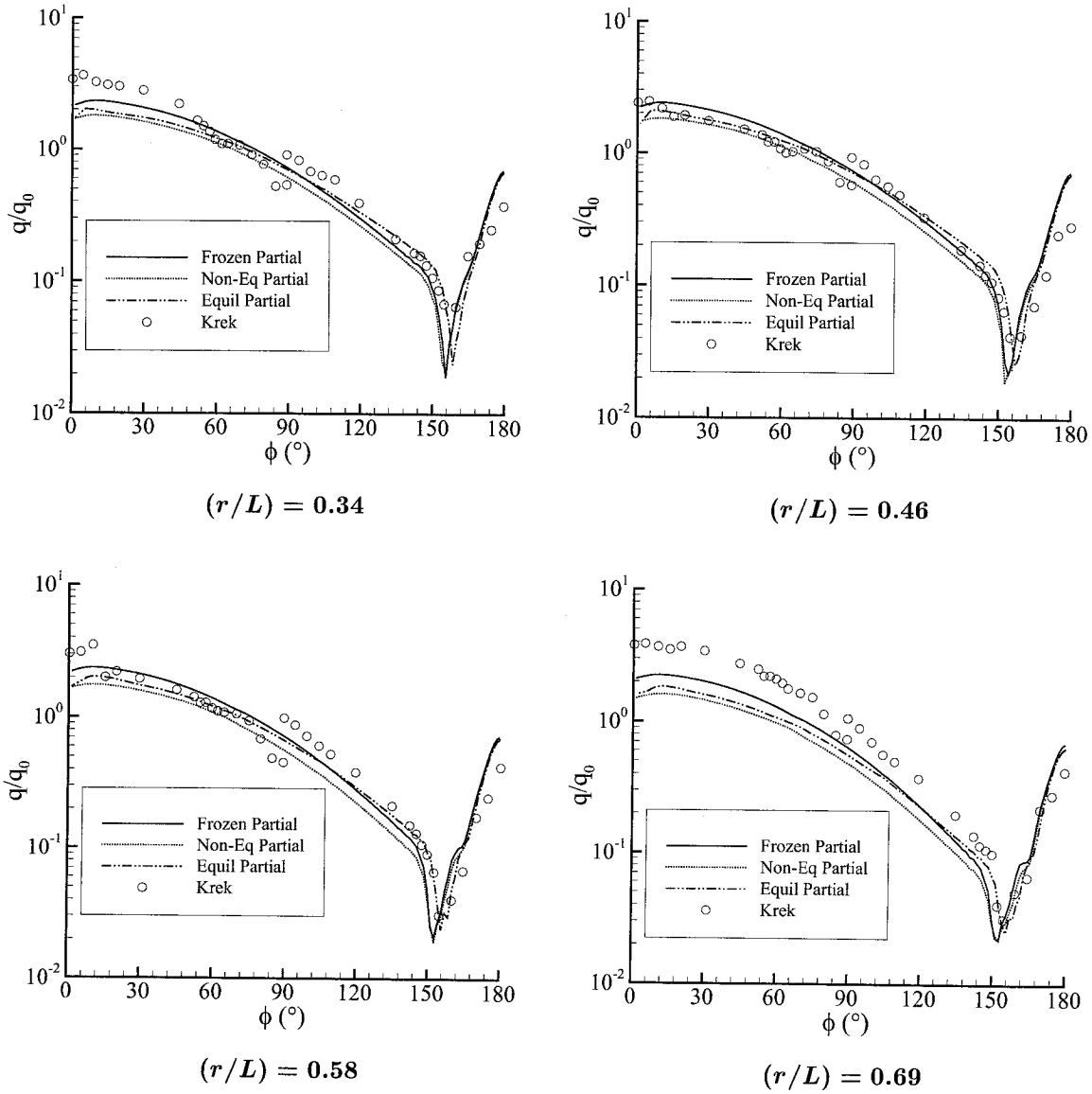

Figure 5.15 **Frozen, non-equilibrium, and equilibrium partial grid heat transfer for a 15° cone at 30° incidence. Low-α Krek conditions, M=5. EFMO. Isothermal, T_w=300 K. q_0 is the heat transfer at the same station on the zero incidence cone.**

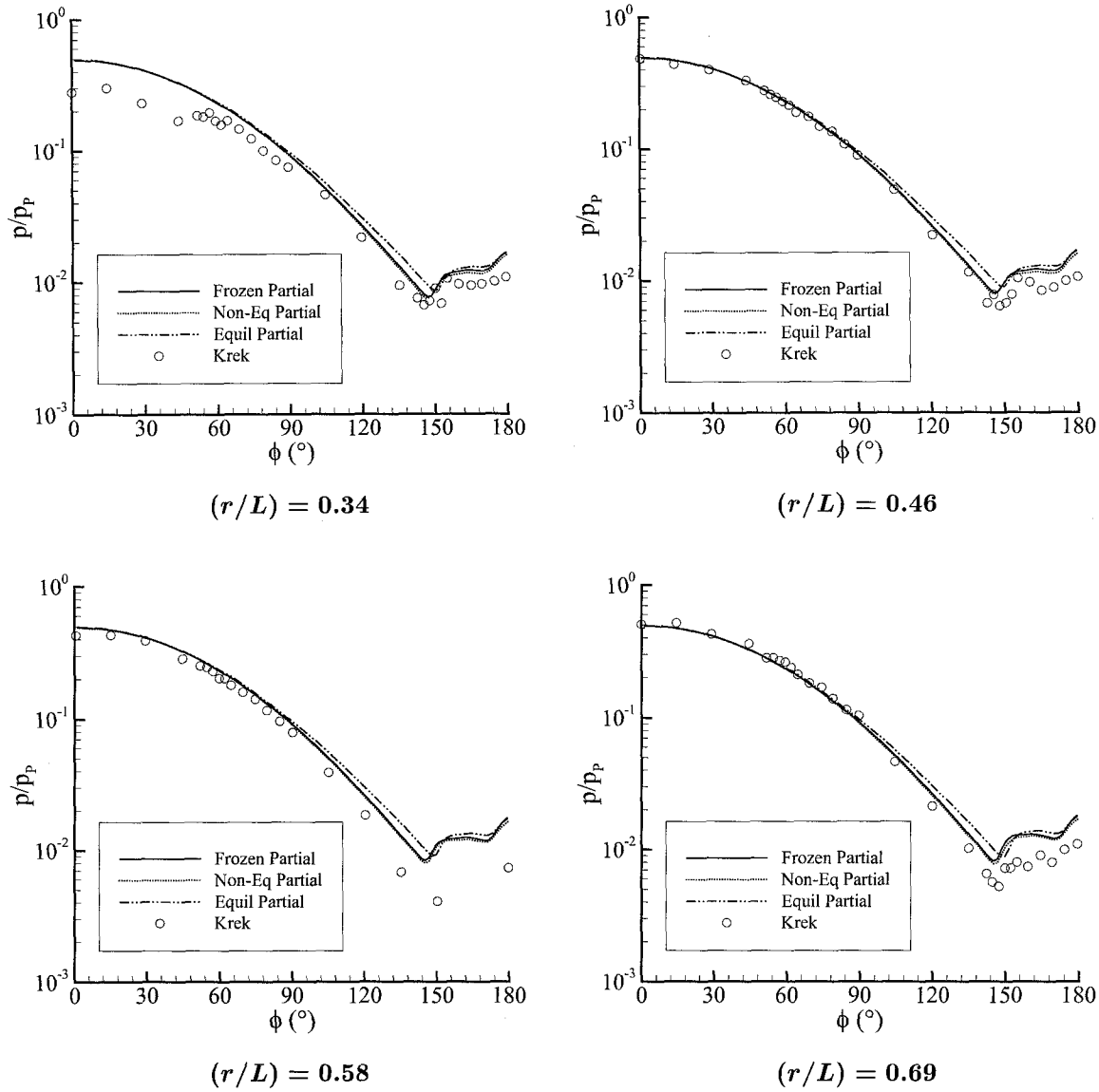

Figure 5.16 Frozen, non-equilibrium, and equilibrium partial grid surface pressure for a 15° cone at 30° incidence. Low-α Krek conditions, M=5. EFMO. Isothermal, T_w=300 K. p_P is the pitot pressure in the freestream.

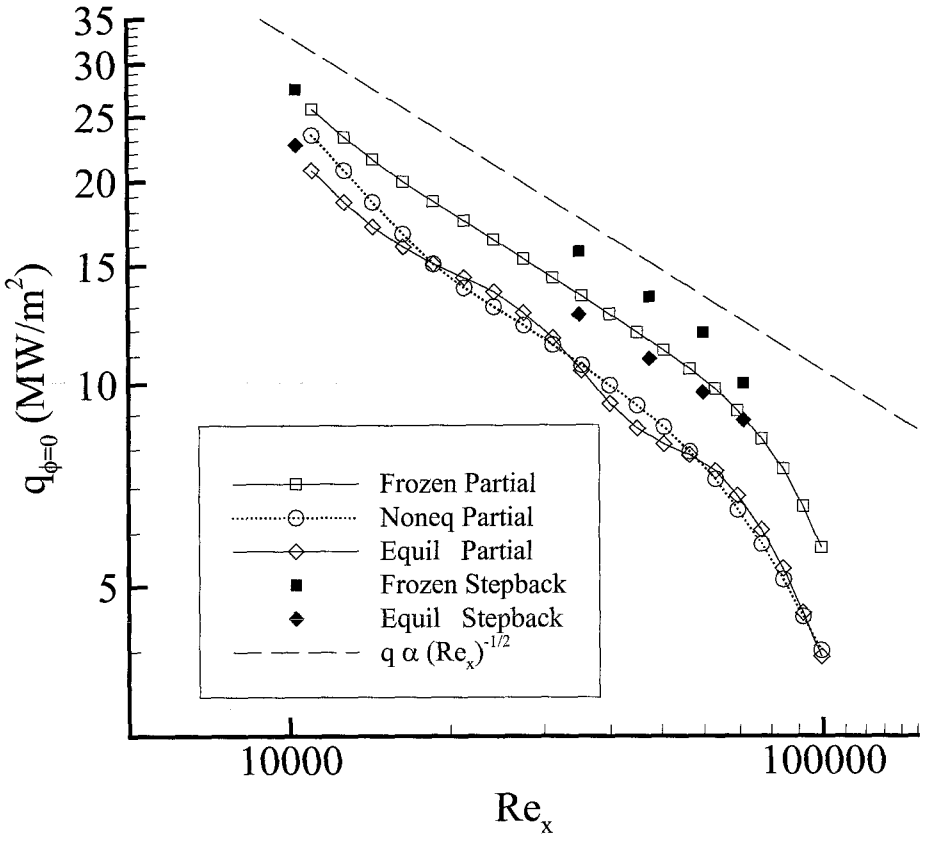

Figure 5.17 Variation of ϕ=0° heat transfer with Re_x, 15° cone at 30° incidence. Low-α Krek conditions, M=5. EFMO. Isothermal, T_w=300 K. The dashed line q $\propto$ $(Re_x)^{-1/2}$ indicates the slope of the line predicted by laminar flat plate theory.

cells. The rapid drop in heat transfer at the end of the cone is most likely due to these errors than to any physical basis. By using more downstream cells, the domain of influence of these errors could be minimized.

Laminar flat plate theory predicts that $q \propto Re_x^{-1/2}$ [59]. On the log-log plot of Figure 5.17, this corresponds to a line whose slope is -1/2. A line with this slope is included in the figure for reference. The stepback solutions agree well with the theoretical trend, although the slope of the stepback line is larger (i.e., less negative) than the plotted line. For intermediate Reynolds numbers, the frozen and non-equilibrium partial grid solutions agree very well with the laminar flat plate slope. The equilibrium windward heat transfer oscillates about the laminar flat plate slope.

5.4.4 Windward Shock Standoff Distance

One of the objectives of this study was to measure the windward shock standoff distance and see how it is affected by chemistry. However, as discussed above, the large stretching necessary for the isothermal calculations smeared the bow shock excessively. The shock standoff distance is essentially an inviscid phenomenon, with the boundary layer thickness displacing the shock slightly. Hypersonic isothermal boundary layers are very thin, and can be neglected in the measurement of the bow shock standoff distance. This will be shown below.

Two inviscid non-equilibrium partial grid calculations were performed, one for the shocked conditions and one for the low-α conditions. Both grids had a resolution of $(20 \times 45 \times 100)$, and extended from $(r/L) = 0.10$ to $(r/L) = 1$. The inviscid partial grid is shown in Figure 5.18.

Figure 5.19 shows a comparison of Mach contours for two non-equilibrium partial grid calculations, one inviscid and one viscous with an isothermal boundary condition. Contours are shown at two radii, $(r/L) = 0.18$ and $(r/L) = 0.69$, and the agreement is excellent at both stations. Both grids have the same resolution of $(20 \times 45 \times 100)$, but the stretchings are quite different. The included angle of the first cell for the inviscid grid was $0.15°$, while for the viscous grid, the included angle was $0.001°$. The position of the inviscid bow shock agrees with the viscous bow shock, and the inviscid bow shock is clearly resolved over a much thinner width than the bow shock from the viscous grid. As discussed previously, when the bow shock is underresolved, the outer edge of the shock moves away from the body. But the inside edge of the bow for the two simulations agrees, producing the same shock layer thickness. The Mach contours outside the boundary layer agree very well up to $\phi \approx 135°$, and the displacement thickness of the boundary layer is negligible. The inviscid solution is clearly adequate for measuring the shock standoff distance.

Figure 5.19 also shows the fundamental differences between the leeward shock-vortex systems for the two cases. With the inviscid case, the separation point is closer to the leeward plane of symmetry, and consequently the vortex is smaller. The leeward shock is not a λ-shock, but it is a single shock. With the viscous case, the boundary layer has grown fairly thick by the time the flow separates. The characteristic λ-shock is faintly seen, although it is not as crisp as the inviscid leeward shock. The shock standoff distance Δ was

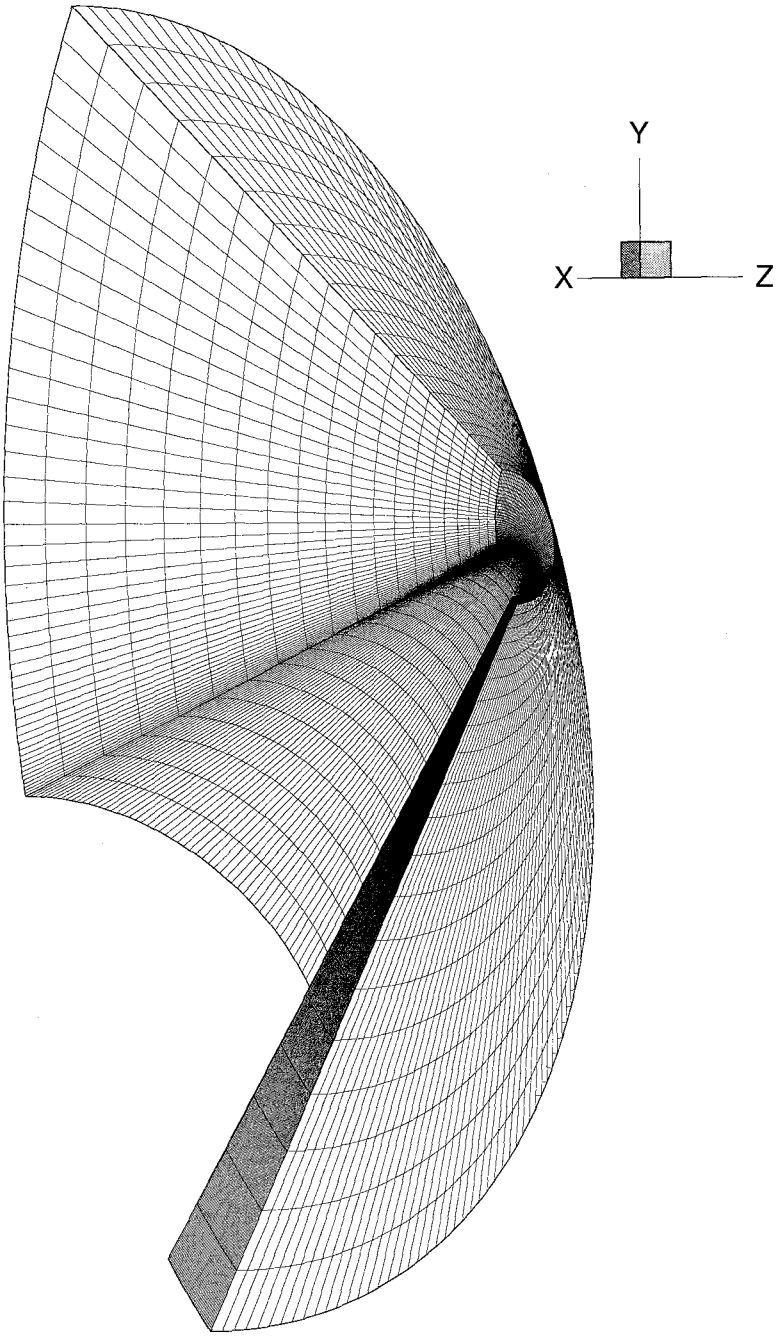

Figure 5.18 Inviscid partial grid ($20\times45\times100$), 15° cone at 30° incidence. Grid extends from $r/L = 0.1$ to $r/L = 1.0$. The freestream is moving in the positive x-direction, horizontal and into the page.

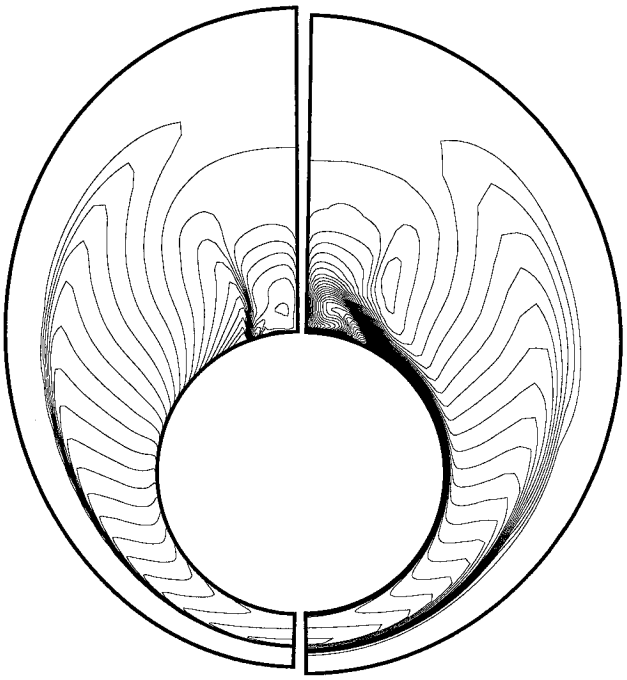

$(r/L) = 0.18$

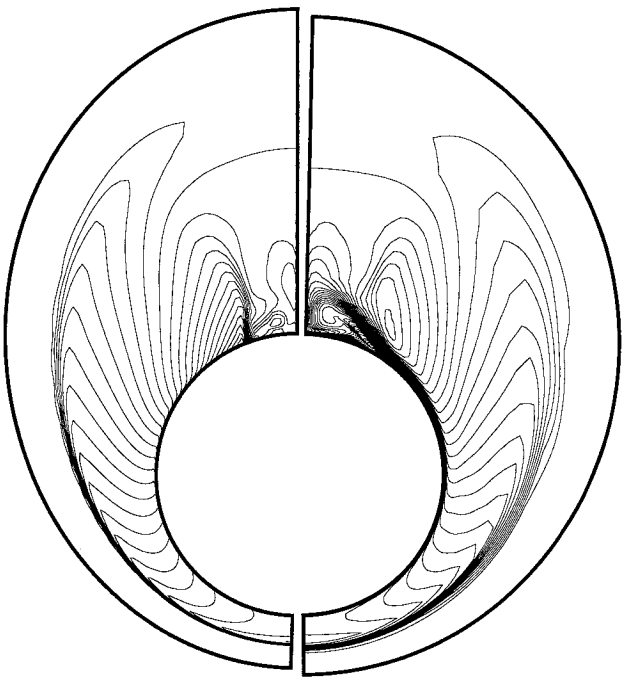

$(r/L) = 0.69$

Figure 5.19 Mach contours comparing inviscid (left) and viscous (right) partial grid calculations at downstream distance indicated. 15° cone at 30° incidence. Shocked Krek conditions, M=3.6. Non-equilibrium, EFMO. Isothermal, T_w=300 K.

	Macrossan & Pullin conditions	Shocked conditions	Low-α conditions
M	5.00	3.60	4.99
ρ (g/m^3)	9.998	9.53	9.33
u (m/s)	5954	5565	5683
T (K)	3581	5381	3273
p (kPa)	10.64	16.67	9.071
h_0 (MJ/kg)	21.99	27.17	20.04
h_{0d} (MJ/kg)	1.66×10^{-2}	3.67	4.44×10^{-3}
h_{0nd} (MJ/kg)	21.97	23.5	20.04
α	4.93×10^{-4}	0.095	1.15×10^{-4}
Ω	2.38	3.80	1.15
L_s (m)	0.076	0.047	0.157

Table 5.3 Equivalent equilibrium conditions used for shock standoff measurements. h_0 is the stagnation enthalpy, h_{0d} is the stagnation enthalpy due to dissociation, $h_{0nd} = h_0 - h_{0d}$, Ω is the Damkohler number, and L_s is the chemical length scale.

determined by the point of maximum temperature gradient. This was measured for each downstream cell, and normalized for comparison with similar results from Macrossan and Pullin [34].

The freestream used by Macrossan and Pullin was also an equilibrium state based on the Krek experimental conditions. Macrossan and Pullin also investigated several freestreams; the one used here was labelled the H22 freestream [34]. The H22 conditions are very similar to the low-α Krek conditions used here, but have some important differences. Table 5.3 compares the various equilibrium freestreams. The Macrossan and Pullin freestream (hereafter referred to as the M & P freestream) is about 5% faster, 7% more dense, and 10% hotter than the low-α state, resulting in a difference of about 10% in the stagnation enthalpy. Because the equilibrium degree of dissociation is very sensitive to changes in temperature and density when $\alpha \ll 1$, the degree of dissociation of the M & P freestream is more than 4 times that of the low-α Krek conditions. The higher α, combined with the larger temperature and density, result in a higher reaction rate behind the bow shock, so the Damkohler number of the M & P conditions is more than twice the low-α Damkohler number.

Macrossan and Pullin's results used two normalizations. The first followed Hornung [60],

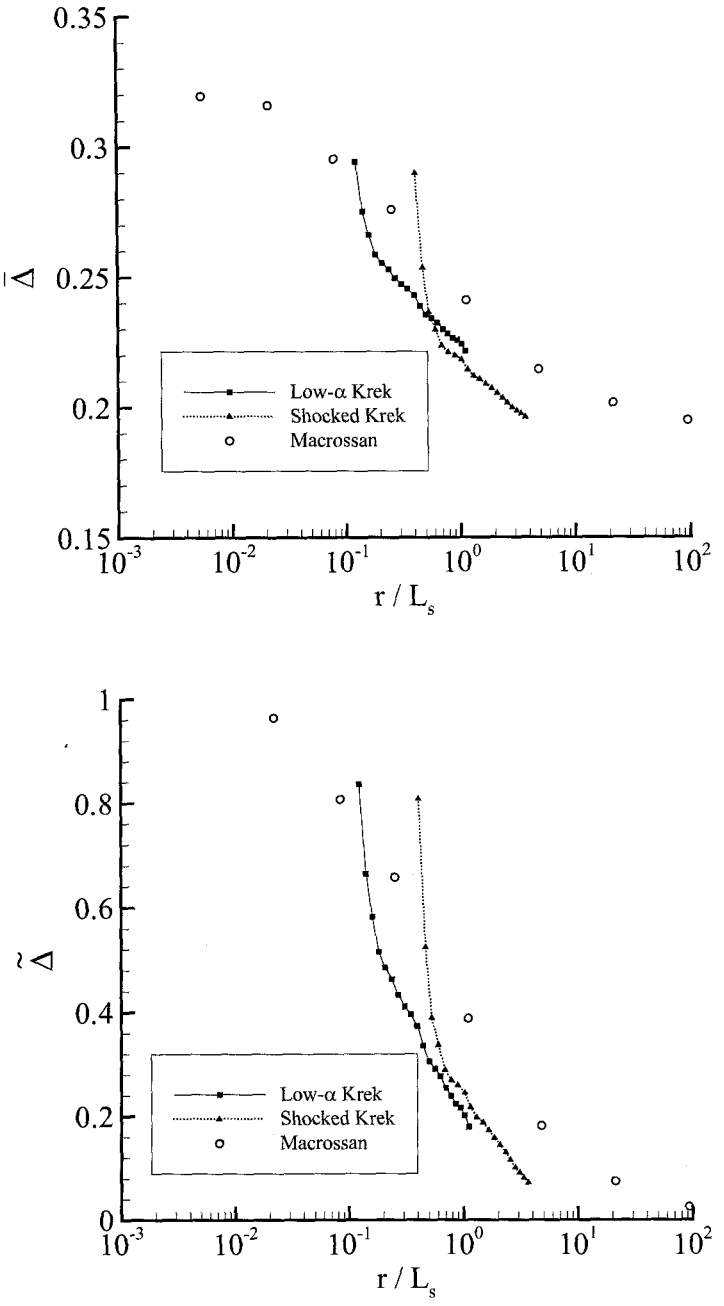

Figure 5.20 Normalized windward bow shock standoff distance vs. (r/L_s). $\bar{\Delta} = (\Delta/r)(\rho_s/\rho_\infty)$, and $\tilde{\Delta} = (\Delta - \Delta_e)/(\Delta_f - \Delta_e)$. Non-equilibrium inviscid partial grids, EFMO. ρ_s/ρ_∞ is the density ratio across the frozen oblique shock, Δ_f is the standoff distance at the frozen limit, Δ_e is the standoff distance at the equilibrium limit. The plot shows the data at each downstream cell. The partial grid solution starts from a frozen stepback solution. The large gradients in the first few cells correspond to the partial grid solution recovering from the frozen stepback boundary condition.

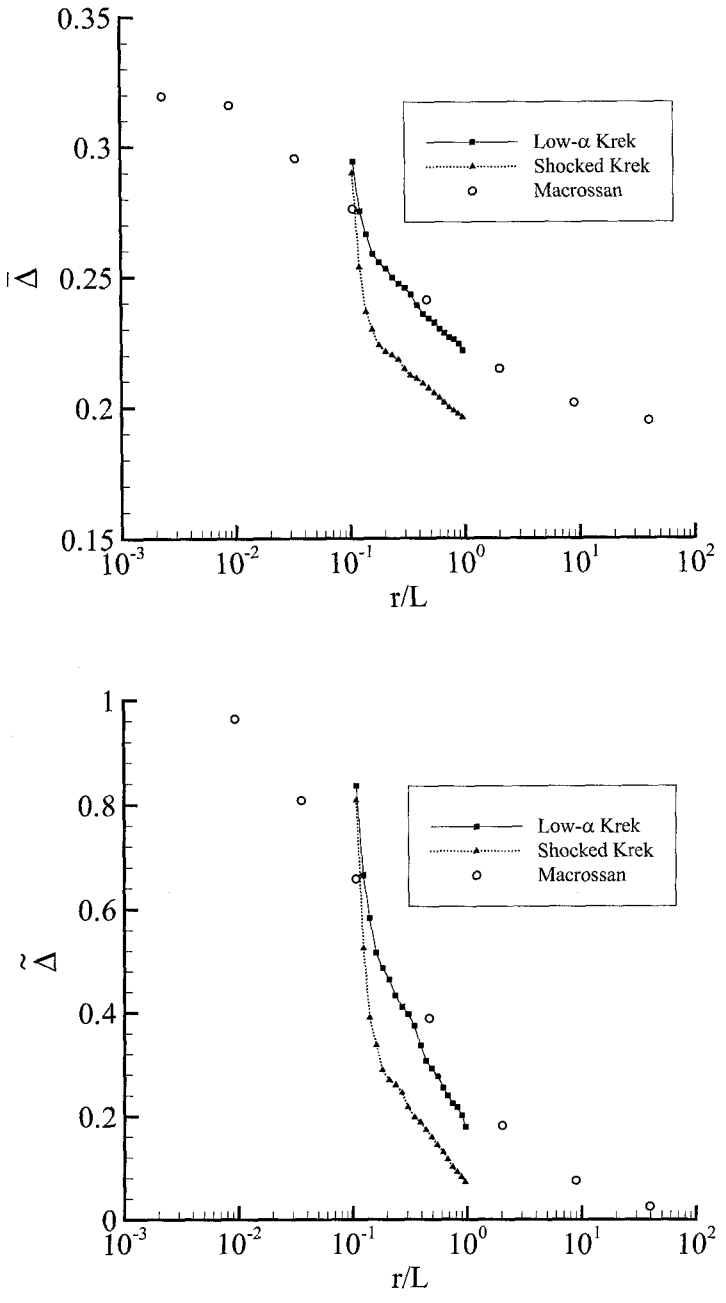

Figure 5.21 Normalized windward bow shock standoff distance vs. (r/L). $\bar{\Delta} = (\Delta/r)(\rho_s/\rho_\infty)$, and $\tilde{\Delta} = (\Delta - \Delta_e)/(\Delta_f - \Delta_e)$. Non-equilibrium inviscid partial grids, EFMO. ρ_s/ρ_∞ is the density ratio across the frozen oblique shock, Δ_f is the standoff distance at the frozen limit, Δ_e is the standoff distance at the equilibrium limit. The plot shows the data at each downstream cell. The partial grid solution starts from a frozen stepback solution. The large gradients in the first few cells correspond to the partial grid solution recovering from the frozen stepback boundary condition.

where the standoff distance was normalized as

$$\bar{\Delta} = \left(\frac{\Delta}{r}\right)\left(\frac{\rho_s}{\rho_\infty}\right), \tag{5.8}$$

where ρ_s/ρ_∞ is the expected density ratio across the characteristic frozen oblique shock. Macrossan and Pullin measured standoff distances for four different freestreams and plotted $\bar{\Delta}$ against r/L_s. The normalization collapsed the frozen limit well, but the data separated to approach different equilibrium limits for the different freestreams.

The second normalization was designed to collapse the data at both the frozen and equilibrium limits. The second normalization is based on the shock standoff distances for the frozen and equilibrium limits, Δ_f and Δ_e, respectively. The normalized standoff distance

$$\widetilde{\Delta} = \frac{\Delta - \Delta_e}{\Delta_f - \Delta_e} \tag{5.9}$$

was plotted against r/L_s, and although the overall correlation was good, the collapse grew slightly worse for $0.01 < (r/L_s) < 20$.

Figure 5.20 shows the bow shock standoff distance from the inviscid non-equilibrium runs. The frozen and equilibrium limits were calculated with the stepback method. For the shocked Krek conditions, the frozen shock was located at $\theta = 5.13°$, which corresponds to $\bar{\Delta} = 0.314$, and the equilibrium shock was located at $\theta = 3.05°$, or $\bar{\Delta} = 0.187$. For the low-α conditions, the frozen shock was located at $\theta = 3.79°$ or $\bar{\Delta} = 0.312$, and the equilibrium shock was located at $\theta = 2.45°$ or $\bar{\Delta} = 0.202$. The frozen and equilibrium limits are defined to be 1 and 0 respectively, for the $\widetilde{\Delta}$ normalization. The Macrossan and Pullin data approaches the frozen and equilibrium limits for $\bar{\Delta}$ in the plots shown here, which were 0.320 and 0.195, respectively.

The partial grid calculation starts from a frozen stepback solution, which has the large standoff distance corresponding to the frozen limit. Four cells downstream of the stepback solution, the partial grid solutions have recovered from the errors, and the trends agree with the Macrossan and Pullin results, although the standoff distance predicted by the partial grids is about 10% lower for $\bar{\Delta}$ and 30% lower for $\widetilde{\Delta}$.

The normalization of r in these plots is by L_s, which ranges from 0.047 m for the shocked Krek conditions to 0.157 m for the low-α Krek conditions. Although the low-α

Krek conditions are very similar to the M & P conditions, the chemical length scales differ by a factor of two, due to the relative sensitivity of the law of mass action at low degrees of dissociation. Ω and L_s are useful as order of magnitude estimates, and perhaps normalizing the downstream distance is not appropriate for normalizing r here. These simulations are intended to model the same dimensional flow past a cone, but normalizing by L_s shifts the two partial grid results half a decade from each other.

Figure 5.21 shows the shock standoff distance when r is normalized by the body length L rather than the chemical length scale L_s. The low-α simulation now agrees quite well with the Macrossan and Pullin data for $\bar{\Delta}$, and agrees fairly well with the $\widetilde{\Delta}$ normalization. Recall that the $\widetilde{\Delta}$ normalization did not collapse well for $0.01 < (r/L_s) < 20$, which corresponds to $0.004 < (r/L) < 8.4$ for the M & P conditions. This is precisely where the partial grid data lies, so the differences for $\widetilde{\Delta}$ are not significant, and the agreement between the low-α conditions and the M & P conditions can be considered very good. However, the shocked Krek conditions are too different to bear comparison with the other freestreams.

5.4.5 Details of the Leeward Flow

This section consists of measurements and observations relating to the leeward shock-vortex system and the separated region.

The separation location was determined from the low-α partial grid solutions by plotting crossflow streamlines. These are shown in Figure 5.22, plotted versus Re_x. This agrees with the trends established earlier: frozen flow separates before equilibrium flow, and non-equilibrium flow separates earlier than than frozen flow, at least for lower Reynolds numbers. The partial grid calculations consistently predict separation at smaller values of ϕ than the stepback calculations. The stepback solutions do exhibit the correct qualitative trends; for all cases, the separation angle reduces with increasing Re_x. The partial grid solutions adjust from the stepback solutions over 4-5 cells. Also, the partial grid solutions level off at $Re_x \approx 65000$. At the same Reynolds number, the frozen and non-equilibrium partial grid solutions converge. As discussed in Section 5.4.3, the change in behavior at the end of the grid is probably due to errors in the downstream boundary condition and should be disregarded.

The first observation is that the large heat transfer in the separated region is due to

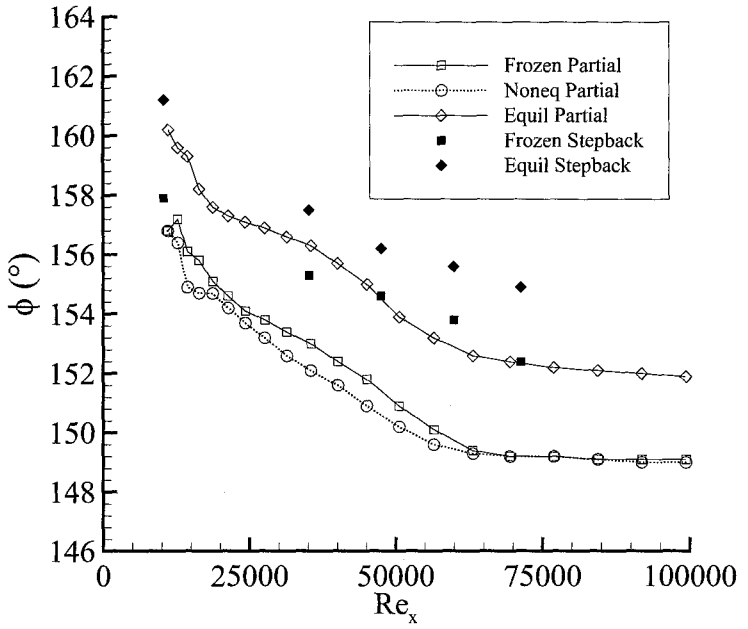

Figure 5.22 Separation location from partial grid solutions. Re_x is the Reynolds number based on freestream conditions and the distance from the tip. ϕ is the azimuthal angle, $\phi = 0°$ at the windward plane, $\phi = 180°$ at the leeward plane.

convection of hot fluid from outside the boundary layer towards the cone surface. Consider Figure 5.23, which shows streamlines and Mach contours from an equilibrium stepback calculation. The fluid near the surface upstream of the separation point has traveled around the cone along streamlines which are very near the cone. This fluid has been cooled by the thermal boundary layer, and it will be relatively near the surface temperature. The fluid which moves along the surface in the region of reversed flow has not been cooled much; these streamlines lie well away from the thermal boundary layer, and have been additionally processed by the leeward shock.

Figure 5.24 shows a comparison of two equilibrium stepback calculations, one with an adiabatic boundary condition and one with an isothermal boundary condition. Dissociation contours are plotted, and the dramatic differences in the boundary layers are clear. In the adiabatic case, the boundary layer is the hottest part of the flow, and the fluid there is almost completely dissociated. The opposite is true in the adiabatic case; the boundary layer is the coldest part of the flow, and is completely recombined. The isothermal boundary layer is thinner, especially so near the separation point. Because the isothermal shear layer is very

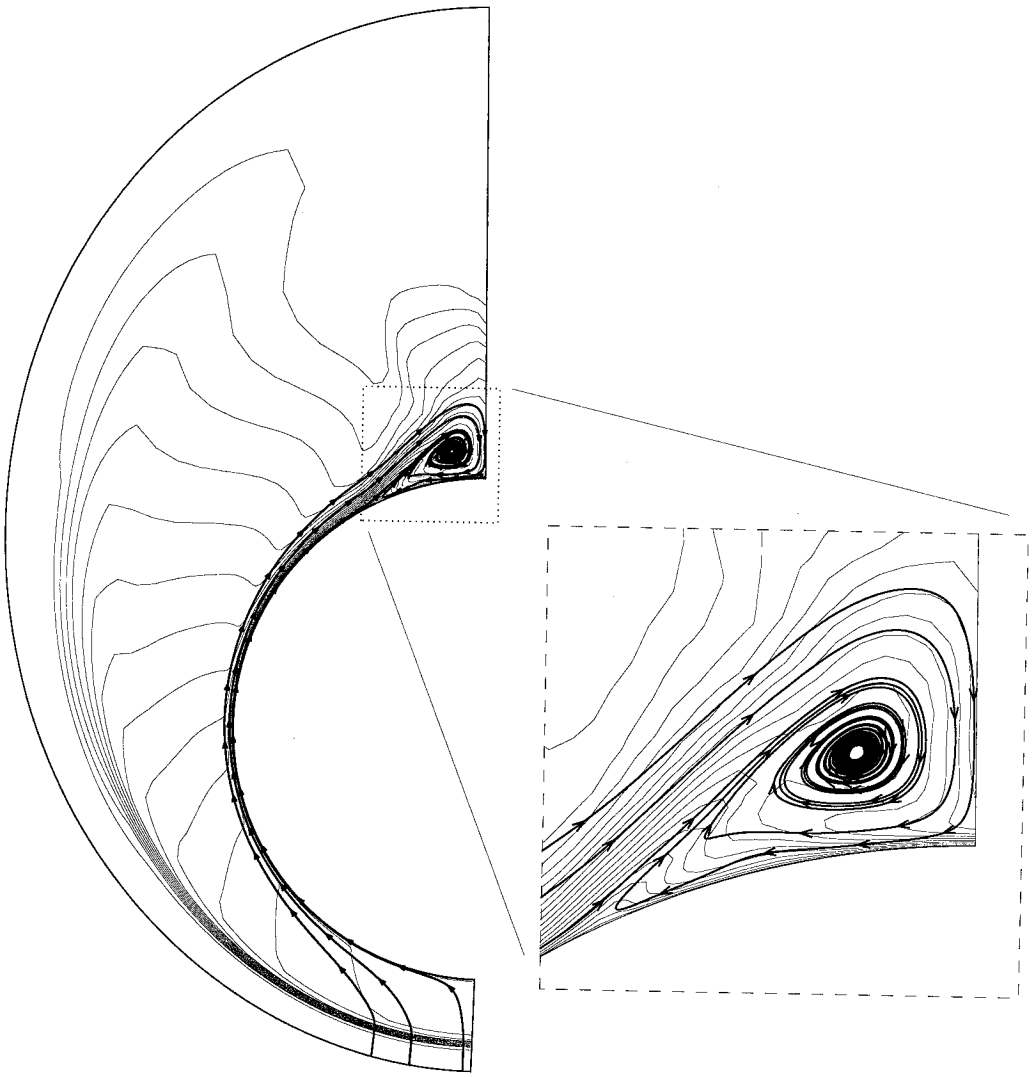

Figure 5.23 Leeward vortex streamlines

cold and dense compared to its adiabatic counterpart, the leeward system can accommodate the mass flow from the separated boundary layer in a smaller vortex. Although the outer edge of vortex is not well distinguished in this figure, the core of the isothermal vortex is clearly closer to the cone surface than the adiabatic vortex.

Figure 5.25 shows dissociation contours from the low-α equilibrium partial grid calculation. Here we can see the effect of the λ-shock on the dissociation reaction. At the windward plane, the flow has dissociated to a relatively high $\alpha \approx 0.15$. As the flow expands around the cone, the fluid recombines, reaching a minimum just upstream of the leeward shock system. This is follow by two jumps in α at the two branches of the λ-shock. Finally, the hot flow behind the leeward shock system is cooled by the cone surface as it enters the vortex.

Figure 5.26 shows temperature contours in the leeward vortex systems at (r/L)=0.033 and (r/L)=0.69 for the shocked Krek conditions. Frozen, non-equilibrium, and equilibrium solutions are shown. Figure 5.27 shows the same plot with crossflow streamlines are plotted over the temperature contours. Note that a larger region is shown for (r/L)=0.69; here we see a larger arc of the cone surface. Many details of the shock-vortex system can be seen in Figure 5.26. The boundary layer and the separated shear layer are clearly seen in all of the plots, and the flow separates earlier at the larger radius. The same trends observed earlier in terms of the effects of chemistry on the separation point are seen here. In Figure 5.26, the vortex is visible for the equilibrium case, and the beginning of the vortex rollup can be seen in the (r/L)=0.69 non-equilibrium case. The λ-shock is clearly seen in the frozen cases, although only the upstream branch is faintly seen in the other cases. From Figure 5.27, we can see that there are slight differences in the size and shape of the vortices for the different chemistry modes, although the largest difference is seen for the (r/L)=0.69 non-equilibrium case, where the vortex is relatively flattened when compared to the other cases.

The most obvious feature of these plots is the low temperature upstream of the shock-vortex system for (r/L)=0.69. This is an interesting example of the effects of non-equilibrium chemistry on the flowfield. There are two types of cooling occurring as the flow passes around the cone: fluid dynamic cooling due to the expansion of the flow, and chemical cooling due to the dissociation reaction. The fluid dynamic cooling is virtually independent of the distance from the tip, but the chemical cooling is not. For flows where the chemical length scale is much smaller than the body length ($L_s \ll L$), the effects of chemical cooling will occur very near the tip, while for flows where ($L_s \gg L$), the chemical cooling will not

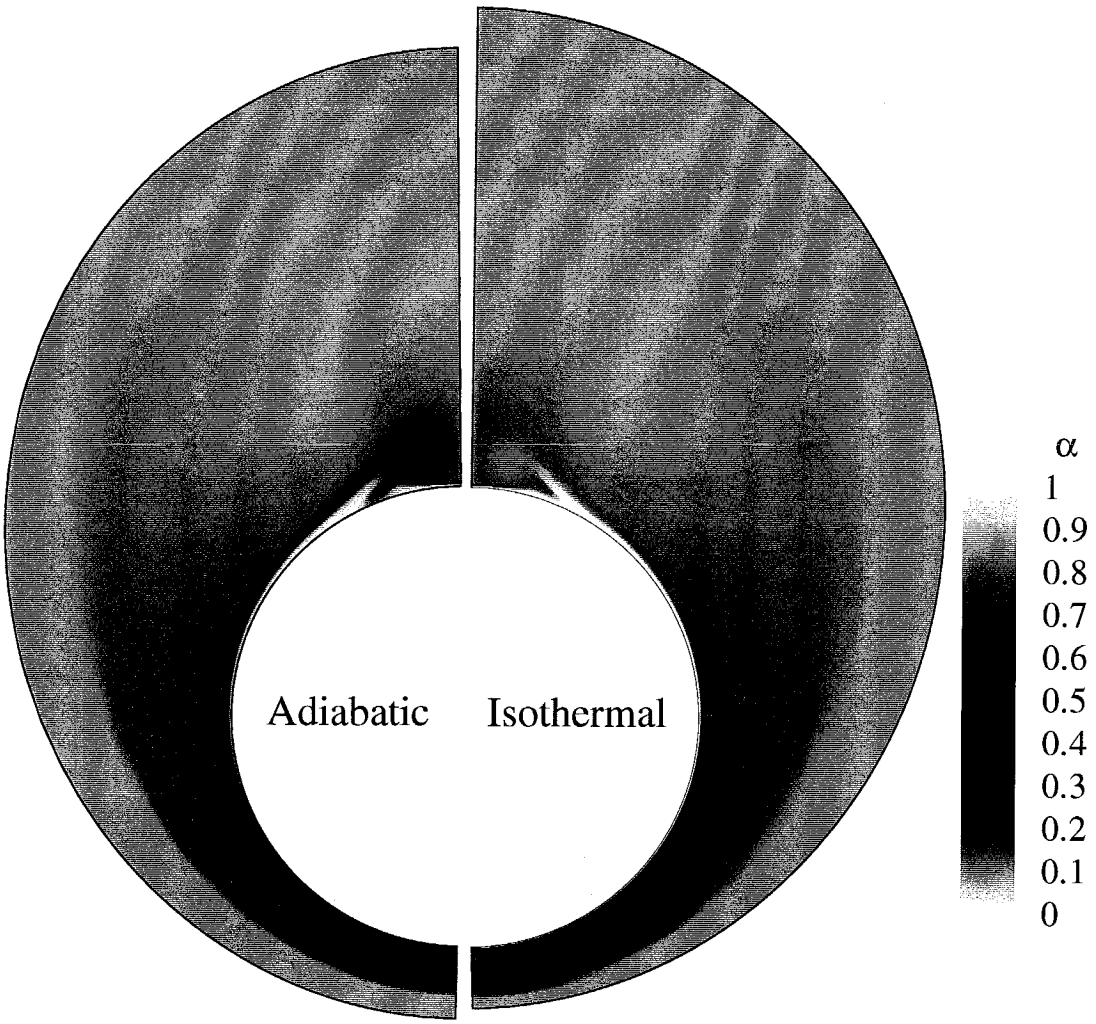

Figure 5.24 Dissociation contours from adiabatic and isothermal stepback simulations. 15° cone at 30° incidence. Shocked Krek conditions, M=3.6. EFMO. Isothermal, T_w=300 K. (r/L)=0.69.

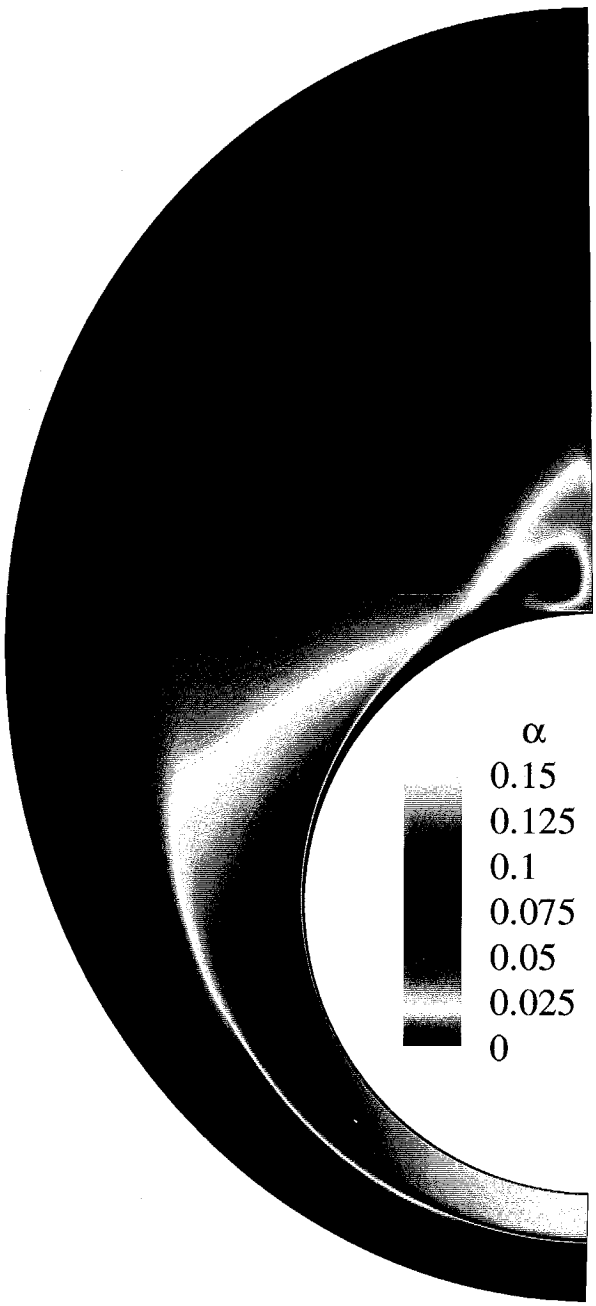

Figure 5.25 Dissociation contours from an equilibrium partial grid simulation. 15° cone at 30° incidence. Low-α Krek conditions, M=5.0. EFMO. Isothermal, T_w=300 K. (r/L)=0.69.

occur until after the flow has completely passed the body.

Recall from Table 5.1 that $\Omega = L/L_s = 1.15$ for the low-α conditions, and $\Omega = 3.8$ for the shocked conditions. Since the chemical length scale L_s is of the same order as the body length L, the relaxation zone of the dissociation reaction will be at least partially captured. Near the tip, the dissociation reaction will not have proceeded far, and the effects of chemical cooling will be smaller. At larger downstream distances, the reaction will have proceeded farther, and the chemical cooling will result in lower temperatures than those seen near the tip. At the smaller radius, very little chemical cooling has occurred, and the cooling is primarily due to the expansion. Upstream of the non-equilibrium vortex, the temperature is not very different from the frozen and equilibrium solutions. However, at the larger radius, the chemical cooling has started, and its effect is superimposed on the expansion cooling. This results in the substantially lower temperature upstream of the non-equilibrium leeward vortex. Since the velocities for the three cases are similar here, this results in a higher Mach number for the non-equilibrium case. This can be seen in Figure 5.28, which shows Mach contours from the (r/L)=0.69 station for the three cases. For the frozen and equilibrium cases, the maximum Mach number in the flow is about 5% higher than the freestream Mach number. However, for the non-equilibrium case, the relatively low temperatures lead to a maximum Mach number of 4.3, about 19% higher than the freestream Mach number. This is yet another example of how the non-equilibrium case is not bracketed by the other two cases.

Finally, Figures 5.29 and 5.30 show dissociation and temperature contours at various downstream stations of the non-equilibrium partial grid. Figure 5.29 shows dissociation contours at (r/L)=0.18, 0.30, 0.44, 0.55, and 0.67. An equilbrium partial grid result from (r/L)=0.69 is also shown for comparison. Figure 5.30 shows temperature contours for the same stations.

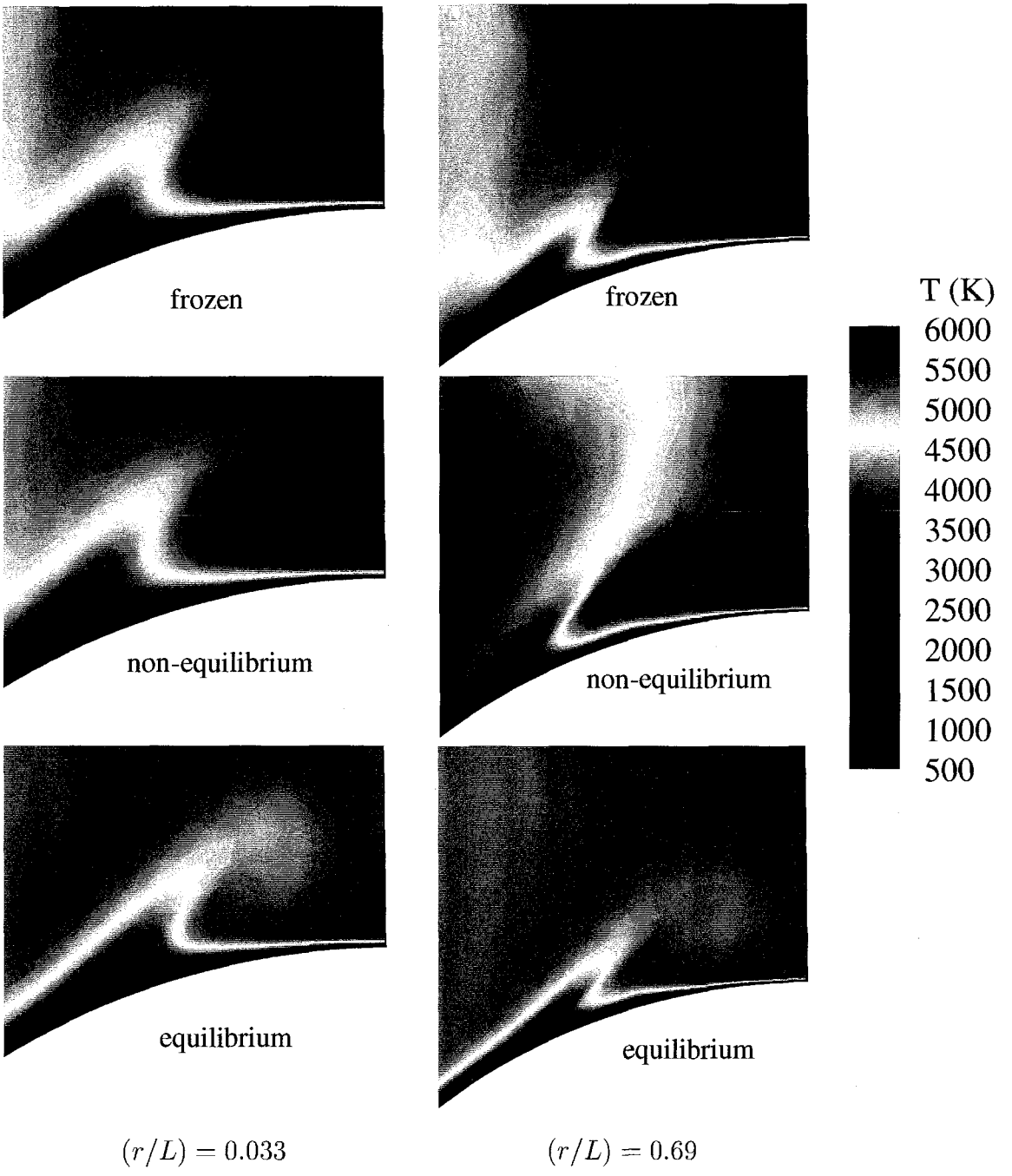

Figure 5.26 Leeward vortex details from partial grid simulations without streamlines. 15° cone at 30° incidence. Shocked Krek conditions, M=3.6. EFMO. Isothermal, T_w=300 K.

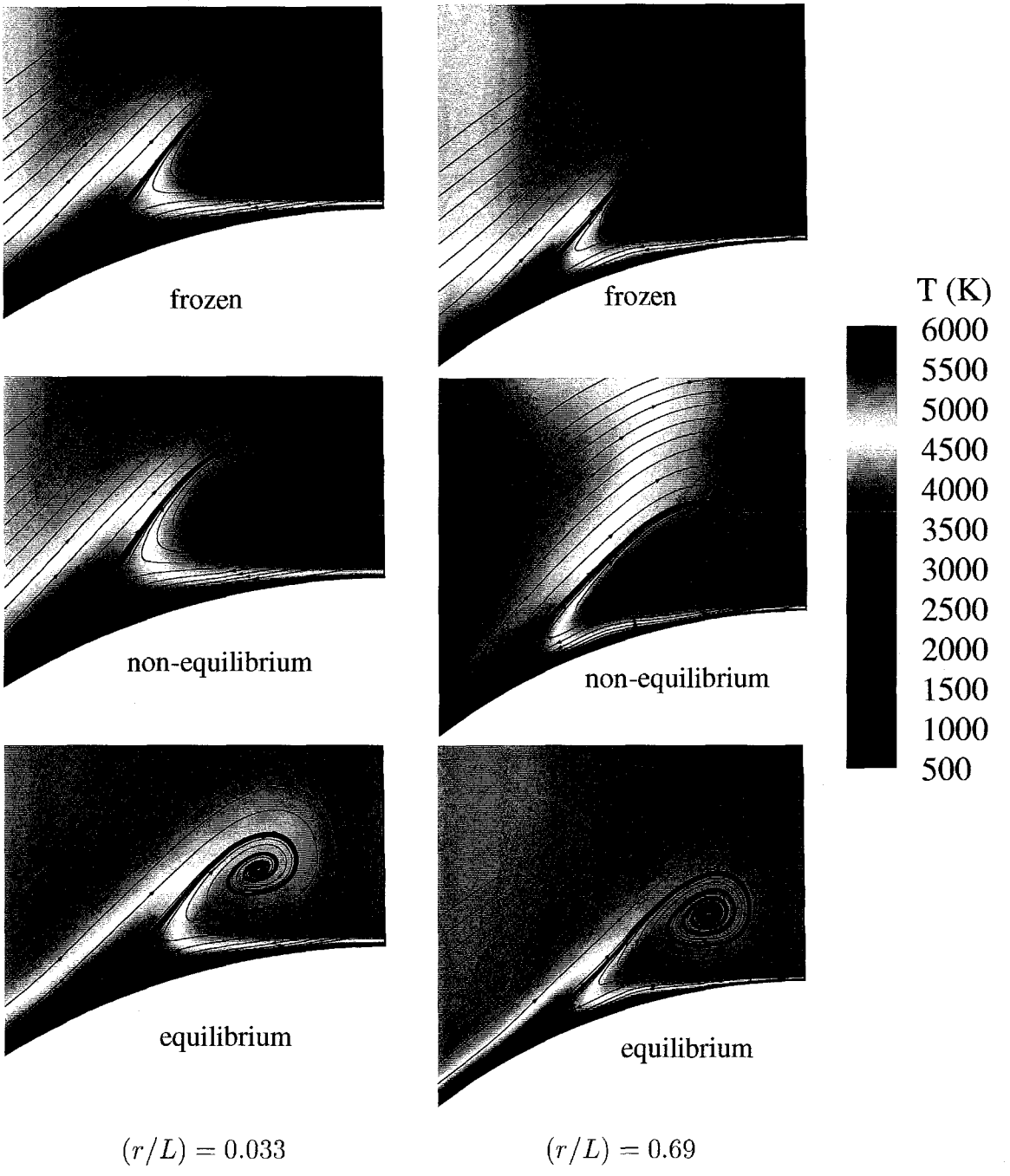

Figure 5.27 Leeward vortex details from partial grid simulations with streamlines. 15° cone at 30° incidence. Shocked Krek conditions, M=3.6. EFMO. Isothermal, T_w=300 K.

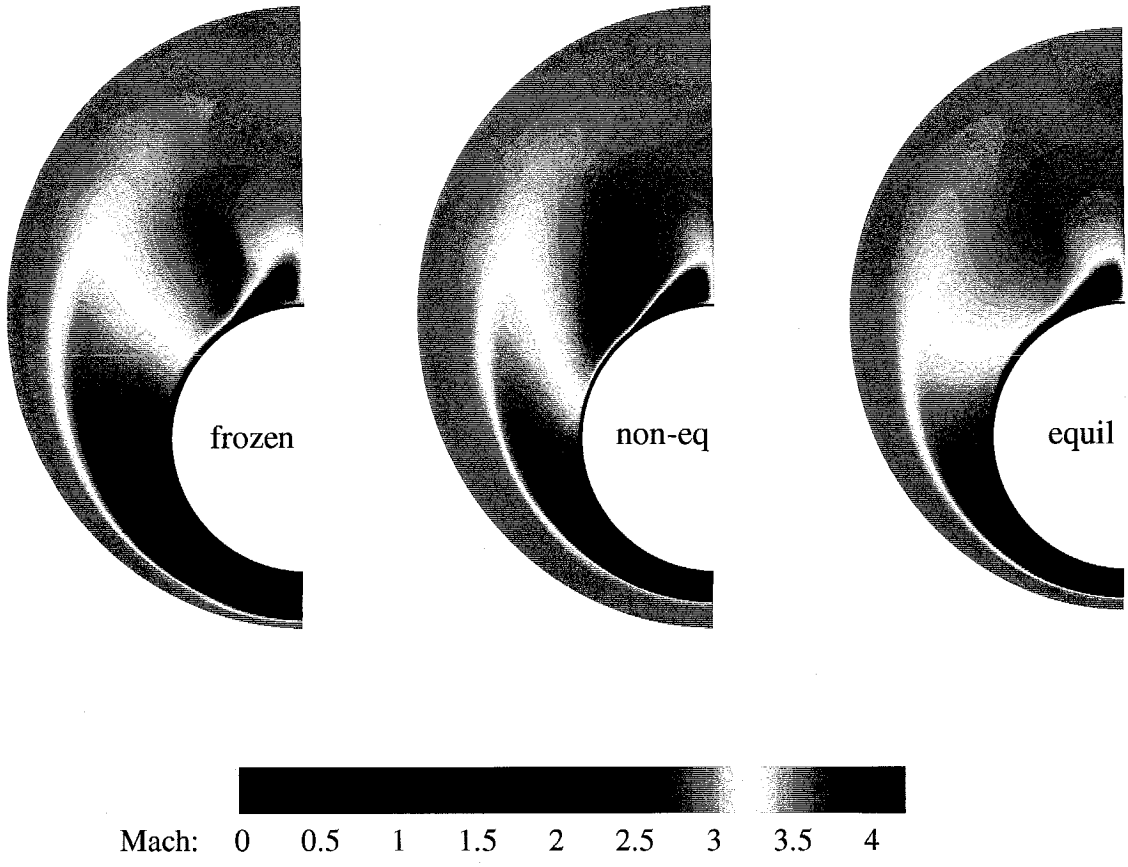

Figure 5.28 Mach contours from partial grid simulations. 15° cone at 30° incidence. Shocked Krek conditions, M=3.6. EFMO. Isothermal, T_w=300 K. (r/L)=0.69.

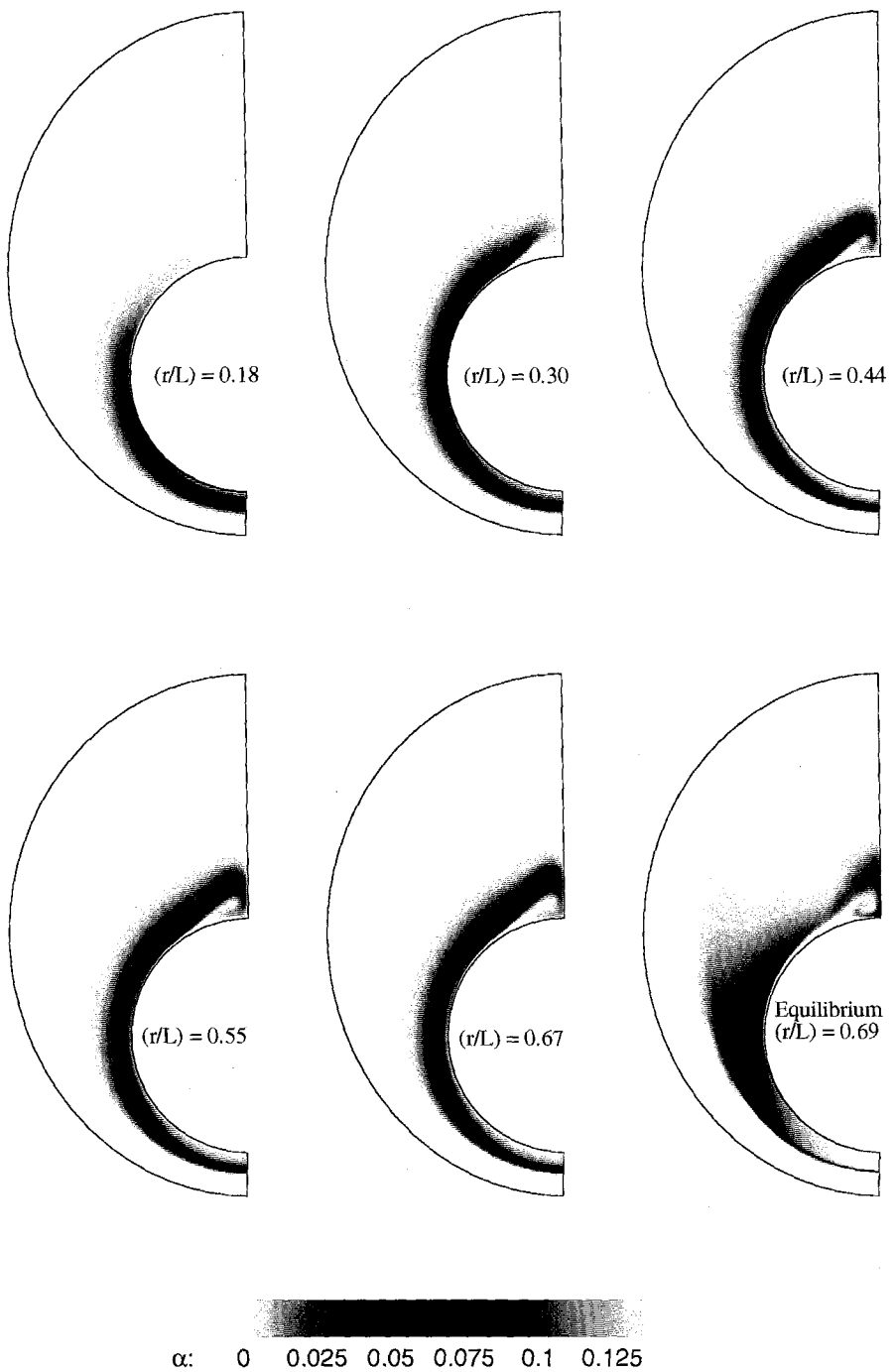

Figure 5.29 Dissociation contours from a non-equilibrium partial grid simulation. 15° cone at 30° incidence. Low-α Krek conditions, M=5.0. EFMO. Isothermal, T_w=300 K. The final plot is an equilibrium partial grid solution, shown for comparison.

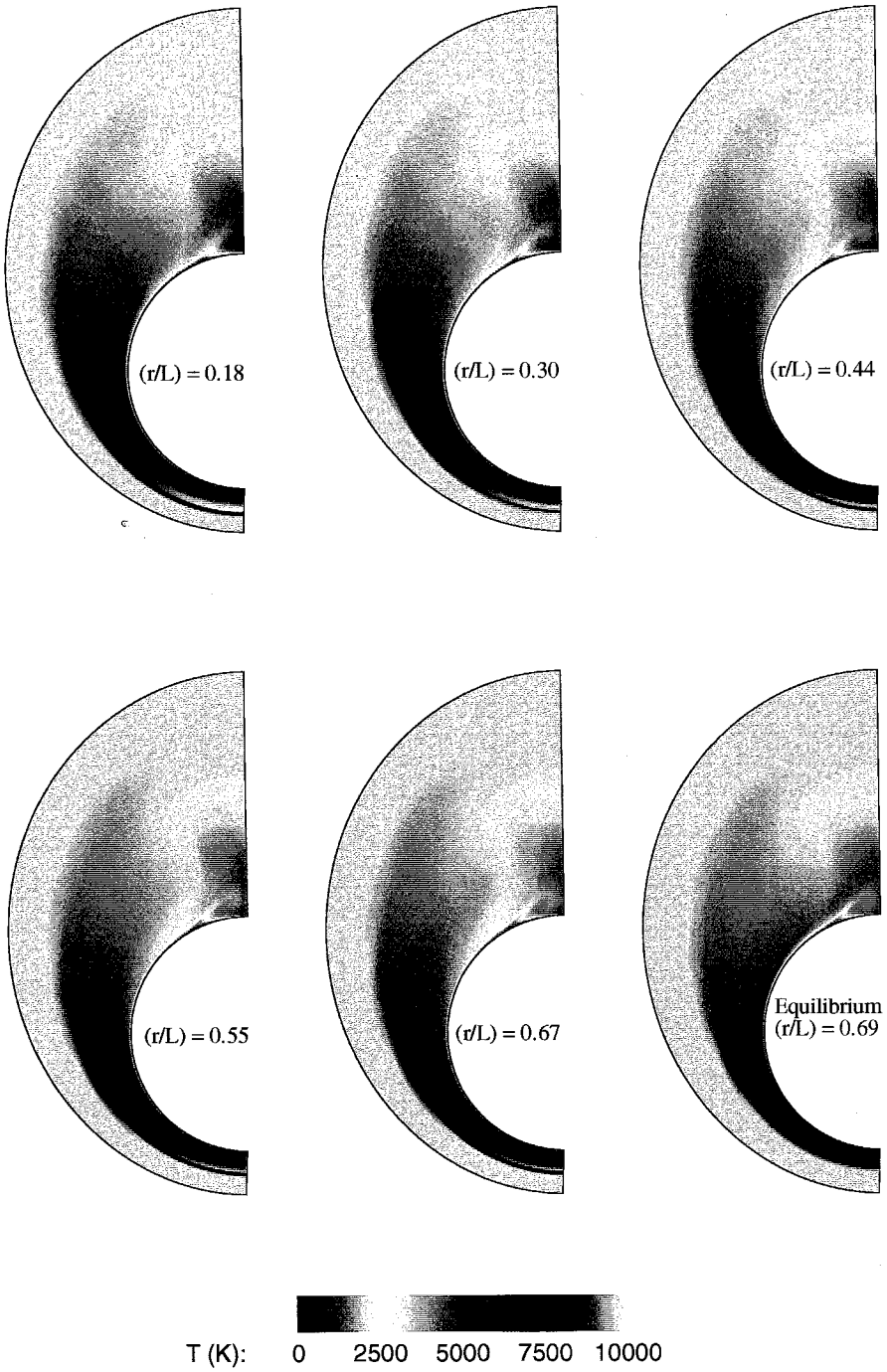

Figure 5.30 Temperature contours from a non-equilibrium partial grid simulation. 15° cone at 30° incidence. Low-α Krek conditions, M=5.0. EFMO. Isothermal, T_w=300 K. The final plot is an equilibrium partial grid solution, shown for comparison.

Chapter 6

Conclusions

The stepback and partial grid methods have been shown to be effective and relatively computationally cheap techniques for approximately solving viscous frozen and viscous reacting flows past cones. This chapter lists the conclusions drawn from the simulations performed in this work.

6.1 Frozen Flow at Zero Incidence

Frozen laminar flow past a cone at zero incidence was simulated with stepback, partial grid, and full grid calculations. This simple case was used to test the differences between the methods. These computations involved a cone of half-angle 10° in air at M=7.95. Adiabatic computations were performed for Pr=1.

- The stepback method tended to underestimate the laminar boundary layer thickness, although it predicted the correct adiabatic wall temperature and shape of the boundary layer profile.

- When a stepback solution was used as a boundary condition for a partial grid computation, the errors from the stepback solution disappeared a short distance downstream of this boundary. This means that the boundary layer increased over only a few radial cells and the solution at the radius of interest was very close to that obtained from the full calculation.

- Partial grid calculations required much less computation time than full grid calculations which attempt to resolve the tip flow, but the results were comparable.

6.2 Frozen Flow at Incidence

High resolution stepback calculations were used to compute the frozen laminar flow past a 10° cone at 24° incidence. The resolution was ($2 \times 150 \times 200$). This test was for air at M=7.95, although the boundary condition here was an isothermal wall at 300 K, and Pr=0.72. The Reynolds numbers based on freestream conditions and the distance from the tip were Re_x=360000 and Re_x=420000. The results were compared with experiments by Tracy [5].

- The topology and features of the flow field agreed very well with the pitot pressure surveys of Tracy.
    - The shock standoff distance was overestimated at the windward plane, but the position of the bow shock agreed well elsewhere.
    - The thickness of the laminar boundary layer was well-predicted, as was the point of separation and the location of the separated shear layer.
    - The leeward λ-shock was sharply captured, although the shock system was slightly skewed relative to Tracy's findings.
    - There was no discernible difference in the flow features between EFM and EFMO.
- The EFMO surface pressure and heat transfer agreed very well with the experimental findings. There was no significant difference in surface pressure between EFM and EFMO, but the EFM simulation considerably overpredicted the heat transfer.
    - The surface pressure dropped as the flow expanded around the cone, reaching a minimum upstream of separation. The surface pressure reached a plateau at the separation point, and rose at the leeward plane of symmetry.
    - The laminar heat transfer also dropped as the flow expands around the cone. The heat transfer reached a minimum at separation, and there was a moderate recovery of heat transfer in the separated region.

6.3 Reacting Flow at Incidence

Reacting laminar flow past a cone at incidence was computed with stepback and partial grid solutions, and the trends regarding both chemistry and the solution method were typified. These simulations were compared with results from Krek [6], who tested M=4.57 flow of nitrogen over a 15° cone at 30° incidence, with stagnation enthalpy h_0=27.17 MJ/kg. The Krek freestream was in a state of non-equilibrium, and two sets of equivalent equilibrium conditions were used as the basis of the simulations.

- Frozen and equilibrium stepback solutions were calculated at several stations using a resolution of $(2 \times 45 \times 100)$. The effects of chemistry on the heat transfer and separation location were observed.
    - On the windward side of the cone, the equilibrium solution had lower heat transfer than the frozen solution. As the flow expanded around the cone, the frozen heat transfer became smaller, up to the separation point. In the separated region, the equilibrium heat transfer was lower. The heat transfer recovery in the separated region was very large, almost reaching the magnitude of the windward heat transfer.
    - Frozen solutions predicted earlier separation than equilibrium solutions, with a concomitant relative increase in the size of the leeward vortex.
    - The large recovery in heat transfer in the separated region was interpreted as being due to the convection of hot, energetic, shocked fluid from outside the boundary layer towards the surface of the cone.
- Frozen, non-equilibrium, and equilibrium partial grid computations were performed. The partial grids extended from (r/L)=0.1 to (r/L)=1, and the resolution of the grids was $(20 \times 45 \times 100)$. The effects of chemistry were examined, as were the variations due to grid solution technique (stepback or partial grid).
    - For frozen and equilibrium flows, the partial grid results showed the same trends with chemistry as the stepback solutions.
    - The non-equilibrium solutions were not bracketed by the frozen and equilibrium solutions. The non-equilibrium heat transfer was lower than both the frozen and equilibrium heat transfer up to the point of separation.

- The non-equilibrium solution's separation point was either at the same location as the frozen solution, or slightly upstream of the frozen separation point.
- The superposition of non-equilibrium chemical cooling and fluid dynamic cooling led to low temperature, high Mach number states upstream of the leeward shock. In this case, the resulting vortex had a flattened shape relative to the frozen and equilibrium vortices. These effects were seen at larger Reynolds numbers for these conditions. This was contrary to Krek's findings, which reported that no Reynolds number effects were observed.
- The viscous non-equilibrium partial grids required five cells to recover from the frozen stepback solution as determined from the location of separation.

- The shock standoff distance was measured using inviscid non-equilibrium partial grid calculations. These grids had the same domain and resolution as the viscous partial grids, but the grid stretching in the crossflow plane allowed much better resolution of the windward shock. These results were compared with an inviscid simulation of a similar flow by Macrossan and Pullin [16].
  - The shock standoff distance was essentially an inviscid phenomenon which was unaffected by the extremely thin isothermal boundary layer.
  - Chemistry had a large effect on the shock standoff distance. The equilibrium standoff distance was 35–40% smaller than the frozen standoff distance for these conditions.
  - The partial grid simulations predicted lower standoff distances than the Macrossan and Pullin data. The agreement became better when the downstream distance was normalized by the body length instead of the chemical length scale, which was too sensitive to small differences in the freestream state.
  - The inviscid non-equilibrium partial grid also adjusted from the frozen stepback solution over five cells, as determined from the shock standoff distance.

- These results suggest the following conclusions regarding the simulation of reacting flows with the stepback and partial grid techniques.
  - Some of the chemistry effects are very subtle. In terms of features such as

separation location, these effects are of the same order as the errors associated with the stepback method.

- For high accuracy simulation of reacting flows, the stepback method should not be used alone. A reacting flow simulation requires the higher accuracy of the partial grid technique.

We conclude with a suggestion for those who wish to pursue simulation of cone flows with these methods. For this work, the reacting stepback grids were of moderate crossflow resolution. This was for several reasons. First, most of the length of the cone was contained in the domain, to capture most of the flow in a single partial grid calculation. Second, the stepback and partial grids had the same crossflow resolution to facilitate direct comparison of the methods. Third, the extremely thin isothermal boundary layers required that the bow shock be poorly resolved. Alternatively, a high resolution stepback calculation could be performed upstream of each radius of interest. Then a shorter partial grid calculation with higher crossflow resolution and lower downstream resolution might be used to compute the flow at each station. Future work is needed to explore how large a partial grid domain must be to eliminate most of the errors from the stepback solution.

Lastly, we emphasize that all attached boundary layers were laminar. The accurate computation of hypervelocity reacting flow past bodies in the presence of boundary layer transition remains a challenge for future computation.

Bibliography

[1] D. I. PULLIN. Direct simulation methods for compressible inviscid ideal-gas flow. *Journal of Computational Physics*, **34**:231–244, 1980.

[2] J.-M. MOSCHETTA AND D. I. PULLIN. A robust low diffusive kinetic scheme for the Navier-Stokes/Euler equations. *Journal of Computational Physics*, **133**:193–204, 1997.

[3] M. J. LIGHTHILL. Dynamics of a dissociating gas. Part 1, equilibrium flow. *Journal of Fluid Mechanics*, **2**:1–32, 1957.

[4] N. C. FREEMAN. Non-equilibrium flow of an ideal dissociating gas. *Journal of Fluid Mechanics*, **4**:407–425, 1958.

[5] R. R. TRACY. *Hypersonic Flow over a Yawed Circular Cone.* Ph.D. thesis, TR-69, Caltech, Pasadena, 1964.

[6] R. M. KREK. *Three Dimensional Flows in a Free Piston Shock Tunnel.* Ph.D. thesis, University of Queensland, Brisbane, 1992.

[7] A. H. WHITEHEAD, JR. Effect of vortices on delta wing lee-side heating at Mach 6. *AIAA Journal*, **8**:599–600, 1970.

[8] R. J. STALKER. Approximation for non-equilibrium hypervelocity aerodynamics. *AIAA Journal*, **27**:1761–1769, 1989.

[9] J. R. MAUS, B. J. GRIFFITH, K. Y. SZEMA, AND J. T. BEST. Hypersonic Mach number and real gas effects on space shuttle orbiter aerodynamics. *Journal of Spacecraft and Rockets*, **21**:136–141, 1984.

[10] A. FERRI. Supersonic flows with shock waves. In *General Theory of High Speed Aerodynamics: High Speed Aerodynamics and Jet Propulsion, Vol. 7*, W. R. Sears, editor, 721–747. Princeton University Press, Princeton, 1954.

[11] A. H. SHAPIRO. *The Dynamics and Thermodynamics of Compressible Fluid Flow.* The Ronald Press Company, New York, 1954.

[12] J. D. ANDERSON, JR. *Modern Compressible Flow with Historical Perspective, Second Edition.* McGraw-Hill, New York, 1990.

[13] F. MARCONI. The spiral singularity in the supersonic inviscid flow over a cone. AIAA Paper 83–1665, 1983.

[14] F. MARCONI. On the prediction of highly vortical flows using an Euler equation model. In *Studies of Vortex-Dominated Flows*, M. Y. Hussaini and M. D. Salas, editors, 311–364. Springer-Verlag, Berlin, 1987.

[15] F. MARCONI. Complex shock patterns and vortices in inviscid supersonic flows. *Computers and Fluids*, **17**:151–163, 1989.

[16] M. N. MACROSSAN AND D. I. PULLIN. A computational investigation of inviscid hypervelocity flow of a dissociating gas past a cone at incidence. *Journal of Fluid Mechanics*, **266**:69–92, 1994.

[17] J. H. B. SMITH. Remarks on the structure of conical flow. *Progress in Aeronautical Sciences*, **12**:241–271, 1972.

[18] W. J. RAINBIRD. The external flow field about yawed circular cones. AGARD CP3O, 1968.

[19] J. C. R. HUNT, C. J. ABELL, J. A. PETERKA, AND H. WOO. Kinematical studies of the flows around free or surface-mounted obstacles; applying topology to flow visualization. *Journal of Fluid Mechanics*, **86**:179–200, 1978.

[20] J.-M. MOSCHETTA, A. LAFON, AND H. DENIAU. Detailed numerical investigation of supersonic crossflow separation. AIAA Paper 94–2382, 1994.

[21] M. HOLT AND J. BLACKIE. Experiments on circular cones at yaw in supersonic flow. *Journal of the Aeronautical Sciences*, **23**:931–936, 1956.

[22] R. H. FELDHUHN AND A. E. WINKELMANN. An experimental investigation of the flowfield around a yawed cone. *AIAA Journal*, **9**:1074–1081, 1971.

[23] C. WEN. *Hypervelocity Flow over Spheres.* Ph.D. thesis, Caltech, Pasadena, 1994.

[24] G. I. TAYLOR AND J. W. MACCOLL. The air pressure on a cone moving at high speed. *Proceedings of the Royal Society of London, Series A*, **139**:278–311, 1933.

[25] A. H. STONE. On supersonic flow past a slightly yawing cone. *Journal of Mathematical Physics*, **27**:67–81, 1948.

[26] A. H. STONE. On supersonic flow past a slightly yawing cone II. *Journal of Mathematical Physics*, **30**:200–213, 1952.

[27] A. FERRI. Supersonic flows around circular cones at angles of attack. NACA TN 2236, 1950.

[28] H. K. CHENG. Hypersonic flows past a yawed circular cone and other pointed bodies. *Journal of Fluid Mechanics*, **12**:169–191, 1962.

[29] J. J. QUIRK. A contribution to the great Riemann solver debate. *International Journal for Numerical Methods in Fluids*, **18**:555–574, 1994.

[30] J. C. MANDAL AND S. M. DESHPANDE. Kinetic flux vector splitting for the Euler equations. *Computers and Fluids*, **23**:447–478, 1994.

[31] P. VILLEDIEU AND P. MAZET. Kinetic schemes for the Euler equations out of thermochemical equilibrium. *La Recherche Aérospatiale*, **2**:85–102, 1995.

[32] W. G. VINCENTI AND C. H. KRUGER, JR. *Introduction to Physical Gas Dynamics.* Krieger, Malabar, Florida, 1965.

[33] M. ABRAMOWITZ AND I. A. STEGUN. *Handbook of Mathematical Functions.* Dover, New York, 1972.

[34] M. N. MACROSSAN. The Equilibrium Flux Method for the calculation of flows with non-equilibrium chemical reactions. *Journal of Computational Physics*, **80**:204–231, 1989.

[35] B. VAN LEER. Towards the ultimate conservative difference scheme II: Monotonicity and conservation combined in a second order scheme. *Journal of Computational Physics*, **14**:361–370, 1974.

[36] P. L. ROE. Some contributions to the modeling of discontinuous flows. *Lecture Notes in Applied Mathematics*, **22**:163–193, 1985.

[37] R. J. LEVEQUE. *Numerical Methods for Conservation Laws.* Birkhäuser, Basel, 1992.

[38] B. VAN LEER. Towards the ultimate conservative difference scheme V: A second order sequel to Godunov's method. *Journal of Computational Physics*, **32**:101–136, 1979.

[39] S. Y. CHOU AND D. BAGANOFF. Kinetic flux-vector splitting for the Navier-Stokes equations. *Journal of Computational Physics*, **130**:217–230, 1997.

[40] P. A. THOMPSON. *Compressible-Fluid Dynamics.* McGraw-Hill, New York, 1972.

[41] F. M. WHITE. *Viscous Fluid Flow, Second Edition.* McGraw-Hill, New York, 1991.

[42] S. OSHER AND F. SOLOMON. Upwind difference schemes for hyperbolic systems of conservation laws. *Mathematics of Computation*, **38**:339–374, 1982.

[43] C. PARK. Assessment of two-temperature kinetic model for dissociating and weakly ionizing nitrogen. AIAA Paper 86–1347, 1986.

[44] R. K. HANSON AND D. BAGANOFF. Shock-tube study of nitrogen dissociation rates using pressure measurements. *AIAA Journal*, **10**:211–215, 1972.

[45] D. J. KEWLEY AND H. G. HORNUNG. Free-piston shock-tube study of nitrogen dissociation. *Chemical Physics Letters*, **25**:531–536, 1974.

[46] J. H. FERZIGER AND M. PERIĆ. *Computational Methods for Fluid Dynamics.* Springer-Verlag, Berlin, 1996.

[47] L. B. SCHIFF AND J. L. STEGER. Numerical simulation of steady supersonic viscous flow. AIAA Paper 79–0130, 1979.

[48] Y. C. VIGNERON, J. V. RAKICH, AND J. C. TANNEHILL. Calculation of supersonic viscous flow over delta wings with sharp subsonic leading edges. AIAA Paper 78–1137, 1978.

[49] E. R. MALLETT. *A Numerical Study of Hypersonic Leeward Flow over the Delta Wing of the Hermes Spacecraft Using a Parallel Architecture Supercomputer.* Ph.D. thesis, California Institute of Technology, Pasadena, California, 1992.

[50] P. L. ROE. Approximate Riemann solvers, parameter vectors, and difference schemes. *Journal of Computational Physics*, **43**:357–372, 1981.

[51] J.-M. MOSCHETTA. Private communication, 1995.

[52] K. STEWARTSON. *The Theory of Laminar Boundary Layers in Compressible Fluids.* Oxford, Clarendon, 1964.

[53] J. D. ANDERSON, JR. *Introduction to Flight, Third Edition.* McGraw-Hill, New York, 1989.

[54] W. MYERS. Caltech dedicates world's most powerful supercomputer. *Computer*, **24**:96–97, 1991.

[55] PARASOFT. *Express User's Guide.* Parasoft, 1992.

[56] J. J. QUIRK. Amrita — a computational facility (for CFD modelling). VKI 29th CFD Lecture Series Notes, Caltech, Pasadena, 1998.

[57] K. C. CRANE AND R. J. STALKER. Mass-spectrometric analysis of hypersonic flows. *Journal of Physics D: Applied Physics*, **10**:679–695, 1977.

[58] G. O. ROBERTS. Computational meshes for boundary layer problems. *Lecture Notes in Applied Physics*, **8**:171–177, 1971.

[59] M. N. ÖZIŞIK. *Heat Transfer: A Basic Approach.* McGraw-Hill, New York, 1985.

[60] H. G. HORNUNG. Non-equilibrium dissociating nitrogen flow over spheres and circular cylinders. *Journal of Fluid Mechanics*, **53**:149–176, 1972.

[61] F. G. BLOTTNER, M. JOHNSON, AND M. ELLIS. Chemically reacting viscous flow program for multi-component gas mixtures. Report No. SC–RR–70–754, Sandia Laboratories, Albuquerque, NM, 1971.

[62] G. V. CANDLER. *The Computation of Weakly Ionized Supersonic Flows in Thermo-Chemical Nonequilibrium.* Ph.D. thesis, Stanford University, Stanford, 1988.

[63] W. H. DORRANCE. *Viscous Hypersonic Flow; Theory of Reacting and Hypersonic Boundary Layers.* McGraw-Hill, New York, 1962.

[64] C. R. WILKE. Approximate formula for the thermal conductivity of gas mixtures. *Journal of Chemical Physics*, **18**:517–522, 1950.

[65] E. A. MASON AND S. C. SAXENA. A viscosity equation for gas mixtures. *Physics of Fluids*, **1**:361–369, 1958.

Appendix A

Determination of EFMO Intermediate States

This appendix outlines the algorithm for determining the intermediate states U_1 and U_2 for the calculation of the EFMO numerical flux [2]. The first step is the evaluation of the expression

$$A = a_L + a_R + \varepsilon \frac{\gamma - 1}{2}(v_{n_L} - v_{n_R}). \tag{A.1}$$

As discussed in Section 2.3, $\varepsilon = \pm 1$. If A is negative, ΔF can be set to zero, although this arises only in very extreme situations such as vacuum apparition. Otherwise, the following calculations are performed to define U_1 and U_2:

$$s_L = \frac{p_L}{\rho_L^{\gamma}} \tag{A.2}$$

$$s_R = \frac{p_R}{\rho_R^{\gamma}} \tag{A.3}$$

$$\rho_1 = \rho_L \left[\frac{A}{a_L(1 + (s_R/s_L)^{1/2\gamma}} \right]^{2/(\gamma-1)} \tag{A.4}$$

$$\rho_2 = \rho_1 (s_R/s_L)^{1/\gamma} \tag{A.5}$$

$$p_1 = p_2 = p^* = s_L \rho_1^{\gamma} \tag{A.6}$$

$$a_1 = \sqrt{\gamma p_1/\rho_1} \tag{A.7}$$

$$v_n{}^* = v_{n_L} - \frac{2\varepsilon}{\gamma - 1}(a_1 - a_L) \tag{A.8}$$

$$v_{n_1} = v_{n_2} = v_n{}^* \tag{A.9}$$

$$v_{p_1} = v_{p_L} \tag{A.10}$$

$$v_{p_2} = v_{p_R} \tag{A.11}$$

$$v_{q_1} = v_{q_L} \tag{A.12}$$

$$v_{q_2} = v_{q_R} \tag{A.13}$$

Appendix B

Transport Properties for Reacting Flow

For reacting flow, species viscosity and conductivity rules are used, then mixing rules based on Chapman-Enskog theory are used to compute mixture properties. The species viscosity can be calculated using a viscosity model developed by Blottner et al. [61]. This model was developed for reacting air, and the curve fits are appropriate for temperatures up to 10,000 K [62]. Some regions of the flows simulated here reach temperatures higher than this, but this is not true where viscosity is important, such as the cold-wall boundary layers. The model uses a three-constant curve fit for the viscosity of each species i, where $i = 1$ refers to the monatomic species, and $i = 2$ refers to the diatomic species.

$$\mu_i = 0.1 \exp[(A_i \ln T + B_i) \ln T + C_i], \tag{B.1}$$

where T is temperature and the values of A, B, and C can be found in Table B.1.

Species	A	B	C
N	0.0115572	0.6031679	-12.4327495
N_2	0.0268142	0.3177838	-11.3155513
O	0.0203144	0.4294404	-11.6031403
O_2	0.0449290	-0.0826158	-9.2019475

Table B.1 Viscosity coefficients for Blottner model

The species conductivities are related to the species viscosities by

$$k_1 = \frac{15}{2} \mu_1 R_2 \tag{B.2}$$

and

$$k_2 = \frac{21}{4} \mu_2 R_2, \tag{B.3}$$

where R_2 is the gas constant for the diatomic species [63]. The mixture viscosity can be

calculated using mixture rules from Wilke [64], using

$$\mu = \frac{X_1\,\mu_1}{X_1 + G_{12}\,X_2} + \frac{X_2\,\mu_2}{X_2 + G_{21}\,X_1}, \tag{B.4}$$

where

$$X_1 = \frac{2\alpha}{1+\alpha} \tag{B.5}$$

and

$$X_2 = \frac{1-\alpha}{1+\alpha}. \tag{B.6}$$

The weighting factors G_{12} and G_{21} are

$$G_{12} = \frac{\left(1 + \left(\frac{\mu_1}{\mu_2}\right)^{1/2}\left(\frac{W_2}{W_1}\right)^{1/4}\right)^2}{\left(8\left(1+\frac{W_1}{W_2}\right)\right)^{1/2}} \tag{B.7}$$

and

$$G_{21} = \frac{\left(1 + \left(\frac{\mu_2}{\mu_1}\right)^{1/2}\left(\frac{W_1}{W_2}\right)^{1/4}\right)^2}{\left(8\left(1+\frac{W_2}{W_1}\right)\right)^{1/2}}. \tag{B.8}$$

Similarly, the mixture conductivity is given by

$$k = \frac{X_1\,k_1}{X_1 + 1.065\,G_{12}\,X_2} + \frac{X_2\,k_2}{X_2 + 1.065\,G_{21}\,X_1}, \tag{B.9}$$

where G_{12} and G_{21} are as given above [65].

Appendix C

Analytical Solution of Frozen Conical Boundary Layer

This appendix discusses the analytical solution for a frozen conical boundary layer. The compressible flat plate boundary layer equations are solved using the Dorodnitsyn-Howarth transformation [52], and this solution is transformed into a conical boundary layer profile.

C.1 Dorodnitsyn-Howarth Transformation

This transformation eliminates density from the boundary layer equations, reducing them to equations for two functions of a similarity variable, one being temperature and the other related to velocity. We start with the momentum equation,

$$\rho u \frac{\partial u}{\partial x} + \rho v \frac{\partial u}{\partial y} = \frac{\partial}{\partial y}(\mu \frac{\partial u}{\partial y}) \tag{C.1}$$

and the energy equation,

$$\rho u \frac{\partial h}{\partial x} + \rho v \frac{\partial h}{\partial y} = \frac{\partial}{\partial y}(k \frac{\partial T}{\partial y}) + \mu (\frac{\partial u}{\partial y})^2. \tag{C.2}$$

Defining a new distance variable $\overline{Y}$ by

$$\overline{Y} = \int_0^y \frac{\rho}{\rho_1} dy$$

where the subscript 1 refers to edge conditions. We define the similarity variable η as

$$\eta = \overline{Y} \left(\frac{\rho_1 U_1}{2 \mu_1 x} \right)^{\frac{1}{2}}.$$

Expressing the temperature and velocity in terms of η

$$T = T(\eta) \qquad\qquad \frac{u}{U_1} = f'(\eta)$$

the momentum equation becomes

$$ff'' + \left(\frac{\rho\mu}{\rho_1\mu_1} f''\right)' = 0 \tag{C.3}$$

and the energy equation becomes

$$fh' + \left(\frac{\rho\mu}{\rho_1\mu_1}\frac{k}{\mu} T'\right)' + \frac{\rho\mu}{\rho_1\mu_1} U_1^2 (f'')^2 = 0. \tag{C.4}$$

The boundary conditions for this system are

$$f(0) = f'(0) = 0 \qquad\qquad f'(\infty) = 1$$

$$T(\infty) = T_1 \qquad \text{and either} \begin{cases} T(0) = T_w & \text{isothermal wall} \\ T'(0) = 0 & \text{adiabatic wall} \end{cases}.$$

For the frozen case, the equation of state is simply $p = \rho RT$ and since the pressure is constant in the boundary layer, this reduces to $\rho T = \rho_1 T_1$. With this, (C.3) and (C.4) respectively become

$$ff'' + \left(\frac{\mu}{\mu_1}\frac{T_1}{T} f''\right)' = 0 \tag{C.5}$$

and

$$\left(\frac{1}{Pr}\frac{\mu}{\mu_1}\frac{T_1}{T} T'\right)' + fT' + \frac{U_1^2}{C_p}\frac{\mu}{\mu_1}\frac{T_1}{T} (f'')^2 = 0. \tag{C.6}$$

C.2 Mangler Transformation

Once the flat-plate boundary layer solution is obtained from the preceding system, it must be transformed to a conical boundary layer using the Mangler transformation [52]. For the flat plate, the distance from the leading edge will be denoted by x and the normal distance from the plate will be denoted by $\overline{y}$. For the cone, the distance from the tip will be denoted by ξ, and the normal distance from the cone surface by y (see Figure C.1). For

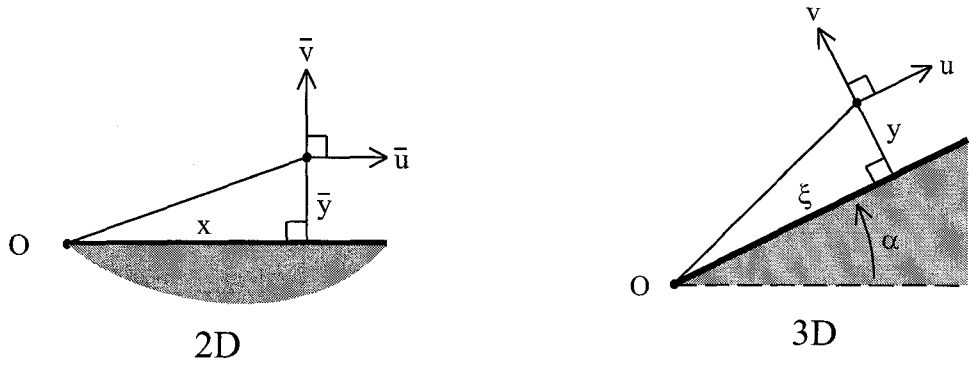

Figure C.1 Mangler transformation

a cone of half-angle α, the Mangler transformation reduces to

$$\xi = \left(\frac{3x}{sin^2\alpha}\right)^{\frac{1}{3}} \qquad\qquad y = \frac{\overline{y}}{(3\ x\ sin\alpha)^{\frac{1}{3}}}\ .$$

In summary, the flat plate boundary layer is solved in terms of the similarity variable of the Dorodnitsyn-Howarth transformation (η), which corresponds to coordinates (x,$\overline{Y}$). These are then transformed back to the normal distance variables (x, $\overline{y}$). Finally the Mangler transformation is used to convert these flat-plate variables to the conical distance coordinates (ξ, y), which may be compared to numerical simulations.

As always, the solution of the boundary layer requires known edge conditions that correspond to the inviscid surface conditions. These were determined by numerically simulating the inviscid frozen flow at the appropriate radius, which can be computed using the stepback method.

Appendix D

Problems with Parallel Implementation

When this work was started, the available sequential machines did not have enough memory to perform high-resolution simulations such as those shown above. The advantage of the Delta was that the memory could be spread over a large number of processors. Recall that these simulations were performed using the implicit version of PGP. The stability advantage of an implicit method is reached by using information from all the cells of the domain. But here the domain is decomposed onto multiple processors, so that each processor sees only its portion of the grid, with the values of the dummy cells provided by the appropriate local cells from other processors. It is counter-productive to decompose the grid onto as many processors as possible; each processor will only see a few cells. In order to retain the advantage of the implicit version, one wants to use as *few* processors as possible.

However, there is an additional problem. Application of the implicit algorithm results in slight discontinuities at the edge of each processor's grid. In regions of smooth flow, these discontinuities are negligible and, in fact, undetectable. However, in regions of large variation, this effect is significant. Basically, this means that one wants to select the domain decomposition so that regions of large shear do not cross processor boundaries. For example, one should choose a decomposition such that each processor grid at the surface contains the entire boundary layer.

Each of the Delta's processors has only 12 MB of memory, which severely limits the size of the local processor grids. Each processor can handle a grid of about 30 cells by 30 cells. For most of the flow field, this does not present any problems. However, the corner of the recirculation zone (i.e., the portion of the global grid adjacent to the leeward plane of symmetry and the cone surface) contains shear in two directions (see Figure D.1). A shear layer exists at the plane of symmetry, where the separated shear layer hits its counterpart from the opposite side of the cone. The shear layer is turned back toward the cone, and then feeds into the boundary layer at the cone surface. Figure D.1 shows temperature contours (with more contours than shown previously, to emphasize the problem), with the maximum

temperature occurring near the center of the recirculation zone. The edges of the local processor grids are evident in several places, most notably at the temperature maximum. With the processor memory limitations of the Delta, it is impossible to select a decomposition where the local grid there fully contains both the shear layer and the boundary layer. However, for the "best" decomposition (which is the one shown in the figure), the processor edge discontinuities were not evident in the computed surface quantities, so these errors did not affect the quality of the solution.

Of course, for a parallel machine with more memory per processor, this will not be an issue.

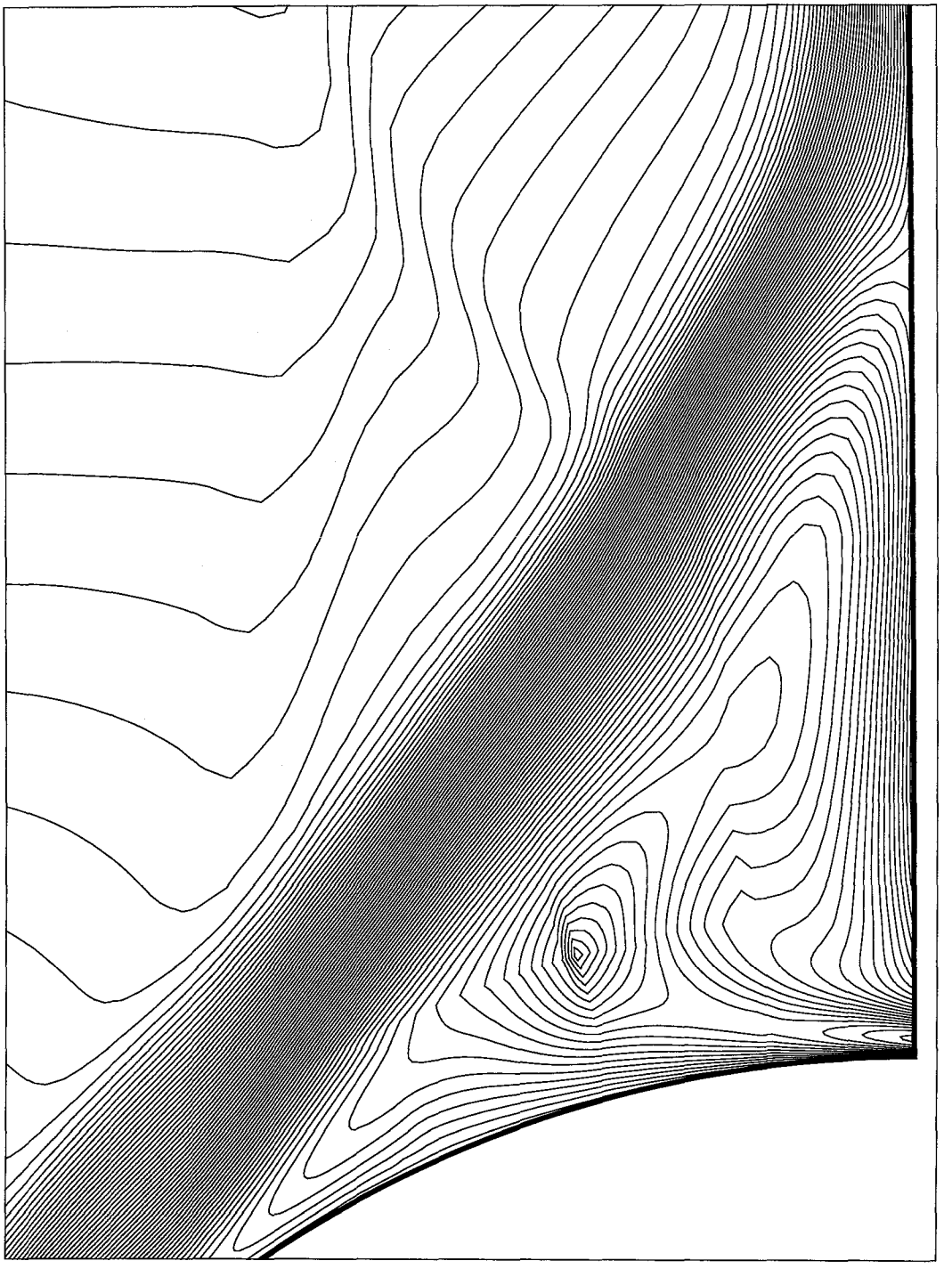

Figure D.1 Discontinuities from edges of locally implicit processor grids.

Appendix E

Grid Stretching Function

This appendix outlines the stretching function used to generate the grids in this work. The function is Roberts' first stretching function [58]. Consider a one-dimensional grid stretching function ψ. This function will map the index of a cell to the coordinate for the centroid of that cell. Let the grid contain n cells and extend from $x_0 \leq x \leq x_n$. The internal cell interfaces can be labelled i_1 to i_{n-1}, and the edges of the grid are given by $x(i_0) = x_0$ and $x(i_n) = x_n$. The stretching function may be specified by choosing the location of the centroid of the first interior cell, or equivalently by choosing the interior edge of the first cell. The position of cell interface i is conveniently specified by the ratio

$$\xi(i) = \frac{x(i) - x(i_0)}{x(i_n) - x(i_0)}. \tag{E.1}$$

Roberts' first stretching function uses a function $\psi(i;\, i_0, i_n, \beta)$, where i_0, i_n, and β are parameters for ψ, and i is the argument of the function. β is a stretching parameter which is determined by finding the value of β which satisfies the previous selection of $\psi(1; i_0, i_n, \beta) = \xi(i_1)$. Define

$$\eta = (i - i_0)/(i_n - i_0) \tag{E.2}$$

and

$$b = \left(\frac{\beta + 1}{\beta - 1}\right)^{1-\eta}. \tag{E.3}$$

The stretching function ψ can finally be defined by

$$\psi = \frac{\beta + 1 - b(\beta - 1)}{1 + b}. \tag{E.4}$$